

University of Alberta

Geomechanical Modeling of Rock Deformation and Associated
Microseismicity

by

Drew Chorney

A thesis submitted to the Faculty of Graduate Studies and Research
in partial fulfillment of the requirements for the degree of

Master of Science

in

Geophysics

Department of Physics

©Drew Chorney

Spring 2014

Edmonton, Alberta

Permission is hereby granted to the University of Alberta Libraries to reproduce single copies of this thesis and to lend or sell such copies for private, scholarly or scientific research purposes only. Where the thesis is converted to, or otherwise made available in digital form, the University of Alberta will advise potential users of the thesis of these terms.

The author reserves all other publication and other rights in association with the copyright in the thesis and, except as herein before provided, neither the thesis nor any substantial portion thereof may be printed or otherwise reproduced in any material form whatsoever without the author's prior written permission.

To my Parents

Abstract

Microseismicity monitoring is increasingly being used to assess in real time the effectiveness of hydraulic fracture treatments. As this tool continues to become more prevalent, questions regarding the observed microseismicity and the geomechanics are being asked. In particular, why is failure occurring in specific locations and not others? What are the failure mechanisms? Where is all the input energy going? What does the energy budget look like? Often substantial differences are estimated between the total input energy inferred from fluid injection rates and the radiated energy observed from recorded seismicity. The injected energy is 10^4 - 10^7 times larger than the estimated radiated seismic energy, and the fracture energy is inferred to equal 15 - 40 % of the input energy (Maxwell et al., 2008; Boroumand and Eaton, 2012). These questions are difficult to answer from the recorded seismicity alone but geomechanical modeling may be able to provide some insight. Using the Bonded Particle Model (BPM) logic sandstone core samples are modeled as the aggregation of thousands of bonded spherical particles. Uniaxial and tri-axial tests on these cylindrical sleeves reproduce the macroscopic properties of rock. A number of features of the models are analyzed with a strong emphasis on investigating the deformation of the samples and their associated energy budget.

Acknowledgements

I wish to thank my supervisors Mirko van der Baan and Claire Currie. Their guidance was vital for moving from a strictly formal mathematics background into the study of geophysics and geomechanics. In particular, Mirko for introducing me to microseismics and transforming me from an undergraduate student into a young academic. Additionally, I'd like to thank Mirko for his patience as I took on additional course work and internships. I'd like to thank my friends and colleagues, especially Melanie Grob and Piyush Jain for their patience and help as we worked together to publish some of this work. Also my two office mates Colin More and Daniel Laycock. I very much enjoyed our conversations, arguments and musings. Thanks Colin for the help with the last minute panic of closing out this thesis. Special thanks to Clinton Loo; your advice and help played a big role in starting and completing this M.Sc.

Thanks to my old supervisors Kristine Bauer and Matthew Greenberg. Thank you Kristine for all your advice and support throughout the years. Special thanks to Eric Mcfee for supporting me as I left the military.

This work was supported by the Microseismic Industry Consortium. I would like to thank the Microseismic Industry Consortium and Itasca for providing licenses for the PFC software.

Finally, to my parents, Marion and Michael, and my brother and sister, Lance and Lauren. Without the support of my family, none of this would have been possible. I dedicate this thesis to my parents. Thank you Mom and Dad.

Contents

1	Introduction	1
1.1	Introduction	1
1.2	Microseismicity vs. Expected Energy Release	3
1.3	Slow Slip Events	4
1.4	A Powerful Geomechanical Model	5
1.5	Thesis Outline	6
2	Geomechanics Review	8
2.1	Continuum Mechanics	8
2.1.1	Stress	8
2.1.2	Strain	11
2.1.3	Isotropic Elasticity	13
2.2	Laboratory Testing of Rocks	14
2.2.1	The Elastic, Ductile, Brittle and Plastic Regimes	15

2.2.2	Uniaxial and Triaxial Tests	15
2.2.3	Brazilian Tensile Test	17
2.3	Friction	19
2.3.1	A Micromechanical Model	20
2.4	Rock Failure	21
2.4.1	Failure Criterion	22
2.5	Wave Propagation, Moment Tensor and Source Mechanisms	24
2.5.1	The Quality Factor	26
2.5.2	The Moment Tensor and Source Mechanisms	27
2.5.3	The Hudson Plot	28
2.5.4	The Gutenberg-Richter Power Law and the Fractal Dimension	29
3	Numerical Modeling and the Bonded Particle Model	32
3.1	Numerical Modeling	32
3.2	The Theory of Bonded Particle Modeling	35
3.2.1	Model Formulation and the Law of Motion	36
3.2.2	Contact Models	39
3.2.3	Damping of the System and the Quality Factor	42
3.2.4	The Moment Tensor	43
3.2.5	Energy	45

4	Assembly and Calibration of the Bonded Particle Models	47
4.1	Spherical Packings	47
4.2	Material Genesis	48
4.3	Compression and Tensile Tests	51
4.4	Porosity	52
4.5	Sample Calibration	55
4.6	Triaxial Tests	58
5	Brittle Deformation and its Associated Microseismicity	61
5.1	Geomechanical Modeling of Rock Fracturing and Associated Microseismicity	62
5.1.1	Introduction	62
5.1.2	Bonded Particle Model	63
5.1.3	Microseismicity	67
5.1.4	Mechanical Observations	67
5.1.5	Microseismicity Analysis	71
5.1.6	Discussion	75
5.1.7	Conclusion	76
5.2	Energy Budget Discrepancy between Rock Fracturing and As- sociated Microseismicity	77

5.2.1	Introduction	78
5.2.2	Modeling	80
5.2.3	Simulations	87
5.2.4	Results	94
5.2.5	Discussion	102
5.2.6	Conclusion	105
5.3	Discussion and Conclusions	106
6	Aseismic Stress Release and Stable Sliding	109
6.1	Joint Calibration	110
6.2	Internal Shearing on a Fracture	117
6.3	Energy Budget for Stable Sliding on a Joint	120
6.4	Discussion and Conclusions	125
7	Seismicity and Radiation Patterns	127
7.1	Wave Propagation	127
7.2	Seismograms of a Large Triaxial Simulaion	138
7.3	Future Work	139
8	Conclusions and Future Work	142

List of Tables

4.1	Porosities given distributions of particle sizes	53
4.2	Triaxial experiment results	55
4.3	Microproperties for a sandstone	58
4.4	Laboratory elasticity results	60
4.5	Numerical elasticity results	60
5.1	Microproperties for sandstone from The Leading Edge article .	66
5.2	The Leading Edge sandstone macroproperties	66
5.3	Peak stresses vs. joint size	70
5.4	Energy content for The Leading Edge simulations	71
5.5	The Leading Edge, microseismicity analysis	72
5.6	Tectonophysics mechanical properties of sandstone	88
5.7	Tectonophysics energy budget	91
5.8	Tectonophysics b-values	99
6.1	Young's moduli as a function of joint angle	120

List of Figures

2.1	Stress vs. strain curves	16
2.2	Brazilian test	18
2.3	Failure envelope	22
2.4	Moment tensor	27
2.5	Hudson plot	29
3.1	Bonded particle model geometry	35
4.1	Cylindrical sample	49
4.2	Low porosity stress vs. strain curves	56
4.3	Uniaxial stress vs. strain curve	59
4.4	Stress envelope	59
5.1	Sandstone samples	64
5.2	The Leading Edge stress vs. strain curves	68
5.3	Jointed sample	69

5.4	The Leading Edge event locations	74
5.5	The Leading Edge Hudson plots	75
5.6	Tectonophysics jointed sample	88
5.7	Tectonophysics stress vs. strain curves	90
5.8	Tectonophysics bond breakages	96
5.9	Tectonophysics event locations	97
5.10	Tectonophysics frequency-magnitude distribution	98
5.11	Tectonophysics temporal variations of the b-values	99
5.12	Tectonophysics Hudson plots	100
5.13	Tectonophysics radiated energy vs. magnitude	101
6.1	Shear test environment	111
6.2	Idealized frictional behavior	112
6.3	Direct shear test results - high friction	115
6.4	Updated shear test environments	116
6.5	Shear test results - low friction	118
6.6	Coulomb friction curves	119
6.7	Effective Young's modulus curve	120
6.8	Frictional work as a function of bond breakages	121

6.9	Stress vs. strain curves for jointed sample	124
7.1	Three component seismogram	130
7.2	Seismogram and the bond breakages	131
7.3	A seismogram zoomed in	132
7.4	An array of receivers	133
7.5	Particle motions at the source and a receiver	134
7.6	Theoretical radiation pattern for a single particle dislocation	137
7.7	Radiation pattern from the bonded particle model	137
7.8	A three dimensional seismic array	138

Chapter 1

Introduction

1.1 Introduction

When there is a failure or break in a medium of rock, elastic waves are generated and propagate with an amplitude directly related to the magnitude of the source of the disturbance. When amplitudes are relatively small, seismologists call them microseismic events. Such events are generally faint relative to the amplitude of elastic waves generated by earthquakes or those of exploded ordinance in traditional reflection seismology. Over the past few years, interpretation of the microseismicity originating from hydraulic fracturing into unconventional hydrocarbon reservoirs by fluid injection has enabled seismologists to create updated real-time images of complex fracture geometries of the target rock (Maxwell and Urbancic, 2001). Monitoring the microseisms originating from hydraulic fracturing has become a prevalent diagnostic tool. Locations of microseisms in the subsurface are used to monitor the growth of the fracture network.

As interpretation of microseisms has become more prevalent in recent years, there is now a desire to understand both the static and dynamic geomechanical processes occurring during the hydraulic fracturing of rock. Complex mechanisms in the subsurface are taking place at all stages during hydraulic fracturing. Unfortunately, the subsurface rock is not directly observable so that inferring geomechanical processes is difficult. Monitoring fluid pressure during the fracture treatment and having a reliable estimate of the local tectonic stress provides a means for estimating fracture propagation but the behavior becomes more difficult to predict within complicated lithologies (for example highly faulted formations). Geomechanical modeling becomes a useful tool for providing a means of insight into the behavior of the mechanical processes occurring within the reservoir during hydraulic fracturing. If a geomechanical model is calibrated to the known properties of rock that are observed during laboratory experiments, the models can then be expanded and implemented into more complicated scenarios. In the more complicated simulations the geomechanical processes can then be directly monitored (which is of course not possible in practice). The objective of this thesis is to use 3D particle flow codes or the bonded particle model (BPM) to simulate the geomechanical behavior of rock deformation along with its associated microseismicity. The models will be used to discuss and analyze some otherwise complicated topics; some motivation follows now.

1.2 Microseismicity vs. Expected Energy Release

There are several primary factors that influence the seismic deformation during hydraulic fracturing. Pressure, injection rates and fluid dynamics are all correlated to the microseismicity observed in the hydraulic fracturing ("fracking") of rock. If pressure and injection rates for a particular fracking operation are known, it is possible to deduce the energy being applied to the target rock. This injection energy is computed as the product of the volume of fluid pumped and the injection pressure. On the other hand, the seismic moment of a microseism can be calculated and used to obtain an estimate of the total energy released via brittle failure (Warpinski et al., 2001).

It is observed that the measured energy input of the system vs. the energy output observed from the microseismicity is millions of orders smaller (Maxwell et al., 2008). Possible explanations for the low output energy percentages could be the result of the attenuation of high frequencies and energy losses due to friction and fluid leak-off. This will explain some of the energy loss but it is likely that orders of magnitude of energy are not accounted for by measured brittle failure. A complete analysis of the energy budget during hydraulic fracturing is difficult and provides an interesting topic for geomechanical modeling. It is likely that semi-brittle/ductile deformation, without release of seismic signal (i.e., aseismic), plays a significant role. The culprits for this ductile deformation may be stored strain energy in the rock and possibly aseismic stress release along faults and joints (Zoback et al., 2012).

1.3 Slow Slip Events

For many years, strange phenomena have been observed at subduction interfaces all around the world. Seismologists observe changes in position of the earth's crust where no seismicity is detected. These events, often called slow slip events, are complex geomechanical mechanisms that release energy by other means than traditional elastic wave propagation. It is possible that analogous deformation may occur during hydraulic fracturing (Zoback et al., 2012).

In modern plate tectonic theory, earthquakes are the result of large plates of oceanic or continental crust shifting and moving with respect to one another. Friction along faults causes the plates to become locked, producing a buildup of strain. As stress increases, the strain of the rock reaches failure and a rapid slip occurs resulting in an earthquake. Traditionally, movements along faults were thought to be discontinuous; that annual averages of plate movement per year were strictly the consequence of these brittle spasmodic slips and ruptures along the fault plane; also known as stick-slip sliding (Stein and Wysession, 2003). With technological advances throughout the past decade, using GPS, seismologists are now able to accurately monitor displacements of relative crustal positions to within millimeters. Consequently, shifting of plates at subduction zones have been observed over large intervals of time where no seismic activity is detected. Seismologists propose that plates are in constant motion and there are in fact "silent earthquakes" that act as a mode of stress release that produce no seismic waves or noise in the surrounding rock (Schwartz et al., 2007). There are a number of such studies at subduction interfaces around the world, for example, the Bungo Channel in Japan (Hirose et al., 1999), the Guerrero gap in Mexico (Yoshioka et al., 2004), and the

Cascadia in western Canada (Dragert et al., 2001).

These slow slip events, also called aseismic events or creep events, have been observed to last anywhere from between a few days to as long as years. It is speculated that a slow slip event is the result of stable sliding of the overriding plate over the subducting plate. Pressure and thermal properties most likely play a significant role in the change of frictional properties.

Hydraulic fracturing of subsurface reservoirs subject the rock to intense pressure and it seems reasonable to suggest that similar aseismic processes may occur. Finally, at many of these subduction zones non volcanic seismic tremor complements the slow slip events (Beroza and Ide, 2011). The correlation between the two phenomena is yet to be understood but the tremor is thought to be the result of varying fluid dynamics occurring deep within the subduction interface. Non-volcanic tremor is also observed during hydraulic fracture treatments.

Although this deformation is likely the complicated superposition of both rock mechanics and fluid dynamics it is nevertheless another interesting topic for geomechanical modeling. Unfortunately in this thesis there will be no hydromechanical models, but if a stable slide could be successfully modeled under more simplistic conditions it's possible it may provide some insight into the energy budget and the deformation of a slow slip event and perhaps an explanation for the mysterious non-volcanic tremor.

1.4 A Powerful Geomechanical Model

It is of general interest to understand the behavior of reservoir deformation when subject to certain boundary conditions. In a traditional continuum me-

chanics approach, the stress field of a continuum, subject to boundary conditions, can be calculated by solving the Navier equations using a finite difference or distinct element method. In order to investigate a dynamical system the equations of motion with the inertial and body force terms must be solved. Ideally, a perfect numerical model should include criterion for failure of the medium while simultaneously modeling quasistatic stress/strain and wave propagation; thus of course making the implementation of continuum models increasingly more difficult. In a continuum based code it is difficult to create models in which fractures propagate naturally. Complex constitutive failure relations are required to establish the link between stress/strain, failure, and the dynamics of the system. In particular, an ideal geomechanical model will be able to handle source mechanisms with moment tensors agreeing with elastodynamics of the models. The moment tensors provide the link between the rock mechanics to the dynamics of the reservoir and the ideal model should handle this as naturally as possible.

1.5 Thesis Outline

The main objectives of this thesis here is to:

1. Explore the energy budget of triaxial simulations conducted on bonded particle models in the hopes of providing insight into the discrepancy observed between the input energy and brittle failure energy during hydraulic fracture treatments.
2. Model a stable slide to provide a possible candidate for ductile deformation while simultaneously monitoring the energy budget (specifically energy losses to friction).

3. Although not the primary objective, the flavor throughout the thesis should constantly act to reinforce the power of the BPM. An ideal model should handle quasistatic stress/strain, various deformation (including rock failure), and elastodynamics.

In Chapter 2 elementary geomechanics is reviewed to provide the reader with the appropriate background. Chapter 3 introduces the BPM providing the detailed logic and explanation for the construction of these models. In Chapter 4 the calibration of the models to the macroscopic properties of a sandstone is discussed. Chapter 5 jumps into two papers (one published the other in the process of being submitted) that carefully examine objective (1). In Chapter 6 frictional sliding is modeled to achieve objective (2). Chapter 7 introduces the elastodynamics of the models. A large simulation is run encapsulating all of the proceeding work with the addition of an array of seismograms in the hopes of establishing a link between the geomechanics and the microseismicity. Although, with no dedicated chapter in particular, throughout the thesis objective (3) will be reinforced. Results are summarized and future work is discussed in Chapter 8.

Chapter 2

Geomechanics Review

Rock mechanics or geomechanics is primarily the study of rock masses subject to stresses and strains. For the bonded particle modeling that will follow shortly, it is necessary to introduce some of the necessary mechanisms for a good quantitative analysis of the geomechanics of the models. The following mathematical formulation is introduced in detail in Jaeger et al. (2007) and Fjaer et al. (2008).

2.1 Continuum Mechanics

2.1.1 Stress

At any point in a continuum both shear and normal force per unit area can be calculated for each of the three Cartesian coordinate axes x , y , and z . These

nine stress components are the entries of the stress tensor $\boldsymbol{\tau}$,

$$\boldsymbol{\tau} = \begin{pmatrix} \tau_{xx} & \tau_{xy} & \tau_{xz} \\ \tau_{yx} & \tau_{yy} & \tau_{yz} \\ \tau_{zx} & \tau_{zy} & \tau_{zz} \end{pmatrix}. \quad (2.1)$$

If n is a vector in Euclidean space, then $T = \boldsymbol{\tau}n$ is the traction vector on a plane with unit normal n . Solving the eigenvalue problem $\boldsymbol{\tau}n = \lambda n$ gives 3 eigenvalues and corresponding eigenvectors. With coordinates in the direction of the eigenvectors, the principal or rotated tensor, $\boldsymbol{\sigma}$, becomes,

$$\boldsymbol{\sigma} = \begin{pmatrix} \sigma_1 & 0 & 0 \\ 0 & \sigma_2 & 0 \\ 0 & 0 & \sigma_3 \end{pmatrix}. \quad (2.2)$$

In short, the stress tensor is now orientated so that shear stress is zero on planes with normals corresponding to the three eigenvectors. These are the principal stress directions with magnitude σ_1 , σ_2 and σ_3 . The mean stress at a point in the continuum is

$$\sigma_m = \frac{\sigma_1 + \sigma_2 + \sigma_3}{3}. \quad (2.3)$$

This is also known as hydrostatic or isotropic stress.

To obtain the magnitude of the normal stress σ and shear stress τ on a plane with unit normal n , the traction vector, T , is projected onto the unit normal $n = (n_1, n_2, n_3)$. Then

$$\sigma = \sigma_1 n_1^2 + \sigma_2 n_2^2 + \sigma_3 n_3^2, \quad (2.4)$$

$$\begin{aligned}\tau &= \pm\sqrt{|T|^2 - \sigma^2} \\ &= \pm\sqrt{(\sigma_1 - \sigma_2)^2 n_1^2 n_2^2 + (\sigma_2 - \sigma_3)^2 n_2^2 n_3^2 + (\sigma_3 - \sigma_1)^2 n_3^2 n_1^2}.\end{aligned}\quad (2.5)$$

In two dimensions, setting $n_1 = \cos\theta$, $n_2 = \sin\theta$ and $n_3 = 0$, (2.4) and (2.5) reduce to the Mohr circle equations,

$$\sigma = \frac{(\sigma_1 + \sigma_2)}{2} + \frac{(\sigma_1 - \sigma_2)}{2}\cos 2\theta, \quad (2.6)$$

$$\tau = -\frac{(\sigma_1 - \sigma_2)}{2}\sin 2\theta. \quad (2.7)$$

An invariant of a tensor is a value that is the same regardless of the choice of coordinate system. There are a number of invariants of the stress tensor which are of interest in rock mechanics. The trace of a second order tensor is the same in any coordinate system; so the mean stress from equation (2.3) is invariant. Another invariant of interest is

$$q = \sqrt{\frac{1}{2} [(\sigma_1 - \sigma_2)^2 + (\sigma_2 - \sigma_3)^2 + (\sigma_1 - \sigma_3)^2]}. \quad (2.8)$$

q is often called the generalized shear stress. It is a measure of how far the stress tensor deviates from purely hydrostatic.

The stress tensor, $\boldsymbol{\tau}$, can be decomposed into an isotropic part, $\boldsymbol{\tau}^{iso}$, and deviatoric part, $\boldsymbol{\tau}^{dev}$, where

$$\boldsymbol{\tau}^{iso} = \begin{pmatrix} \sigma_m & 0 & 0 \\ 0 & \sigma_m & 0 \\ 0 & 0 & \sigma_m \end{pmatrix}, \text{ and} \quad (2.9)$$

$$\boldsymbol{\tau}^{dev} = \boldsymbol{\tau} - \boldsymbol{\tau}^{iso}. \quad (2.10)$$

$\boldsymbol{\tau}^{iso}$ controls the volumetric change of a rock, whereas $\boldsymbol{\tau}^{dev}$ is a measure of the distortion of the rock.

2.1.2 Strain

In the one-dimensional context, when a continuum is subject to stress there is a fractional decrease or increase in the length of a fictional bar within the continuum. Completely analogous to the stress tensor, there are nine strain components that form the strain tensor in Cartesian coordinates,

$$\boldsymbol{\varepsilon} = \begin{pmatrix} \varepsilon_{xx} & \varepsilon_{xy} & \varepsilon_{xz} \\ \varepsilon_{yx} & \varepsilon_{yy} & \varepsilon_{yz} \\ \varepsilon_{zx} & \varepsilon_{zy} & \varepsilon_{zz} \end{pmatrix}. \quad (2.11)$$

For an arbitrary particle in the continuum at position (x, y, z) , with an applied stress that causes particle displacement (u, v, w) , the normal strains are,

$$\varepsilon_{xx} = \frac{\partial u}{\partial x}; \quad \varepsilon_{yy} = \frac{\partial v}{\partial y}; \quad \varepsilon_{zz} = \frac{\partial w}{\partial z}. \quad (2.12)$$

The shear strains are,

$$\begin{aligned}\varepsilon_{xy} = \varepsilon_{yx} &= \frac{1}{2} \left(\frac{\partial u}{\partial y} + \frac{\partial v}{\partial x} \right), & \varepsilon_{xz} = \varepsilon_{zx} &= \frac{1}{2} \left(\frac{\partial u}{\partial z} + \frac{\partial w}{\partial x} \right), \\ \varepsilon_{yz} = \varepsilon_{zy} &= \frac{1}{2} \left(\frac{\partial v}{\partial z} + \frac{\partial w}{\partial y} \right).\end{aligned}\tag{2.13}$$

The normal strains are a measure of the volumetric change of the rock, and the shear strains are a measure of the angular distortion of the rock. Completely analogous to the stress tensor, the strain tensor can be rotated into a unique orthogonal principal coordinate system, so that $\boldsymbol{\varepsilon}$ takes on the form,

$$\boldsymbol{e} = \begin{pmatrix} \varepsilon_1 & 0 & 0 \\ 0 & \varepsilon_2 & 0 \\ 0 & 0 & \varepsilon_3 \end{pmatrix}.\tag{2.14}$$

At every point in the continuum, when in the principal strain coordinate system, the deformation is strictly stretching and/or compression along three mutually perpendicular directions. Analogous to the stress tensor $\boldsymbol{\varepsilon}$ can be decomposed into an isotropic part, $\boldsymbol{\varepsilon}^{iso}$, and a deviatoric part, $\boldsymbol{\varepsilon}^{dev}$, such that

$$\boldsymbol{\varepsilon} = \boldsymbol{\varepsilon}^{iso} + \boldsymbol{\varepsilon}^{dev}.\tag{2.15}$$

The volumetric strain is,

$$\varepsilon_v = \text{trace}(\boldsymbol{\varepsilon}^{iso}) = \varepsilon_1 + \varepsilon_2 + \varepsilon_3.\tag{2.16}$$

2.1.3 Isotropic Elasticity

For an isotropic medium, the linear relationship between stress and strain takes the form

$$\sigma_1 = (\lambda + 2G)\varepsilon_1 + \lambda\varepsilon_2 + \lambda\varepsilon_3, \quad (2.17)$$

$$\sigma_2 = \lambda\varepsilon_1 + (\lambda + 2G)\varepsilon_2 + \lambda\varepsilon_3, \quad (2.18)$$

$$\sigma_3 = \lambda\varepsilon_1 + \lambda\varepsilon_2 + (\lambda + 2G)\varepsilon_3, \quad (2.19)$$

where λ and G are the Lamé parameters. G is also known as the shear modulus that relates stresses to strains in pure shear. When the medium is isotropic, the behavior is described solely by these two parameters. There are three other elasticity parameters, the Young's modulus, E , the Poisson's ratio, ν , and the Bulk modulus, K . The dimension of the parameter space $\{\lambda, G, E, \nu, K\}$ is two, so that only two of the five parameters are needed to fully describe an isotropic elastic medium.

The relationship between the mean stress and the volumetric strain is,

$$\tau_m = \left(\lambda + \frac{2}{3}G \right) \varepsilon_v = K\varepsilon_v. \quad (2.20)$$

The Young's modulus is found by measuring the ratio of the stress to strain along one direction, that is,

$$E = \frac{\sigma_1}{\varepsilon_1}. \quad (2.21)$$

Poisson's ratio is defined as the negative of the ratio of the strain in perpendicular directions, that is,

$$v = -\frac{\varepsilon_2}{\varepsilon_1} = -\frac{\varepsilon_3}{\varepsilon_1}. \quad (2.22)$$

For the geomechanical modeling that is to follow, the elasticity parameters that are used to describe the models will be the Young's modulus and Poisson's ratio. These elasticity parameters are advantageous in that they are the easiest to measure in the laboratory (and in the numerical models as well).

2.2 Laboratory Testing of Rocks

When a rock is extracted from the subsurface there are several macroscopic properties of the sample that are of interest. Macroscopic properties of rock are heavily influenced by both the environment and its micromechanical attributes. Some examples could be, the porosity, length of diagenesis, compaction pressure, mineral composition, etc. Assuming isotropy, Young's modulus and Poisson's ratio fully describe the elasticity of the rock. From (2.21) the Young's modulus is a measure of the stiffness of the sample. The stiffer the sample, the greater the stress needed to cause unit strain. Poisson's ratio is a measure of how much the rock expands in directions perpendicular to an applied strain. The uniaxial compressive strength (UCS), C_o , of the sample is a measure of the maximum compressive stress that occurs just before the sample fails. The tensile strength, T_o , is a measure of the stress needed to cause failure of the sample in tension. Laboratory tests are conducted on core samples of the rock to determine these four parameters. Before discussing the method for determining these parameters it is useful to discuss several states that the rock may be in depending on the magnitude of the applied stress.

2.2.1 The Elastic, Ductile, Brittle and Plastic Regimes

There are several regimes in which a continuum may behave depending on the magnitude of confinement on the sample. If the deformation on a rock is small, the original position of the particles in the rock will return to their initial positions after an applied stress is removed. This deformation is in the elastic regime. If further stress is applied to a sample, eventually the stress will reach the yield stress. After the yield stress has been exceeded the original positions of the particles will not be recovered with the applied stress being removed. In this regime, irreversible damage has taken place but the sample still supports the load. The rock is said to be ductile. If the stress is increased further, the sample will eventually be unable to sustain the axial load and in which case the sample fails completely. The regime where the stress strain curve drops off abruptly is called the brittle regime. The elastic, ductile, and brittle regimes are shown in Figure 2.1a. A rock behaves in an ideally plastic fashion when subjected to an infinite amount of strain, there is no resulting change in the stress on the sample. This behavior is idealized in Figure 2.1b.

2.2.2 Uniaxial and Triaxial Tests

In practice, rock samples are removed from the surface as cylindrical cores on which stresses and strains are applied to measure the macroscopic behavior. An idealized core sample is shown in Figure 2.1c. The two large arrows show the direction of the axial load, whereas the smaller radial arrows show the confinement pressure.

The first test to apply on a core sample is the uniaxial compression test. This single test determines the Young's modulus, Poisson's ratio, and the UCS.

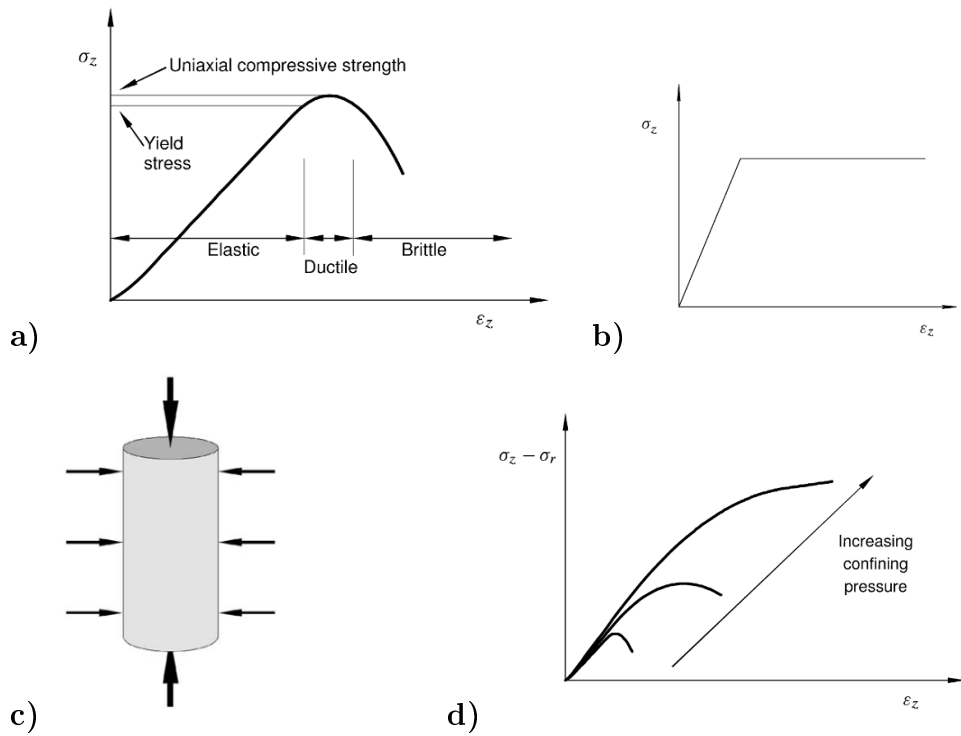


Figure 2.1: The elasticity regimes. a) Stress strain curve showing the elastic, ductile and brittle regimes. b) An image showing ideal plastic behavior. c) Cartoon displaying the triaxial setup. d) Stress strain curves are increasing confinement pressures. For images a) and b) strain on the horizontal axis and stress on the vertical axis. In d) differential stress on the vertical axis. After Fjaer et al. (2008).

The axial length of the core is held in position by platens, while the stress of these two platens on the sample is increased. The radial stress of the sample is zero. The scenario is such that $\sigma_1 \neq 0$, $\sigma_2 = 0$, and $\sigma_3 = 0$. The maximum stress that the platens achieve before the sample fails is the unconfined (or uniaxial) compressive strength. This is depicted in an axial stress vs. axial strain curve, see Figure 2.1a. Young's modulus from (2.21) is then the slope of the stress strain curve in the elastic regime. Poisson's ratio from (2.22) is then obtained from the slope of the elastic axial strain vs. radial strain curve of the core sample. In the laboratory these measurements are achieved with sensitive stress/strain gauges.

Triaxial tests are similarly conducted on a cylindrical core sample. The triaxial test is completely analogous to the uniaxial test except now $\sigma_2 = \sigma_3 \neq 0$. A servo maintains a constant confinement on the sample while the axial load is applied. In the same fashion, stresses and strains of the sample are monitored to provide the overall macroscopic behavior of the confined sample. Just as with the uniaxial tests, the compressive strength of the sample is measured. In general, as confinement pressure increases the compressive strength of the sample increases. Eventually, if the confinement pressure is high enough the failure becomes more ductile and the rock will no longer exhibit brittle failure. This behavior is shown in Figure 2.1d. Young's moduli and Poisson's ratios are often obtained for the cores samples under confinement as well.

2.2.3 Brazilian Tensile Test

The most popular test for finding the tensile strength of a core sample is to subject the sample to the Brazilian tensile test. The main axis of a core sample

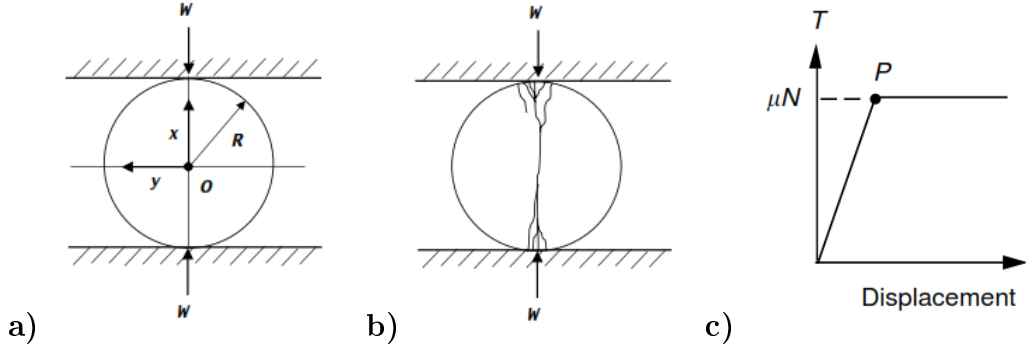


Figure 2.2: a) Shows the setup for Brazilian tensile tests; W is the point force, x and y the coordinate system, and R the radius of the cylinder. b) An image indicating the tensile failure of a core sample during a Brazilian test. c) An ideal stable slide. After Jaeger et al. (2007).

is placed perpendicular to an applied load; see Figure 2.2a. At the center of the disk the normal stresses along the x and y axes are,

$$\tau_{xx} = \frac{-W}{\pi R}, \quad \tau_{yy} = \frac{3W}{\pi R}, \quad (2.23)$$

where W is the point load (per axial length of the cylinder) and R is the radius of the cylinder (Jaeger et al., 2007). At the center of the cylinder, the compressional stress is exactly three times larger than the magnitude of tensile stress. However, the compressive strength of a rock is usually many times larger than that of the tensile strength. The sample will fail in tension first and the tensile strength of the sample by Eq. (2.23) is then

$$T_0 = \frac{3W_c}{\pi R}, \quad (2.24)$$

where W_c is the point load upon failure of the sample. Figure 2.2b illustrates the tensile fracture that forms when conducting a Brazilian tensile test.

2.3 Friction

Friction in rock mechanics can be described as the tendency for two contacting rock surfaces to resist displacement when a shear force is applied. Friction is of great importance in geomechanics at both the micromechanical level and macromechanical level. On the small scale, friction provides a resistance for mineral grains to slide. On the large scale it provides a resistance for sliding along faults and joints.

The shear friction of a rock surface is best described by the linear relationship,

$$\tau_f = S_0 + \mu\sigma, \quad (2.25)$$

where μ is the coefficient of friction of the rock, S_0 is the cohesion of the surface, and τ_f is the shear stress needed to cause sliding for a given normal stress, σ , on the plane in question. If $|\tau|$ on the plane is greater than $|\tau_f|$, the system will start to slide. In reality there are two frictional values; the coefficient of static friction, μ_s , and the coefficient of dynamic friction, μ_d . The friction coefficient in (2.25) is the coefficient of static friction. As the shear stress on the plane exceeds that of τ_f , sliding occurs and the coefficient of friction then drops off to the dynamic coefficient of friction (Dieteriech, 1979). In general there is a critical distance that must to be overcome before the dynamic friction stabilizes.

For a stable slide, on a surface with cohesion, S_0 , and coefficient of friction, μ , both the dynamic and static coefficients will be near equal with the shear stress leveling off onto τ_f . This ideal behavior is characterized in Figure 2.2c.

Stick slip sliding is the behavior for two elastic surfaces to spasmodically lock

and slide relative to each other. It has been found that with an increase in normal stress there is a transition from stable sliding to stick-slip sliding (Dieteriech, 1978). Experiments have found that a stiff rough surface tends to reduce the propensity for stick-slip sliding. There are other factors that may promote stable sliding over stick-slip oscillation. Stesky (1974) investigated the relationship between temperature and stick-slip sliding for a number of rocks samples. Higher temperatures increase the tendency for a stable slide. Finally pore pressure will play a role. With an increase in hydrostatic pressure, (2.25) becomes,

$$\tau_f = S_0 + \mu(\sigma - P_f), \quad (2.26)$$

where P_f is the pore pressure. If μ and S_0 remain unchanged the failure shear stress is much lower and the criterion for slippage is reduced. It is likely both temperature and pore pressure play a significant role in stable sliding vs. stick slip sliding.

2.3.1 A Micromechanical Model

With the coefficient of friction established, it is of interest to study the behavior of rocks with fractures and joints. Depending on the coefficient of friction and the stress field, rock may slide along preexisting faults and fractures. Ultimately this will have an effect on both the UCS of the sample along with its macroscopic elasticity parameters. Jaeger et al. (2007) discusses the effect of sliding crack friction on the Young's modulus of a rock sample under uniaxial compression. The computation assumes a thin plate of length L , width b , and thickness t , for which the thickness is negligibly small. For a crack of half

length c , with unit normal at an angle θ from the compression axis, by energy considerations, it can be shown that for a thin closed crack with joint friction μ ,

$$\frac{1}{E} = \frac{1}{E_m} \left(1 + \frac{(\sin^2 2\theta - 2\mu \cos^2 \theta |\sin 2\theta|) \pi c^2}{2bL} \right), \quad (2.27)$$

where E_m is the Young's modulus of the sample without a joint. The formula assumes the cohesion $S_0 = 0$, and again, the crack is thin and closed.

2.4 Rock Failure

When a rock is subject to large amounts of stress, failure eventually occurs. In the laboratory, while conducting triaxial tests on cylindrical core samples, the axial stress is increased until the sample is unable to withstand the load. If the confinement pressure is not too high, the sample responds to the excessive axial stress by failing in a brittle fashion.

From laboratory experiments, the failure of an unconfined core sample subject to an increasing axial load is often accompanied by irregular longitudinal splitting as the sample fails in tension. For triaxial tests, the sample fails as shear fractures develop at angles close to 45 degrees from the axial direction. At very high levels of hydrostatic pressure pore collapse occurs as the sample fails from excessive compaction. The grains of the rock are crushed causing permanent damage to the framework of the rock.

A sample subject to boundary conditions may eventually fail, and so it is natural to establish a criterion for these different types of failure. There are a number of such criteria that can be applied depending on the behavior of the

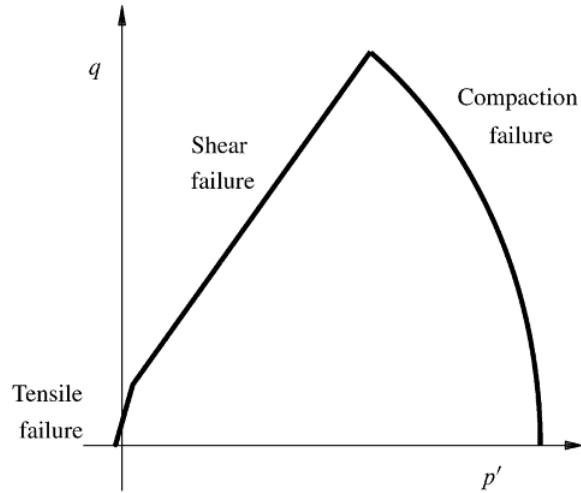


Figure 2.3: An example of a failure envelope. If the stress field intersects the envelope, failure occurs. Generalized shear stress on the vertical axis and effective normal stress on the horizontal axis. After Fjaer et al. (2007).

rock in question. Only a very small subset of the many criteria are discussed here.

2.4.1 Failure Criterion

If the principal stresses for a point in a continuum are known, the magnitude of the normal and shear stress on an arbitrary plane can be calculated using equations (2.4) and (2.5). Similar to friction discussed previously, a shear stress failure criterion is established, so that if on the plane, τ and σ , satisfy

$$|\tau| \geq S_0 + \mu\sigma, \quad (2.28)$$

failure occurs. This is known as the famous Coulomb failure criterion. The constant S_0 is called the cohesion, and μ is the coefficient of internal friction, not to be confused with the coefficient of static friction for sliding discussed above. The failure criterion can be written equivalently in terms of the prin-

principal stresses as,

$$\sigma_1 \geq 2S_0 \left[(1 + \mu^2)^{1/2} + \mu \right] + [(1 + \mu^2)^{1/2} + \mu]^2 \sigma_3. \quad (2.29)$$

With S_0 and μ estimated for a sample, from (2.29), the compressive strengths at various confinement pressures can be obtained.

If the principal stresses meet the requirements of equation (2.29) then shear fracturing of the sample occurs. It may be of interest to calculate the angle of the fracture plane to the direction of σ_1 . The coefficient of internal friction can also be written in the form

$$\mu = \tan \varphi, \quad (2.30)$$

where φ is the angle of internal friction. By plotting the Mohr circle equations, (2.4) and (2.5), along with (2.28), in a $\tau - \sigma$ plot, θ and φ are related by,

$$\theta = \frac{\pi}{4} + \frac{\varphi}{2}, \quad (2.31)$$

where θ is the angle from the main axis to the normal of the failure plane. Consequently, the failure plane must be inclined at an angle less than 45 degrees to the main axis (σ_1). In the laboratory, these shear fractures do occur at angles very close to 45 degrees.

The Coulomb failure criterion assumes shear failure along a plane. As mentioned previously, samples may also fail in tension or from pore collapse. In addition to the Coulomb failure criterion further conditions must be explored for a complete description for the failure of a rock sample.

In the $\tau - \sigma$ coordinates, a Griffith criterion is given by the following equation,

$$\tau^2 \geq 4T_0(\sigma + T_0), \quad (2.32)$$

where T_0 is the tensile strength of the sample. Obviously, if the shear stress is zero, the criterion for failure matches the tensile strength of the rock.

Now if a large purely hydrostatic pressure is applied to a sample, it is clear that neither (2.32) or (2.28) will be satisfied. These failure criteria alone would suggest failure does not occur under purely hydrostatic pressure, which is certainly not the case. Therefore an upper limit on the hydrostatic pressure should be set as a failure criterion for the rock sample.

In practice, all failure criteria that best model a sample of rock are often collectively represented in $p-q$ coordinates. The principal stresses are transformed by equations (2.3) and (2.8) and plotted as, for an example, in Figure 2.3 ($p = \sigma_m$). The figure provides an envelope for the three dimensional stress space $\{\sigma_1, \sigma_2, \sigma_3\}$ after transformation into the $p-q$ domain. If boundary conditions are continuously applied to a rock, a stress path will follow a continuous curve in this $p-q$ domain. If or when the curve intersects the envelope, failure of the sample occurs.

2.5 Wave Propagation, Moment Tensor and Source Mechanisms

Up until now, it has been assumed that the response of a continuum due to stress results in quasi-static strain; the equations have been independent of time. When a stressed rock fails, it is of interest to study the dynamic behavior

of the sample. In particular failure causes seismic waves to propagate out from the source throughout the rock.

In the case of a planar wave, traveling within a medium far from any boundaries, the velocities of the P and S waves are,

$$V_P = \sqrt{\frac{(1 - \nu)E}{(1 + \nu)(1 - 2\nu)\rho}}, \quad (2.33)$$

$$V_s = \sqrt{\frac{E}{2(1 + \nu)\rho}}, \quad (2.34)$$

where E is the Young's modulus, ν is the Poisson's ratio, and ρ is the density of the rock. These velocities are achieved by seeking a planar solution to the non-homogenous Navier equations.

If a single particle is excited in a continuum with point force $T(t)$, the waves are non-planar, and propagate out spherically from the source. The solution to the non-homogeneous Navier equations, discussed thoroughly by Aki and Richards (2002), are then,

$$\begin{aligned} u_i(\mathbf{x}, t) = & \frac{1}{4\pi\rho} (3\gamma_i\gamma_j - \delta_{ij}) \frac{1}{r^3} \int_{r/\alpha}^{r/\beta} \tau T(t - \tau) d\tau + \frac{1}{4\pi\rho V_p^2} \gamma_i\gamma_j \frac{1}{r} T\left(t - \frac{r}{V_p}\right) \\ & - \frac{1}{4\pi\rho V_s^2} (\gamma_i\gamma_j - \delta_{ij}) \frac{1}{r} T\left(t - \frac{r}{V_s}\right), \end{aligned} \quad (2.35)$$

where the γ_i are direction cosines for \mathbf{x} and r is the radial distance from the source particle to position \mathbf{x} . The solution has three terms, with $1/r^3$ and $1/r$ relationships. The first term is a near field term as it dominates at small distances from the source, the second two terms are far field terms as they

dominate at distances far from the source. The two far field terms are the P and S waves. If measuring wave velocities one must be aware of whether seismograms are in the near or far field. It is common to assume that a distance of ten times the wavelength is sufficiently far away so that the near field term becomes negligible.

2.5.1 The Quality Factor

Different rocks have a different responses to seismicity. In general, as a wave propagates, the amplitude of a plane wave will decay due to non-geometric attenuation. In particular, energy is lost as internal energy such as heat. A quality factor, Q , can be introduced that provides a measure of attenuation. The Q factor is defined by observing the fractional change in kinetic energy over one wavelength, specifically,

$$\frac{1}{Q} = \frac{\Delta T}{2\pi T}, \quad (2.36)$$

where ΔT is the change in kinetic energy over one wavelength, and T is the kinetic energy at the beginning of the cycle. A high Q factor indicates a rock in which seismic waves attenuate slowly, whereas a low Q factor the seismic waves attenuate rapidly. In general, metamorphic and igneous rocks have high Q factors, whereas sedimentary rocks have much lower Q factors. The high porosity of the sedimentary rocks provides more room for sliding between grains leading to greater losses of mechanical energy to non conservative forces such as friction.

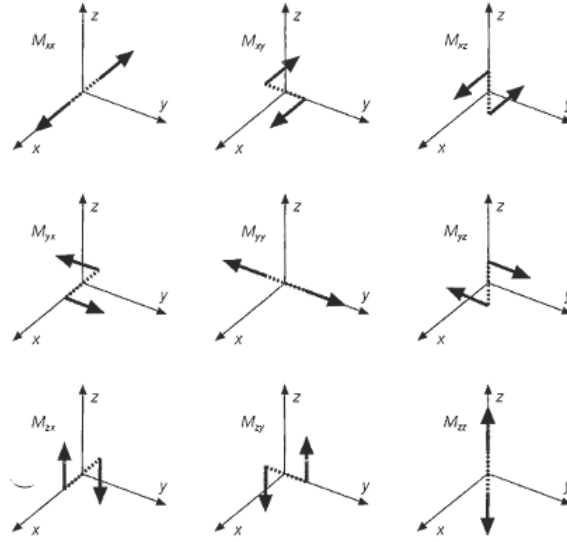


Figure 2.4: The nine force couples that make up the moment tensor. After Stein and Wysession (2003).

2.5.2 The Moment Tensor and Source Mechanisms

When rock fails, seismic waves propagate outwards from the initial disturbance. It is of interest to provide some quantification of the source mechanisms for the initial failure. Far from the source, the failure can be represented by the moment tensor. The moment tensor effectively represents the source of failure as a single point source characterized by the nine force couples shown in Figure 2.4. The force couples provide a body-force equivalent to the source mechanism. In seismology, the particle displacement at the seismogram is the convolution of the moment tensor with the Green's function. The moment tensor is often calculated from inversion of the seismograms.

From a purely mechanics driven derivation at the source, the moment tensor is,

$$M_{pq} = \iiint_V f_p r_q dV, \quad (2.37)$$

where f_p are forces per unit volume in the p -direction, r_q are the distance from

f_p to the effective point source of the source mechanism in the q -direction, and the integral is performed over some finite source volume, V .

Similar to both the stress and strain tensors, the moment tensor, \mathbf{M} can be decomposed into an isotropic part, \mathbf{M}^{iso} , and a deviatoric part, \mathbf{M}^{dev} , in particular,

$$\begin{aligned} \mathbf{M} &= \mathbf{M}^{iso} + \mathbf{M}^{dev} \\ &= \mathbf{M}^{iso} + (M_1 - M_2) \begin{pmatrix} 0 & 0 & 0 \\ 0 & -1 & 0 \\ 0 & 0 & 1 \end{pmatrix} + M^{CLVD} \begin{pmatrix} -\frac{1}{2} & 0 & 0 \\ 0 & -\frac{1}{2} & 0 \\ 0 & 0 & 1 \end{pmatrix}, \end{aligned} \quad (2.38)$$

where M_i are the principal moments, and M^{CLVD} is the coefficient of the “compensated linear vector dipole” component. The difference $(M_1 - M_2)$ is the subtraction of smallest principal moment from the largest principal moment. The second matrix in (2.38) is a purely double couple point source. The M^{CLVD} quantifies the extent to which the deviatoric part of the moment tensor differs from a pure double couple source mechanism.

If the eigenvalues from a moment tensor, \mathbf{M} , are M_1 , M_2 , and M_3 then the moment magnitude of the event can be estimated from Silver and Jordan (1982) using

$$M_0 = \frac{1}{2} \sqrt{(M_1^2 + M_2^2 + M_3^2)}. \quad (2.39)$$

2.5.3 The Hudson Plot

The moment tensor is a 3 x 3 matrix that characterizes the source mechanism following failure of a rock. In order to provide a qualitative tool for interpret-

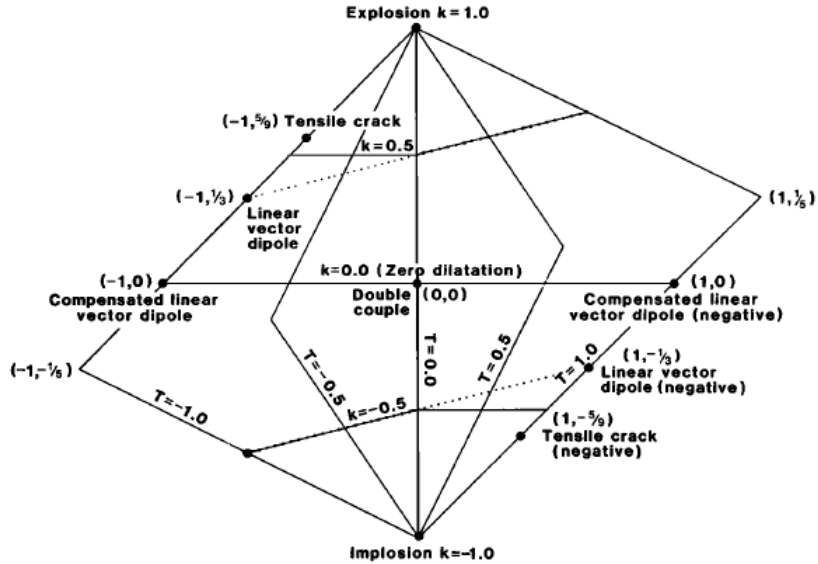


Figure 2.5: The moment tensor is represented by the two unique parameters k and T . The figure shows key points in the k and T coordinates. After Hudson et al. (1989)

ing various moment tensors it is common practice to represent each source mechanism by values k , and T and plot them on what is called a Hudson Plot. The k and T values are calculated from the eigenvalues of the moment tensor (Hudson et al., 1989). The two parameters uniquely describe a given moment tensor up to magnitude. The range of T and k is between -1 and 1. Points on the plot correspond to different types of failure at the source. See Figure 2.5 for some key failure types illustrated on the hudson plots.

2.5.4 The Gutenberg-Richter Power Law and the Fractal Dimension

A frequency-magnitude relationship was proposed by Gutenberg and Richter (1944) for earthquakes which takes the form,

$$\log n = a - bM, \quad (2.40)$$

where n is the number of earthquakes of magnitude greater than M and a and b are constants derived by linearizing the data in question. The constant b is more commonly called the b -value. Although this equation was derived for earthquakes it is now commonly applied to microseismic events. A high b -value means there are more smaller type events and a low b -value indicates larger events. Analyzing the b -value can be used to changes infer in-situ stress and the geomechanics (Grob and van der Baan, 2011).

Another statistical value of interest is the fractal dimension, D . The fractal dimension provides a characterization for the sparsity of the events. It is calculated using the spatial correlation integral method,

$$C(r) = \frac{2}{N(N-1)N(R < r)}, \quad (2.41)$$

proposed by Grassberger and Procaccia (1984), where N is the total number of events, and $N(R < r)$ is the number of event pairs within a distance r . If the distribution of the events is fractal than it will follow a power law of the form,

$$\log C(r) = C_1 + D \log r, \quad (2.42)$$

where C_1 is a constant and D is the fractal dimension. The fractal dimension, D , is a numerical value used for characterizing the sparsity of the events. D values of 1, 2, and 3 are indicative of distributions of that of a line, plane, and sphere, respectively. For example, a D value of 2 for a distribution of events would indicate the clustering of the events along a plane. For a further

discussion of the D value and its role in inferring the behavior of subsurface geomechanics, see Grob and van der Baan (2011).

Chapter 3

Numerical Modeling and the Bonded Particle Model

In the previous chapter a geomechanical review was introduced to provide the main theoretical equations often used in rock mechanics. In this next chapter numerical modeling and the bonded particle model is thoroughly discussed.

3.1 Numerical Modeling

It is of general interest to understand the behavior of rock deformation when subject to certain boundary conditions. In a traditional continuum mechanics approach, the stress field of a continuum, subject to boundary conditions, can be calculated by solving the Navier equations using a finite difference or distinct element method. The Navier equations have the inertial term equal to zero so that the stresses and strains are of a quasi-static nature. In this approach the dynamic behavior of the rock is not considered. In order to

investigate the dynamics of a continuum the non-zero inertial term must be introduced of which then the general wave equation is solved. For example, in the specific case of single particle motion, in space and time within an isotropic medium, the solutions are as in (2.35), which is of course the spherical propagation of waves. Now, it is also of interest to investigate the failure of a medium which makes the situation significantly more difficult. In order to model failure of a continuum there must be some sort of intrinsic notion of 'rock strength' (for certainly the equations of motion alone are indifferent to any sort of user defined rock strength). This starts to become troublesome. The strength of the rock is defined at a macroscopic level by conducting uniaxial compression tests. How does the UCS translate to failure on the micromechanical level? In practice, rock failure is often introduced by setting a failure criterion so that as the stress path, at a single point in the continuum, intersects a predefined failure envelope, as in Figure 2.3, failure occurs. Naturally, the next question to ask is what is the effect of failure on the displacements of individual points in the continuum? It is of utmost interest to know these displacements after failure in order to solve the non-homogeneous Navier equations and to calculate source mechanisms for failure. Producing a model that bridges the quasi-static stress/strain, rock failure and the dynamical displacements of points in the continuum is in general very complicated.

Finally, it is important to consider the micromechanisms or imperfections of the rock that may have a pronounced effect on the stress/strain, failure and particle dynamics of the system. A rock is a naturally occurring geologic material highly influenced by the nature in which it is found. Such features indigenous to an arbitrary mass of rock could include tectonic stress, faults, fractures, liquid filled pores, high temperatures, orientation of mineral grains etc. Ultimately, the effects of complex structure in a rock is very hard to

accurately model by an elastic continuum alone (Ling, 2003).

The Bonded Particle Model (BPM) is a discontinuum approach to modeling complex scenarios. It turns out, such a discontinuum-based approach for modeling rock deformation is appealing since it eliminates the need for complex constitutive failure relations required for continuum approaches (Hazzard et al., 2000). In this approach, stress/strain, failure and the dynamics of particle displacements is free to propagate naturally. The BPM is a specific implementation of the more general modeling technique known as the Discrete Element Method (DEM). The DEM employs rigid or deformable body mechanics to a discrete system of blocks, particles, or bodies where the discrete particles interact with each other through contacts. The behavior of the blocks at the contacts can be very general. Once the interaction of contacts is assessed for all particles in the system, the updated positions of the particles are found by integration of the equations of motion over the time-step or cycling parameter (Ling, 2003). The BPM is a particular example of the DEM where the discrete particles are now rigid spheres and the contact interaction between particles is elasticity described by Hooke's Law.

Before jumping into the theory of the BPM it should be briefly mentioned that these models have been used by many authors to investigate the rock mechanics of a number of scenarios. Bahrani et al. (2011) used 2D bonded particle models to investigate the strength of rock masses at different confinement levels. In particular, the authors were interested in gaining insight into civil and mining projects at large depths greater than 2km below the surface. Mas Ivars et al. (2011) investigated the mechanical behavior of jointed rock masses. Potyondy (2006) simulated stress corrosion by implementing a time-dependent damage law to the bonds in the models. He was able to successfully simulate corrosion

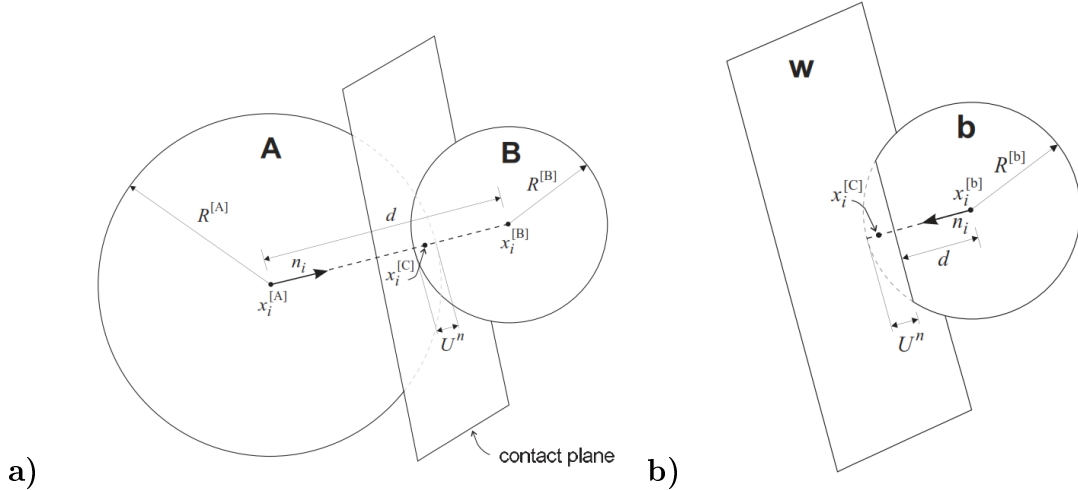


Figure 3.1: Images illustrating the contact geometry. a) Shows the ball-ball geometry. b) Shows the ball-wall geometry. Image from Itasca Consulting Group (1999).

that occurs when silicates are submerged in water. The effects of porosity and the geometry of the void space on the strength and mechanical properties of rock was investigated by Potyondy (2007). Ferdowsi et al. (2013) used a DEM type model to study microslips as a precursor to large slips. In short, there is a large amount of literature available where the BPM is used to study a number of geomechanical problems.

3.2 The Theory of Bonded Particle Modeling

For a BPM, a synthetic rock model is formulated by generating a set of randomly sized particles inside a finite domain. The interaction of these particles becomes a dynamical process with acceleration and velocity vectors of particles occurring when there are force imbalances throughout the sample. The system response of an aggregation of particles is a result of force imbalances propagating through the system as particles interact with one another.

3.2.1 Model Formulation and the Law of Motion

The particles are specifically rigid spheres, so that deformation of a macroscopic rock model is between the particles and not of the individual particles themselves. When two spheres, A and B , intersect each other, one can define an overlap by

$$U^n = R^A + R^B - d, \quad (3.1)$$

where R^A and R^B are the radii of particles A and B respectively, and d is the distance between the center of the two spheres. The unit vector, n , is in the direction from the center of particle A to the center of particle B . The contact point, x^C , is at the center of the overlap, U^n , along direction, n . Define the contact plane as a plane with unit normal, n , centered at the point x^C ; see Figure 3.1a for details. When two spheres overlap there is a force between them called the contact force, F . In general this contact force has two components,

$$F = F^n + F^s, \quad (3.2)$$

where F^n is the normal force component and F^s is the shear force component with respect to the contact plane. The normal component of the contact force is,

$$F^n = K^n U^n, \quad (3.3)$$

where $K^n = \frac{k_n^A k_n^B}{k_n^A + k_n^B}$, and k_n^i , $i = \{A, B\}$, is the normal stiffness of each particle in the contact pair. This is just a one dimensional Hooke's Law. The shear force component F^s is calculated in an incremental fashion. When the contact

is initially formed the normal force is found by the absolute overlap between the spheres, whereas the shear force, F^s , is set to zero. The increment of relative shear displacement from the initial particle position, ΔU^s , dictates the incremental contact shear force,

$$\Delta F^s = -K^s \Delta U^s, \quad (3.4)$$

where $K^S = \frac{k_s^A k_s^B}{k_s^A + k_s^B}$, and k_s^i , $i = \{A, B\}$, is the shear stiffness of each particle in the contact pair. It should be mentioned that the increment, ΔU^s , is not a simple computation; this increment must account for both rotation of the spheres around each other and the rotation of the individual spheres in reference to the Cartesian reference frame. For full details see Potyondy and Cundall (2004). Finally the contact shear force F^s is,

$$F^s = \Delta F^s + F_{prev}^s, \quad (3.5)$$

where F_{prev}^s , is the contact shear force at the previous iteration. The moments and forces on the particles, from the contact, are given by equations,

$$\begin{aligned} F^A &= -F, \\ F^B &= F, \\ M^A &= (x^C - R^A) \times F, \\ M^B &= (x^C - R^B) \times F. \end{aligned} \quad (3.6)$$

The interaction of the particles with walls is almost completely analogous. For the models that are to follow the walls exhibits only normal forces on the

balls (no shear) and therefore the walls do not exhibit any moments on the particles. The formulation is exactly as (3.3) except the K^n is an updated normal stiffness that now depends on both the normal stiffness of the particles and the walls (the stiffness of the wall is generally not the same as that of the spheres). This new K^n is calculated by

$$K^n = \frac{k_n^{wall} k_n^{ball}}{k_n^{wall} + k_n^{ball}}, \quad (3.7)$$

where k_n^{wall} and k_n^{ball} are the normal stiffnesses of the walls and spheres, respectively. The overlap U^n is now,

$$U^n = R - d, \quad (3.8)$$

where R is the radius of the sphere and d is the shortest distance from the center of the sphere to the wall; see Figure 3.1b. Plugging (3.7) and (3.8) into (3.3) provides the forces on the particles exhibited by the walls.

The forces and moments are summed over all ball-ball and ball-wall contacts in the system to compute both the net force, F_{net} , and net moment, M_{net} , which act on each individual particle. This fully describes the forces and moments acting on any given particle in the system at the beginning of any arbitrary time-step. This is the Force-Displacement Law.

The dynamic behavior of the system is achieved by a time stepping algorithm where during each time-step, Δt , the velocities and accelerations are constant. At the beginning of each time-step F_{net} and M_{net} for each particle is calculated using the Force-Displacement Law described above. If the particle has mass, a net force leads to an acceleration of the particle. An individual particle will have a radius, R , and density, ρ , from which the particle mass is derived. The

new translational velocity, v_{new} , and angular velocity, ω_{new} is,

$$v_{new} = v_{prev} + \left(\frac{F_{net}}{m} \right) \Delta t, \quad (3.9)$$

$$\omega_{new} = \omega_{prev} + \left(\frac{M_{net}}{I} \right) \Delta t \quad (3.10)$$

and the updated position of the particle is

$$x_{new} = x_{prev} + v_{new} \Delta t, \quad (3.11)$$

where v_{prev} , ω_{prev} and x_{prev} are the values from the previous time-step. This is the Law of motion for the particles. With the new positions of the particles the net forces and moments on each particle are again calculated using the Force Displacement Law. The dynamical evolution of a particle assembly is achieved by this repeated and simultaneous application of both the Force Displacement Law and the Law of motion governed by equations (3.9), (3.10) and (3.11).

For the BPM rock model just described, there are a number of user defined micro-parameters. The macroscopic response of the rock mass is governed by the particle density, ρ , the range in particle radii, the shear stiffness, K^s , and the normal stiffness, K^n . This provides the general behavior of a system of particles in the absence of additional contact models. This sort of medium behaves like a frictionless unbonded granular material. There are various other contact models that can be explored.

3.2.2 Contact Models

The contact model implemented in the chapters that are to follow is the linear contact model with the addition of the parallel bond contact model.

The linear contact model includes friction and a slip condition that limits the maximum shear force, F_s . The slip condition is as follows. If F^s , defined by (3.5), at the contact is greater than μF^n , where μ is the coefficient of friction of the two particles in contact, then the magnitude of F^s applied during the Force Displacement law is set to μF^n and slip is allowed to occur. Consequently, if the friction, μ , of the two particles in a contact are zero there will be no shear contact forces acting on the particles with the slip occurring immediately. If the friction coefficients differ between the two particles in the contact, the smaller of the two is used.

To achieve a rigid assembly of particles that behaves macroscopically similar to that of a rock there must be a “cement” that binds the particles together. The parallel bond is a contact model which provides the cementation of the particles. The bond can be envisioned as elastic springs spread uniformly across a circular area centered at the contact point perpendicular to the contact plane. The parallel bond logic is defined by five input parameters, the parallel normal stiffness, \bar{k}^n , shear stiffness, \bar{k}^s , normal strength, $\bar{\sigma}_c$, shear strength, $\bar{\tau}_c$ and bond radius, \bar{R} . With these parameters, additional forces and moments act on the two particles of the contact. In short, the parallel bond implement forces and moments that act as resistance for the two particles to both translate and rotate away from each other in both the normal and shear directions on the contact plane. Initially, the forces and moments created by the parallel bonds are set to zero with the additional forces and moments being proportional to the increments $\Delta U^s, \Delta U^n$, $\Delta \theta^s$, and $\Delta \theta^n$, where the increments $\Delta \theta^s$ and $\Delta \theta^n$ are rotations about the normal and shear directions of the contact plane, respectively. Additionally note, if the particles move away from each other, ΔU^n is negative and there is a force is created by the parallel bond that pulls the particles together. Finally, if the increments become too large, the

tensile and shear stresses on the parallel bond will exceed either $\bar{\sigma}_c$ and $\bar{\tau}_c$ so that the bond will fail in either a normal (tensile) or shear fashion. For a more thorough discussion and rigorous formulation of the parallel bond see Potyondy and Cundall (2004).

The parameter space for the models (including both the contact logic and the parallel bonds) is, R , the radius of a sphere, k_n , k_s , the contact normal and shear stiffness, respectively, the coefficient of friction, μ , the normal and shear stiffness of the parallel bonds, \bar{k}^n , and \bar{k}^s , respectively, the tensile and shear strength, $\bar{\sigma}_c$, and $\bar{\tau}_c$, respectively, and finally the particle density, ρ . It should be noted that for the contacts it is common to define a ratio, k_n/k_s , and a micro Young's modulus, E_c . Similarly for the parallel bonds a ratio, \bar{k}^n/\bar{k}^s , is defined along with another micro Young's modulus, \bar{E}_c . The relationship between these Young's moduli and the stiffnesses is found using the following formulas,

$$k_n = 4RE_c, \quad (3.12)$$

$$\bar{k}^n = \frac{\bar{E}_c}{R^A + R^B}, \quad (3.13)$$

where R is the radius of the sphere, and R^A and R^B are the radii of the two particles comprising the parallel bond. This formulation allows for different stiffnesses for each particle in the model and allows different bond stiffnesses for all the parallel bond pairs in the model. Additionally, it turns out choosing these micro Young's moduli provides a good starting estimate for the macroscopic Young's modulus of the sample aiding with the calibration process. Finally, instead of assigning a single parallel bond radius, \bar{R} , for every

parallel bond pair in the model, individual radii for a given pair is calculated as $\bar{R} = \bar{\lambda} \min(R^A, R^B)$, where $\bar{\lambda}$ is a user-defined input parameter. The full parameter space for the bonded particle model is $\bar{\lambda}, E_c, k_n/k_s, \bar{E}_c, \bar{k}^n/\bar{k}^s, \mu, \bar{\sigma}_c$ and $\bar{\tau}_c$. These will be the input parameters mentioned for any of the calibrated samples within this thesis.

With the above formulation, an assembly of particles can deform freely responding to boundary conditions with bonds being broken to represent local failure.

In principle, when a system of particles is generated within a region bounded by walls, cycling a number of time steps should cause the forces throughout the medium to balance. In practice, after cycling for many time cycles, there are small unbalanced forces on the particles. This is a symptom of the discrete nature of the BPM. A damping parameter is introduced to keep these unrealistic unbalanced forces as small as possible and to provide another mode for attenuation (other than friction).

3.2.3 Damping of the System and the Quality Factor

In order to dissipate kinetic energy within the models a damping parameter is introduced. The damping creates a fictitious force, F_D , that opposes the net unbalanced force, F_{net} , on all particles in the model. The force is calculated by,

$$F_D = -\alpha |F_{net}| \text{sign}(V), \quad (3.14)$$

where α is the damping parameter, and $\text{sign}(V)$ is the direction of the velocity of the particle. The damping force always acts to oppose the direction of the

motion and is proportional to the net force on the particle calculated by the Force-Displacement Law. Assuming a single mass spring system, with total energy of the system W , subject to F_D it can be shown that over one cycle

$$\frac{\Delta W}{W} = 4\alpha, \quad (3.15)$$

regardless of the rate at which the cycle is executed (Itasca Consulting Group, 1999). The equation is derived by breaking down the cycle into cases that depend on the velocity and acceleration of the mass and then by examining changes in kinetic energy. Plugging (3.15) into (2.36) yields

$$Q = \frac{\pi}{2\alpha}. \quad (3.16)$$

This equation provides an estimate for the damping parameter needed to match the wave attenuation parameter, Q , of a rock.

3.2.4 The Moment Tensor

If the tensile or shear stress exceeds the maximum tensile or shear strength of the parallel bond a breakage will occur. The bond breakages leave unbalanced forces on all particles neighboring the source breakage. By monitoring changes in forces it is possible to model source mechanisms for the failure. Hazzard and Young (2004) created an algorithm that extracts the moment tensors for such failure.

When a bond breakage occurs in the BPM the broken parallel bond is considered a single crack occurring between two particles. The moment tensor for a single breakage is calculated by measuring the changes in contact forces at

all contacts, C^i , surrounding the two particles for the duration of the event. The duration of the event is calculated by assuming the slowest possible fracture propagation velocity is half the speed of the shear wave velocity, V_s . The number of cycles for an event is then,

$$T_{steps} = \frac{2r_{avg}}{(V_s/2)} \times \frac{1}{\Delta t} \quad (3.17)$$

where r_{avg} is the average radius of all balls in the sample. As will follow shortly, the Young's modulus and Poisson's ratio of the sample can be measured by conducting triaxial tests on the BPM from which the shear wave velocity of the sample can be estimated from (2.34). At each time-step the contact force at a given contact, C^i , is subtracted from the initial contact force prior to the bond breakage to measure the change in contact force, $\Delta \mathbf{F}^i = (\Delta F_1^i, \Delta F_2^i, \Delta F_3^i)$. The moment tensor, \mathbf{M} , is calculated from (2.37), where this integral is now a discrete summation over all C^i . The distance $\mathbf{r} = (r_1, r_2, r_3)$ is the distance from the contact point of each C^i to the location of the event (which is the contact point of the initial crack). The moment tensor is then

$$M_{pq} = \sum_i \Delta F_p^i r_q. \quad (3.18)$$

The magnitude of each \mathbf{M} (calculated at each time-step) is obtained from (2.39). The moment tensor of the event is the \mathbf{M} which produces the largest magnitude over the duration of the event.

As the the standard deviation on the average size of the spheres in the samples are relatively low, any single bond breakages between two bonded spheres will have similar magnitudes (The net forces following the breakages are similar as the masses are similar). In order to model a broad range of magnitudes of

events, a rupture must be defined. A rupture is defined as a larger event that includes multiple cracks. The rupture occurs when there are multiple cracks that occur within close proximity of the initial crack. Specifically, a new crack must share one of its particles with a crack already within the rupture and must have occurred within T_{steps} since the most recent crack. In this fashion a rupture is a coalescence of many bond breakages. The larger magnitude event is complete when no new crack occurs within proximity of the existing cracks after T_{steps} cycles have elapsed. The moment tensor is calculated in exactly the same fashion using (3.18), except the contacts C^i now include all contacts surrounding all particles involved in all of the bond breakage pairs within the rupture and the event location is the geometric centroid of the cracks. Completely analogous to a single crack event, the moment tensor of the event is the \mathbf{M} which produces the largest magnitude over the duration of the event.

3.2.5 Energy

Boundary conditions (forces) applied to particles within the BPM provides a net input of energy into the system. As the model is cycled forward it is of interest to track this energy throughout the system. The input energy will end up as either kinetic energy, potential energy, or dissipated energy from the non conservative forces such as friction or damping.

The boundary work is the work done by the walls on the sample. The boundary work is calculated by first summing up all contact forces between each wall and the particles in contact with it. The work conducted by a single wall is then just this resultant force multiplied by the displacement of the wall over one time-step. The work is then summed up over all walls in the system, and then

summed over all time-steps. The kinetic energy of the system at any given time is calculated by summing the translational and rotational kinetic energy of the particles in the system. The frictional work is obtained by multiplying the force of friction, μF^n , with the slip distances, at all contacts in the system, and then summed over all time-steps. The strain energy in the system is found by elastic potential energy calculations of the balls where the spring constant in the Hooke's Law formulation is simply the normal and shear stiffness of the spheres. Specifically, the strain energy stored in the contacts is then,

$$E_{strain} = \frac{1}{2} \sum (|F_i^n|^2/k_n + |F_i^s|^2/k_s). \quad (3.19)$$

Similarly the parallel bond energy can be found using Hooke's Law where the spring constant is the normal and shear stiffness of the parallel bonds. The strain energy for the parallel bonds is a little more complicated (as there is rotational elasticity) but can also be calculated directly. For the calculation of the parallel bond energy, E_{pb} , see Itasca Consulting Group (1999). Unfortunately, energy lost to the damping of the system is not monitored. As will follow shortly, various components in the energy balance will be evaluated to investigate relationships between total input energy and that released via brittle failure (microseismic events) in triaxial deformation experiments.

Chapter 4

Assembly and Calibration of the Bonded Particle Models

The samples simulated using the BPM are idealized as an aggregation of numerous bonded overlapping spheres. Before discussing calibration it is necessary to provide some insight into both the packing geometries and porosities of created specimens.

4.1 Spherical Packings

Spherical packing is a problem that dates back to Johannes Kepler when he pondered what arrangement of identical spheres gives the maximum density of a volume (http://en.wikipedia.org/wiki/Sphere_packing). A spherical packing is an arrangement of spheres in three dimensional space in which there is no overlap of the spheres. It is now well known and proven that the maximum possible density for a spherical packing is approximately 0.747 leading

to a porosity of 0.253 (D. Weaire, 1999). Such a packing is anisotropic as the contacts between spheres are not homogeneous in every direction (for example in one direction there may be a contact, and in another direction there is no contact). Such an anisotropic packing cannot be fully described by the two elasticity parameters E and ν . For the models that are to be created the packing should reflect an isotropic medium. In order to achieve this packing the radii of the spheres must not be identical and so a range of radii is chosen. Danian and Jinmin (1991) conduct numerous experiments on random packings of unequal and equal sized spheres. The lowest porosity they achieve by mixing different sized spheres is around 0.35. Denton (1957) extensively studied spherical packings in which he conducted a number of laboratory experiments. After random packings on identical sized spheres he found a mean porosity of 0.391 across all experiments. Murphy (1982) conducted a number of random packing experiments on non-identical spheres and obtains a porosity as low as 0.20. In general if one is to achieve a low porosity packing a range of radii must be chosen. Although the bonded particle models do allow overlap of the particles a range of particle sizes must also be chosen to keep the porosities as low as possible and the elasticity of the medium isotropic.

4.2 Material Genesis

The bonded particle model is an aggregation of an arbitrary number of packed spheres that are then bonded using the parallel bond logic discussed in Subsection 3.2.2. For the following simulations the outer boundaries of the samples are cylindrical walls or rectangular prisms, see Figure 4.1a. In general, more complicated containers can be created, but will not be investigated here. An arbitrary number of spheres are randomly generated within the boundaries of

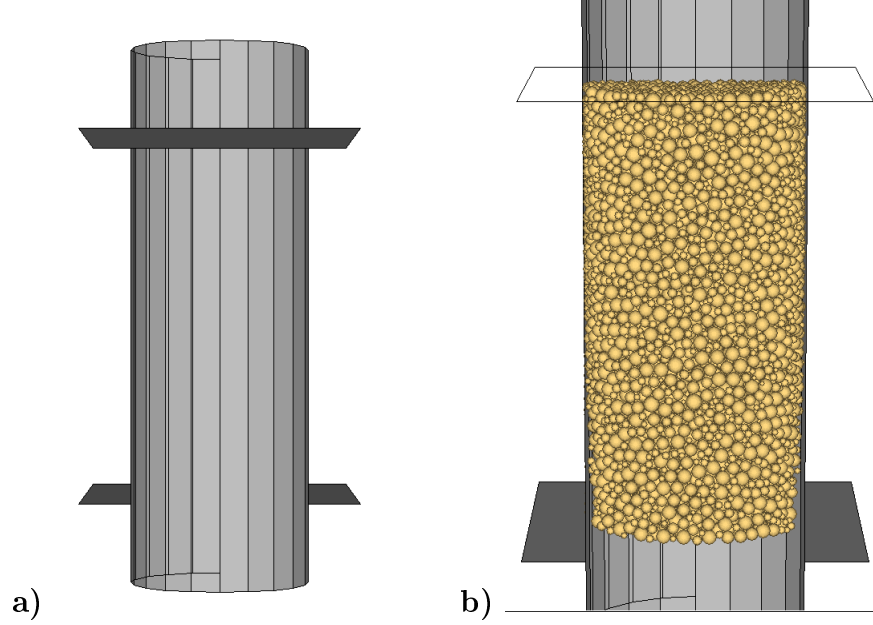


Figure 4.1: a) The cylindrical cylinder that is the container for the bonded particle models. b) An example of a system of particles generated in the confines of walls.

a cylindrical sleeve with initially no friction between the particles. The radius and height of the cylinder is 0.005 m and 0.02 m, respectively. Upon placement of the spheres, the size of the spheres are kept very small so that there is no initial overlap. The spheres are placed using a random number generator where the seed feeding the random number generator can be altered at the user's request. With the spheres placed within the confines of the boundary surface an algorithm expands the radii of the sphere to reach an initial input porosity of 0.35. The number of particles generated is dictated by the user-defined input parameters, R_{min} and R_{max} , the minimum and maximum radii of the balls respectively. Values for R_{min} and R_{max} are chosen so that there is no less than 10,000 particles within the confines of the cylinder. A uniform distribution of particles sizes is implemented. The number of particles is

$$N = \frac{3V(1 - n)}{4\pi(R_{min} + R_{max})^3}, \quad (4.1)$$

where V is the volume of the cylinder/prism, and n is the porosity of the sample. To achieve the packing, a radius multiplier, m , is computed,

$$m = \left(\frac{1 - n}{1 - n_0} \right)^{1/3}, \quad (4.2)$$

where n_0 is the porosity of the sample immediately following the initial generation. All spheres are multiplied by m to achieve the input porosity. The system is cycled forward to reach static equilibrium creating the initial compact assembly.

It is important that the contact forces between the particles be as close to uniform as possible. The magnitude of the forces in all directions for any given particle in the sample should be about the same. The radii of the particles in the sample are altered to achieve a uniform isotropic stress, σ_0^t . The value, σ_0^t , is found by measuring the local mean stress. The desired isotropic stress of the sample must be set low in comparison to the material strength. In general, the isotropic stress should be lower than one percent of the UCS (Itasca Consulting Group, 1999). The low isotropic stress is essential to reducing any unrealistic locked in forces. When the initial packing of the spheres is created, the contact forces from the overlap of the particles try to push the particles out from each other. The parallel bond holds the particles in place but these contact forces remain as locked in forces.

At this point in the material genesis process there tends to be a few particles in the sample that are not in contact with the main assembly. These spheres are generally quite small and are called floaters. An algorithm expands all the floaters in the sample until they come in contact with at least two particles (but only to the point so as not to exceed the desired uniform isotropic stress). Finally, the material genesis is complete with the addition of the parallel bond

logic. The assembly now represents a hard rock and is ready for compression tests and calibration. For more explicit details see Itasca Consulting Group (1999). See Figure 4.1b for an example of a sample ready for calibration.

4.3 Compression and Tensile Tests

Once a sample has been created the next step is to investigate its macroscopic properties. As described in Chapter 2, Section 2.2, uniaxial tests, triaxial tests, and Brazilian tests are applied to the samples. For uniaxial tests, the radial wall of the cylinder is deleted so that only the upper and lower platens act on the sample. The platens are accelerated to a user input velocity resulting in axial stress and strain of the model. The axial stress, strain, and radial strain are recorded during the elastic loading of the sample from which E and ν are derived (using equations (2.21) and (2.22)). The axial stress is calculated by summing the contact forces across the wall and dividing by the area. The axial strain is measured from the displacement of the platens. In the case of the unconfined tests, the radial strain is measured by gauge balls (the displacements of a number of spheres within the sample are measured to derive the axial strain). The maximum axial load obtained during the simulation is the UCS of the sample.

For the triaxial simulations, the confining cylinder is used as a means of generating stress on the sample. A servo algorithm is implemented that changes the radial velocity of the cylinder to match the desired radial confinement of the triaxial experiment. Completely analogous with the unconfined simulations, the radial stress, radial strain, axial stress, and axial strains are recorded during the elastic regime of the loading cycles to derive elasticity parameters using

equations (2.21) and (2.22).

Finally the tensile strength of the sample is measured by conducting Brazilian tensile tests. The tensile strength is calculated from (2.24) where R is the radius of the cylinder and W_c is the point load on the sample. The point load, W_c , is implemented by applying two planar walls as in Figure 2.2a and is measured by summing all of the contact forces along these walls. For more specific details regarding the algorithms that are used to conduct these tests see Itasca Consulting Group (1999).

4.4 Porosity

In general, there is a relationship between the porosity of the sample and its elasticity parameters, tensile strength, and compressive strength. Unrealistic porosities may produce unrealistic macroscopic parameters, and in turn the micro-parameters must be varied in order to achieve the proper behavior. Potyondy (2007) finds both the Young's modulus and peak compressive strength decrease with increased void space.

The initial porosity of a packing is achieved by applying the radius multiplier from (4.2) to all particles in the sample. Unfortunately, regardless of this initial porosity the isotropic stress algorithm tends to create porosities of the samples very close to around 0.356. A number of tests are conducted with various ranges in particle radii; see table 4.1. In regards to sedimentary rocks in general, a porosity of 0.356 is very high and unlikely to be found in nature (with perhaps the exception of an unconsolidated sandstone or conglomerate). Real rocks will have a much lower porosity; sandstones deep in the subsurface are under great pressure from the overburden and may have porosities

Table 4.1: Relationship between the range of radii and initial and final packings after implementation of the material genesis algorithm described by Potyondy (2004).

$\mathbf{R}_{max}/\mathbf{R}_{min}$	Initial Porosity	Final Porosity
2.8	0.304	0.359
5.0	0.305	0.349
10.0	0.301	0.344
15.0	0.304	0.339

lower than 5%. Mature sedimentary rocks far along in their diagenesis will have porosities substantially lower than 0.356. So in general oil and gas reservoirs are very unlikely to have such a high porosity. In this thesis we ignore this fact but a non-uniform distribution with a mean average skewed toward smaller particle sizes could possibly produce lower porosities. Alternatively, non-spherical or clumped particles could be considered but at significantly increased computation times.

An algorithm was implemented to make an attempt at reducing the porosity of the samples in the hopes of better modeling rock found in nature. The algorithm acts on a sample created by the material genesis routines discussed previously. A particle in the sample is randomly selected, p_1 . Two numbers are then randomly selected using a uniform distribution between 0 and 2π . These two numbers are then projected onto the unit sphere by,

$$R(\theta, \phi) = (\sin\theta\cos\phi, \cos\theta\cos\phi, \sin\phi). \quad (4.3)$$

Equation (4.3) then provides a random direction in three dimensional space. Next, unit vectors are obtained for the directions to all spheres in contact with the selected particle p_1 (these unit vectors are called contact vectors). The neighbouring spheres are found by running through a linked list of contacts

for the particle p_1 (these are tracked for all particles in the models). The angles between the random vector and contact vectors are found. If the angle between a contact vector and the direction vector is greater than a set angle, a new sphere is placed. In this fashion new particles are randomly introduced into the void space of the assembly. The floater routines discussed previously are then applied. If there are any remaining floaters, all non-floaters are then locked in position (by manually forcing their positions to be fixed) while the remaining floaters are expanded in size. The simulation is cycled forward. The floaters are then pushed towards the lowest possible energy state. The contact forces of the particles are monitored. If they are too high, their radii are reduced in the attempt of maintaining the desired isotropic stress, σ_0^t , set during the original genesis of the sample.

Samples with porosities as low 0.10 are achieved by inserting smaller particles into the existing void space of the models. In principle even lower porosities can be obtained, but the number of particles becomes quite large and the simulations tend to be quite computationally expensive. Figure 4.2b shows the stress strain curve of a 10 MPa triaxial test on a sample with a porosity of 0.245. The initial stress strain curve of the sample before the addition of particles is in Figure 4.2a. The uniaxial tests results are in Table 4.2. The curve in Figure 4.2b initially shows irregular non-elastic behavior. This is likely a result of the sample being poorly connected with locked in forces unevenly distributed through the system. Also, reducing the porosity produces an increase in the compressive strength of the sample by about 15 MPa. The porosities of the models are definitely related to their overall strength. Decreasing the porosity provides additional grains for spreading out any applied load (the average magnitude of the force chains are reduced). Ideally, for the most realistic sandstone describing conventional oil and gas reservoirs, the porosities should

Table 4.2: Triaxial Experiment Results

	Porosity 0.3748	Porosity 0.2457
Peak Stress	175.15 Mpa	191.14 Mpa
E	17.88 Gpa	17.104Gpa
v	0.25718	0.1738

be close to 0.15-0.25; for unconventional reservoirs porosities can be as low as 0.05-0.08. However, for the models used throughout, no attempt is made to adjust the high porosities. The main concern with reducing the porosities is that it is computationally expensive and that the force chains may be disturbed affecting the overall isotropy of the sample.

4.5 Sample Calibration

After the material genesis is complete, appropriate micro-parameters need to be determined. In general, it is not intuitive as to what micro-parameters should be chosen to achieve the overall desired macroscopic behavior. The micro-parameters that determine the macroscopic behavior of the unbonded models are R_{min} , R_{max} , σ_0^t , ρ , k_n/k_s , E_c , and μ , which were discussed in Chapter 3 Section 3.2.2. With the parallel bond logic there are the five additional parameters, \bar{k}^n/\bar{k}^s , \bar{E}_c , $\bar{\sigma}_c$, $\bar{\tau}_c$, and $\bar{\lambda}$ (also discussed in Chapter 3 Section 3.2.2). If one wishes to model a sandstone these micro-parameters must be chosen in such a way to produce a sample with the proper elasticity constants, unconfined compressive strength, angle of internal friction, and tensile strength. In reality there is no simple way of determining appropriate micro-parameters. The micro-parameters must be tweaked in such away so that the model matches experimental data. In general the technique is to run uniaxial tests to first match the Young's modulus of the sample and then match the

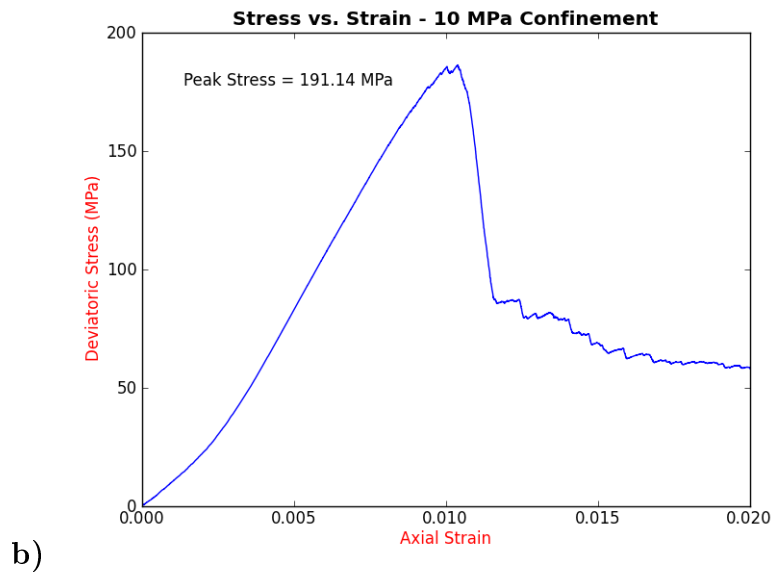
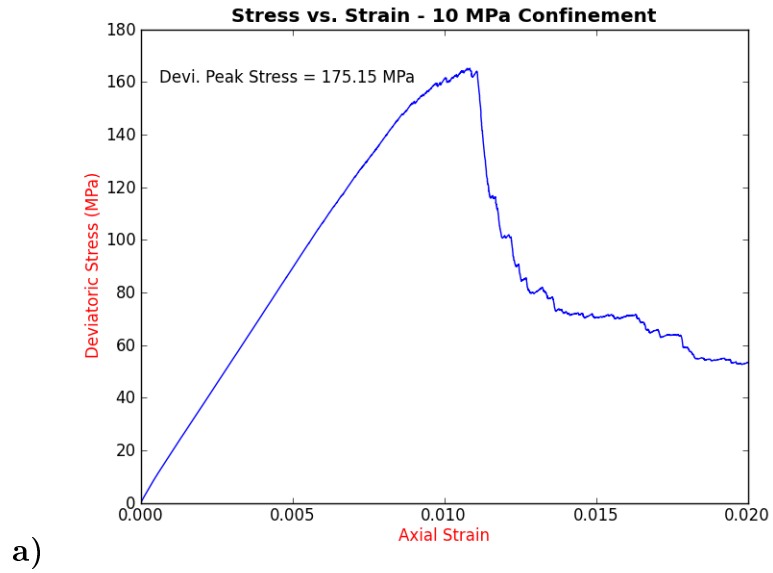


Figure 4.2: a) Initial system with 2658 balls, porosity is 0.3748. b) System after balls randomly inserted, now 14949 particles, porosity is 0.24567.

Poisson's ratio. Once the elasticity constants are set, the strength of the sample is altered by changing the parallel bond strengths. Post peak behavior is tweaked by altering the friction coefficient. The initial micro Young's moduli are chosen as values close to the desired macroscopic Young's modulus.

In the following section a sample is created and calibrated to laboratory tests conducted by P. E. Senseny (1983) on sandstones from the Piceance Basin. A cylindrical sample of diameter 0.01m and height 0.02m is calibrated to match a sandstone with compressive strength of 175.6 MPa, $E = 39.6GPa$, and $\nu = 0.26$. The tensile strength of the sandstone is -13.77 MPa.

After several uniaxial tests, while tweaking various micro parameters, the sample is calibrated to a peak stress of 174.9 MPa, $E = 39.0 GPa$, $\nu = 0.26$. See Figure 4.3 for the stress strain curve from the uniaxial test. The curve shows elastic deformation of the sample until abrupt brittle failure occurs as the axial stress rapidly drops. The elastic regime of the curve is very stiff showing minimal hardening at the beginning of the simulation. In practice, uniaxial tests conducted in the laboratory display initial non linear behaviour as depicted in the idealized curve from Figure 2.1a. The algorithm used in the material genesis of these models implements homogenous, well connected, contact forces throughout the sample whereas in reality rocks are generally quite heterogeneous. This is likely the main reason for the stiff behaviour observed at the onset of the simulations on the bonded particle models. A Brazilian tensile test is then conducted on the sample with a result of 49.9 MPa. The tensile strength of the sample is approximately 3.6 times stronger than the actual sandstone. It is a well documented fact that if a bonded sample is calibrated to a set of elasticity parameters and compressive strength, the tensile strength of the particulate will be much stronger than that of which is desired (Po-

Table 4.3: PFC3D microproperties for sandstone, where $\bar{\lambda}$ is the parallel bond radius, E_c is the micro Young’s modulus of the particles, \bar{E}_c is the micro Young’s modulus of the parallel bonds, \bar{k}_n is the normal stiffness of the parallel bond, \bar{k}_s is the shear stiffness of the parallel bond, $\bar{\sigma}_c$ is the normal parallel bond strength, and $\bar{\tau}_c$ is the shear parallel bond strength.

Grains (particles)	Cement (bonds)
$\rho = 3400\text{kg/m}^3$	
$R_{max}/R_{min} = 2.8$	$\lambda = 1.0$
$E_c = 37.9\text{GPa}$	$\bar{E}_c = 38.9\text{GPa}$
$k_n/k_s = 1.9$	$\bar{k}_n/\bar{k}_s = 1.9$
$\mu = 0.6$	$\bar{\sigma}_c = \bar{\tau}_c = 156 + 35\text{MPa}$

tyondy, 2012). In short, this is a side effect of all particles being spherical, and non-granular. Grain/clump based models exist and flat jointed models are being researched in attempt to better model both the compressive and tensile strengths of a desired rock (Potyondy, 2011). For the following experiments no attempts have been made to specifically calibrate the tensile strength of the samples as such grain/clump-based models significantly increase the computation times.

The micro-parameters for this calibrated sandstone are $R_{min} = 0.00014m$, $R_{max} = 0.000392m$ and $\sigma_0^t = 1.0 \times 10^6 Pa$. The rest of the micro-parameters are in Table 4.3.

4.6 Triaxial Tests

Triaxial tests are conducted on the created sample at varying confinement pressures to obtain the stress envelope. Tests are conducted at 10, 20, 30 and 50 MPa. These are compared with the compressive strengths from the laboratory experiments conducted by Senseny (1983). There is some discrepancy between the simulations and laboratory results. However, the numerical sim-

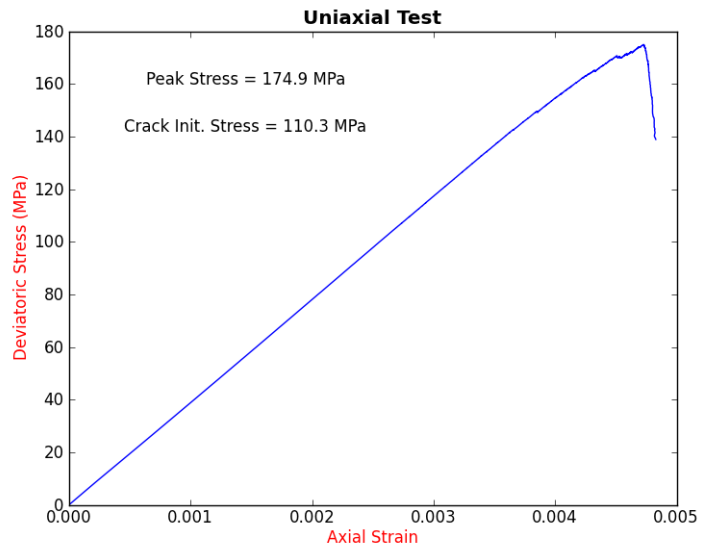


Figure 4.3: Stress strain curve for uniaxial test on calibrated sandstone.

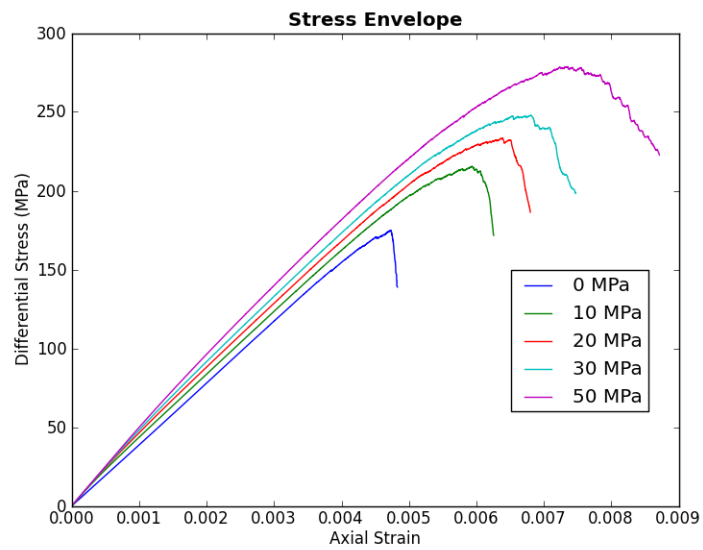


Figure 4.4: Stress vs strain curves at different confinement pressures.

Table 4.4: Laboratory results at different confinement pressures for sandstone from the Piceance Basin (Senseny 1983).

Confinement Pressure	Laboratory Results	Young's Modulus	Poisson's Ratio
0 MPa	175.6	39.6	0.26
10 MPa	200.5	36.2	0.18
20 MPa	240.2	36.3	0.20
30 MPa	277.1	37.5	0.19
50 MPa	427.6	44.8	0.26

Table 4.5: Numerical results

Confinement Pressure	Numerical Simulations	Young's Modulus	Poisson's Ratio
0 MPa	174.9	39.0	0.26
10 MPa	225.4	46.6	0.16
20 MPa	253.3	43.1	0.19
30 MPa	277.9	44.6	0.17
50 MPa	328.7	46.6	0.16

ulations do show the increased peak strength with increasing confinement of the sample (see Figure 4.4). With the exception of the 50 MPa simulation, the numerical results are in close agreement with the laboratory tests conducted on the Piceance sandstone (see Tables 4.4 and 4.5). The 50 MPa laboratory confinement peak stress seems quite high and the Poisson's ratio is quite a bit off.

The model sandstone is now calibrated and is ready for the simulations and analysis that is to follow in chapters 5, 6, and 7.

Chapter 5

Brittle Deformation and its Associated Microseismicity

In the previous chapters the geomechanics and bonded particle modeling theory was introduced so that the models are now in a position to answer some of the key topics discussed in the introduction. This chapter is divided into two main parts where the first section is an article that was published in *The Leading Edge* (Chorney et al., 2012). The sample calibration was completed by P. Jain, the simulations of the models along with the geomechanical interpretation was conducted by D. Chorney, the microseismicity analysis was done by M. Grob, and final revisions by M. van der Baan. The second article further develops topics discussed in the *Leading Edge* article and is a draft for submission to *Tectonophysics*. The initial outline was drafted by M. Grob. All simulations conducted by D. Chorney. The microseismicity analysis was done by M. Grob. The bonded particle model theory written by P. Jain. The focus of this chapter is on brittle deformation and its associated microseismicity. Following the two articles is a general discussion.

5.1 Geomechanical Modeling of Rock Fracturing and Associated Microseismicity

5.1.1 Introduction

Microseismic monitoring is increasingly being used to assess in real time the effectiveness of hydraulic fracture treatments. Operators are interested in three key questions. (1) Where are the microseismic events occurring (what is the size of the microseismic cloud)? (2) What is the failure mechanism (are fractures opening, closing or shearing)? (3) Why is failure occurring in specific locations but not others (why are fractures not always symmetric with respect to the injection well and what is the geomechanical behavior of the reservoir)? In particular, the last question is difficult to answer from the recorded seismicity alone since the geomechanical behavior depends on the in situ stress field, the local rock properties (lithologies), and any existing areas of weakness including faults, fractures and joints (Grob and Van der Baan, 2011). Geomechanical modeling can thus play a key role in better understanding both brittle and ductile deformation inside a reservoir due to hydraulic fracturing and the resulting microseismicity. Bonded-particle modeling (BPM) is becoming an important computational tool for modeling the complex dynamical behavior of rocks rupturing given a set of boundary conditions (Potyondy and Cundall, 2004). Rocks are modeled as the aggregation of (typically) thousands of bonded spherical particles with the goal of reproducing the macroscopic properties of the material and possibly additional features such as microseismicity. This method allows the modeling of realistic materials by specifying appropriate intrinsic particle properties as well as inter-particle (bond) properties. Rupture is modeled through the breaking of the bonds that link the particles

(Hazzard et al., 2000). Thus it is only the material properties, primarily the bond strength, which determine the size and shape of a rupture, providing a clear link between the geomechanics occurring in a reservoir and the recorded microseismicity. The resulting source mechanism is inferred from the type of bond breakages (normal or shearing) and their temporal and spatial evolution. A bonded-particle method therefore allows one to investigate in a controlled fashion the interaction of geomechanical reservoir behavior, rock properties, in situ stress field, existing fractures and the resulting microseismic event locations, source mechanisms and both seismic (brittle) and aseismic (plastic) deformation. Here we demonstrate the utility of the method by simulation of triaxial compression tests using calibrated sandstone models. Specifically, the models are tested with and without the introduction of a circular plane of weakness. The kinetic energy in the system is monitored and moment tensors for the failure mechanisms are extracted. The models show fault nucleation in the post peak stress regime for homogeneous samples and localization of bond failures at the edges of the joints for the samples with the circular planes of weakness. The kinetic energy from the bond breakages is compared with the radiated energy, the discrepancy between them being about two orders of magnitude.

5.1.2 Bonded Particle Model

A synthetic rock model is formulated by generating a set of particles inside a finite domain, and specifying the contact properties for inter-particle bonds (Potyondy and Cundall, 2004; Figure 5.1a). Parallel bonds are used to specify the interactions between two particles in contact and are representative of cementation between the two adjacent particles. This “cement” allows both

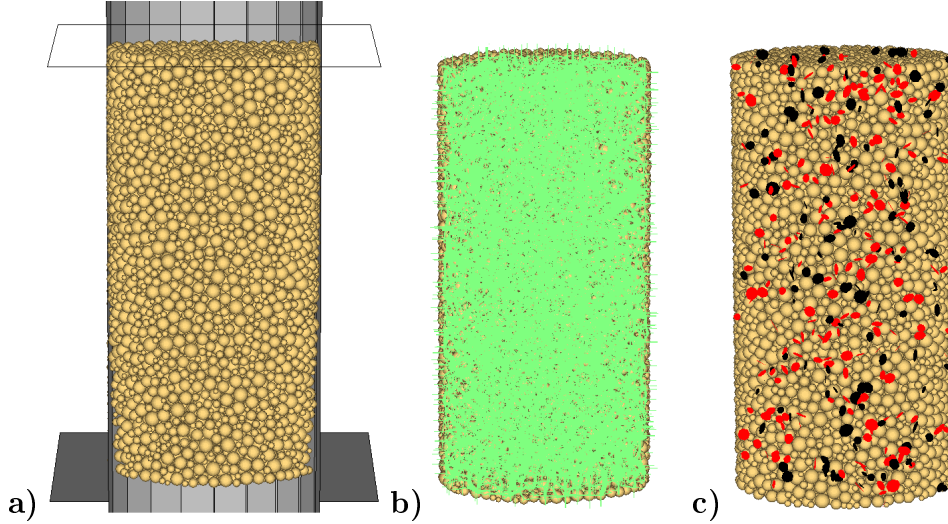


Figure 5.1: Images of the calibrated sandstone. a) The assembly sample showing the confining walls. b) The force chains between particles shown in green before compression. c) The bond breakages after stress has been applied to the assembly (normal bond breakages in red and shear bond breakages in black).

forces and moments to be transmitted over a finite area (either circular or rectangular). The force on each ball (Figure 5.1b) is linearly proportional to the displacement between the balls (ie. linear springs). The force can be resolved into normal and shear components, with coefficients of proportionality given by the normal stiffness k_n and shear stiffness k_s respectively. Parallel bonds allow for both compressive and tensile forces depending on the sign of the contact displacement. The intrinsic ball properties include the density ρ (kg m^{-3}), radius r (m) and friction μ (dimensionless). This assembly of particles can deform freely and bonds can be broken to represent local failure (Figure 5.1c). Bonds are characterized by normal and shear strengths, and together with the friction coefficients, are used to model tensile and shear failure. Such a discontinuum-based approach seems more appropriate to model rock deformation through failure since it eliminates the need for complex constitutive relations required for continuum approaches (Hazzard et al, 2000).

To simulate the behavior of an interface, BPMs can use a smooth-joint con-

tact model (for an overview, see Ivars et al., 2011). The essential idea is that particles can slide past one another along a plane irrespective of particle size or contact orientation. The smooth joint reduces the effect of the local topography or rugosity intrinsic of a plane composed of spheres.

Finally, with all parameters set, the dynamical evolution of a particle assembly is achieved by the repeated and simultaneous application of both a force-displacement relation and integration of Newton’s second law to calculate new particle velocities and positions after a small time increment. For a more thorough discussion of the theory behind the BPM, see Potyondy and Cundall (2004).

An essential first step is model calibration, which is achieved by comparing compression and fracture simulations with known properties of materials measured from equivalent laboratory tests. Here the micro-parameters of the BPM simulation (i.e. particle and bond properties) are “tuned” until the desired behavior of the assembly is attained.

We simulate a cylindrical sample of sandstone with height 20mm and radius 5mm, using a parallel-bonded model. By performing unconfined triaxial tests, the model is calibrated to a Young’s Modulus, E , of 14.5 GPa, and Poisson’s Ratio, ν , of 0.30. The unconfined peak stress of the sample, σ_f , is 105 MPa, with a crack initiation stress, σ_{ci} , of 47 MPa. For this model, the crack initiation stress occurs when the number of bond breakages is 5% of the total breakages at peak stress. The following macroscopic properties are obtained using the procedures outlined in Potyondy & Cundall (2004). See Tables 5.1 and 5.2 for in-depth parameters of the calibrated sample.

A general comment is in order regarding the tensile strength of parallel-bonded particle models. It is well documented that for a bonded sample calibrated to

Table 5.1: PFC3D microproperties for sandstone, where $\bar{\lambda}$ is the parallel bond radius, E_c is the micro Young’s modulus of the particles, \bar{E}_c is the micro Young’s modulus of the parallel bonds, \bar{k}_n is the normal stiffness of the parallel bond, \bar{k}_s is the shear stiffness of the parallel bond, $\bar{\sigma}_c$ is the normal parallel bond strength, and $\bar{\tau}_c$ is the shear parallel bond strength.

Grains (particles)	Cement (bonds)
$\rho = 3000\text{kg/m}^3$	
$D_{max}/D_{min} = 2.8$	$\lambda = 1.0$
$E_c = 16\text{GPa}$	$\bar{E}_c = 16\text{GPa}$
$k_n/k_s = 8.423$	$\bar{k}_n/\bar{k}_s = 8.423$
$\mu = 0.5$	$\bar{\sigma}_c = \bar{\tau}_c = 112 + 33\text{MPa}$

Table 5.2: Macroproperties from uniaxial tests.

Property	PFC ^{3D} Calibrated Sample
E (GPa)	14.5
ν	0.30
σ_f (MPa)	105
σ_{ci} (MPa)	47
ρ (kg/m ³)	1920

a set of elasticity parameters and compressive strength, the tensile strength of the sample is overestimated (Potyondy, 2011). This is a limitation of the model, which uses spherical as opposed to more realistic granular particles. Grain/clump based models and flat jointed models attempt to better model both the compressive and tensile strengths of rock samples (Potyondy, 2012). Therefore, in the following simulations the tensile strength of the sample is higher than that of a sandstone, by an estimated 5-6 times. As rocks under compression tend to fail first by tensile fracturing, the samples will be somewhat stronger.

5.1.3 Microseismicity

Bond breakages, and the associated release of strain energy, form seismic events (Hazzard et al, 2000). Specifically, the energy released during bond breakages, in the form of seismic waves, trigger further cracking by increasing local stresses, which exceed the strength of neighboring bonds. The coalescence of these micro-cracks constitutes a macro-rupture. The moment tensor corresponding to an event can be computed by analyzing the force changes at contacts around the source particles (Hazzard and Young, 2004). The moment tensor is then calculated at each time step over the duration of the event by assuming that a shear fracture propagates at half the shear wave velocity of the medium (i.e. from the time of breakage to twice the time for a shear wave to propagate to the edge of the source area). If a new crack forms within the source surface of an active crack, the two cracks are considered part of the same seismic event. The source area S is expanded to enclose all source particles and the time is reset to zero. This algorithm requires the use of dynamic damping in which damping of the system is reduced when cracking occurs. It is important to note that this causes a relative increase of kinetic energy in the system which may disrupt bonds close to failure. In fact, a sample has been documented to have a $\sim 15\%$ reduction in peak strength with the introduction of dynamic damping (Hazzard et al., 2000). Consequently this failure tends to be more abrupt yielding stress-strain curves with jagged peaks.

5.1.4 Mechanical Observations

Using a calibrated sandstone model, several tests are performed. The first set of simulations are conducted on the intact calibrated sample. Stress-strain

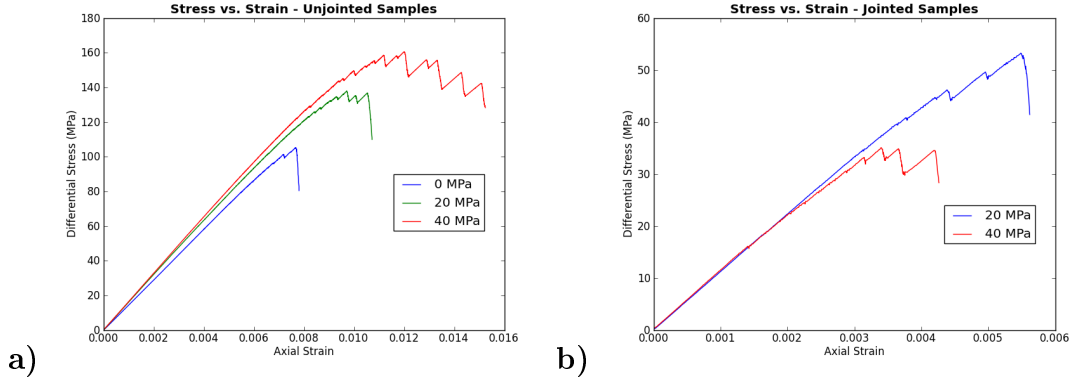


Figure 5.2: Differential stress strain curves for a) homogenous samples and b) samples with circular smooth joint inserted.

curves at 0 MPa, 20 MPa, and 40 MPa confining pressures are obtained, see Figure 5.2a. The simulations are run until 80% of the absolute peak stress is achieved (post peak stress). As expected, an increase in confining pressure increases both crack initiation and peak stress of the sandstone. In the unconfined triaxial test, the failure is likely a result of tensile failure and the bond breakages in the sample are uniform throughout the sample. For the failure of the samples under confinement, shear fracture is readily observed as the bond breakages localize along distinct planes.

The next set of tests are conducted using the same calibrated sandstone model with the introduction of smooth joints. A circular joint is placed at 27 degrees from the vertical axis with a radius of 6mm, see Fig. 5.3. The coefficient of friction of the joint is set at 0.2. Triaxial tests are conducted at confining pressures of 20 and 40 MPa (Figure 5.2b for the corresponding stress strain curves). Comparing the jointed and non-jointed samples at 20 MPa confinement, the peak differential stress is reduced from 137.8 to 53.2 MPa. In general, the strength of the sample is dramatically reduced by the introduction of the joint. New cracks are mainly located at the edges of the joints as propagation of the plane of weakness becomes the primary mechanism for fracture devel-

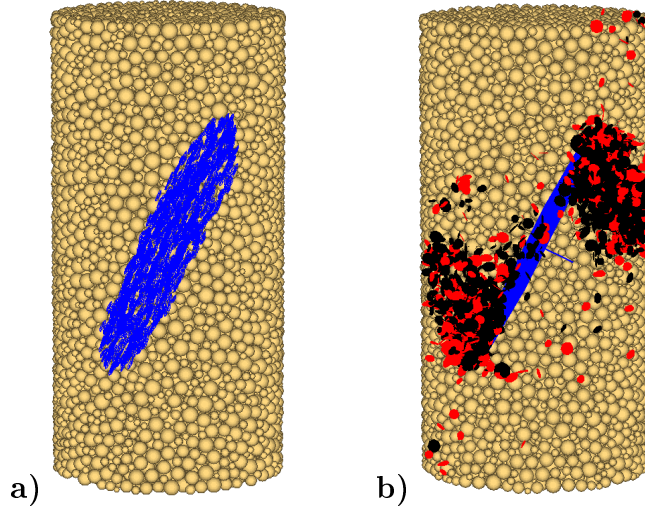


Figure 5.3: The calibrated sandstone sample with circular smooth joint inserted. The joint is 27 degrees off the vertical axis and has a radius of 6mm. a) Sample before simulations. b) 40 MPa sample after triaxial test (normal bond breakages in red and shear bond breakages in black).

opment, see Fig. 5.3b. Further analysis shows that increasing the confining pressure substantially decreases the differential peak strength of the jointed sample (see Fig. 5.2b). This appears counterintuitive as it is expected that the sample will be strengthened with increased confining stress. However, in the present case, the size of the asperity is large in relation to the size of the sample. The edges of the crack are close to the radial boundary. This induces a significant near-stress field in the proximity of the crack tips contrary to far-stress fields usually considered in rock mechanics (Jaeger et al., 2001). In the axial direction the source of the stress field is further out from the joint. The result is that the sample is weakened despite the increase in confining stress. We have found that simulations with smaller joint lengths (relative to specimen size) reproduce the familiar increase in peak strength with increasing confinement pressure, see Table 5.3.

The energy released by the failure of bonds in the samples can be computed from the spikes in kinetic energy following bond breakages. The kinetic energy

Table 5.3: Absolute peak stress of the samples. Sample radius is 5mm. Table lengths are radii of the circular joints.

Confinement Pressure	No Joint	Joint-6mm	Joint-4mm	Joint-3mm	Joint-2mm
20 MPa	157.8 MPa	73.75 MPa	129.8 MPa	145.7 MPa	154.7 MPa
40 MPa	200.5 MPa	75.3 MPa	149.3 MPa	171.1 MPa	192.2 MPa

of the sample is computed by measuring the instantaneous velocities (both translational and rotational) of all particles in the system, both before and after bond breakages. The kinetic energy before failure is subtracted from the maximum of the kinetic energy spike following a breakage, and the total kinetic energy emitted is then estimated from the sum over all bond breakages.

Routines are also available to calculate the boundary work at any given time, which gives the total input energy of the system. Measuring the ratio of the bond failure kinetic energy and the system input energy gives an estimated percentage for the brittle failure of the simulation (see Table 5.4). For the sample with 0 MPa confinement, the kinetic energy from brittle failure is about 9% of the input energy. A key observation is that brittle failure is reduced approximately by half in the presence of confining pressure. This result is supported by laboratory experiments that show a higher mean stress will cause failure to be more ductile than brittle. With the introduction of joints the change in brittle energy content is not significant. This may be a symptom of the timescale of the simulations, which are run until 80% peak failure is met. Instead, it may be more suitable to have the simulation end when a fixed axial strain is met or to hold the energy input of the system constant across all simulations.

Table 5.4: Energy content at the end of simulations.

Experiment	Kinetic Energy from Bond Breakages (J)	Boundary Work (J)	Brittle Failure Percentage
0 MPa - No joint	0.0698	0.7095	9.84 %
20 MPa - No joint	0.0761	1.7287	4.40%
40 MPa - No joint	0.1745	3.4986	4.99%
20 MPa - Jointed	0.0194	0.4449	4.36%
40 MPa - Jointed	0.0225	0.4156	5.41%

5.1.5 Microseismicity Analysis

The number of microseismic events in each simulation follows an exponential curve as the applied stress increases. This behavior is similar to real laboratory experiments (Jouniaux et al., 2001). A comparison of the total number of events for samples without a joint (Table 5.5) shows that a higher confinement leads to more failure. For simulations with the joint, the plane of weakness accommodates the deformation and thus reduces the peak strength of the specimen. The number of events is drastically reduced. By construction, the joint will also decrease the number of bond breakages as particles neighbouring the joint are unbonded. These results are consistent with laboratory experiments performed by Jouniaux et al. (2001).

The analysis of the micro-cracks shows that more than two thirds of the events are single bond breakages (cf Table 5.5). A single bond event has an average magnitude of -7.7 although the magnitude can range between -9 to -7 depending on the force variations. The radiated energy calculation, E_s , is based on the Gutenberg-Richter relationship between the moment magnitude M_w and the energy (Kanamori, 1977):

Table 5.5: Microseismicity analysis.

Samples	Number of events	% of single - bond event	Radiated energy (J)	% radiated energy / boundary work	b-value	D-value
0 MPa no joint	1723	73	0.000785	0.1	2.35 ± 0.2	2.73 ± 0.11
20 MPa no joint	2868	66	0.001433	0.08	2.25 ± 0.08	2.79 ± 0.08
40 MPa no joint	4276	65	0.002699	0.08	2.14 ± 0.09	2.80 ± 0.09
20 MPa jointed	600	71	0.000282	0.06	2.33 ± 0.13	1.67 ± 0.09
40 MPa jointed	610	73	0.000399	0.08	1.59 ± 0.09	1.54 ± 0.12

$$E_s = 10^{(11.8+1.5*M_w)} \quad (5.1)$$

The ratio between the radiated energy and the boundary work is below 0.1%. E_s is also compared with the measured kinetic energy after the bond breakages in the sample. The discrepancy between the two is more than two orders of magnitude. However, it should be noted that the Gutenberg-Richter formula was developed for earthquakes with a magnitude higher than 5 and should certainly be modified for smaller-scale types of events. Additionally, this empirical relationship assumes a double-couple type of mechanism whereas most of the events in our simulation show tensile behavior (Figure 5.5).

A sparse distribution of events is displayed in Figure 5.4 for the unconfined experiment at the three different stages. A macro fracture plane appears after the peak stress has been reached for the non-jointed sample at 40MPa confinement. For the jointed samples, the plane of weakness causes the events to localize near the smooth joint very early on in the simulations. Differences in event location distributions are quantified through the fractal dimension D, which measures the clustering of events (Grassberger and Procaccia, 1984). A D value close to 3 signifies a uniformly distributed cloud of events whereas a D value below 2 is found for events located over a planar structure. A D value

above 2.7 is found over all events for all simulations without the joint (cf Table 5.5). This is in agreement with the visual spread of the events observed. A D value around or below 2 is found for the jointed experiments at confining pressures 20 and 40 MPa. This suggests that events localize along planar structures in the sample.

Another important statistical value is the exponent of the power law distribution of the event magnitudes first described by Gutenberg and Richter (1944), denoted by b . A low b -value implies more large events whereas a high b -value means more small events. In our simulations the lowest b -values are found for the 40 MPa confined experiments, which is consistent with Amitrano (2003) who show b -values depend inversely on stress (Amitrano, 2003). More recently, b -values over 2 have been found to be directly related to tensile fracture mechanisms (Maxwell et al., 2008). The b -values computed for all simulations are rather high, typically above 2. The source mechanisms for events are represented on a Hudson plot (Hudson et al., 1989) in Figure 5.5. They predominantly range from opening to closing types of events, so tensile failure seems to be indeed correlated with very high b -values. A few events are at the center of the Hudson plot, which indicates a strike-slip type of mechanism. No difference in terms of source mechanism can be found between the different stages of the experiment. Longer simulations are expected to expose a complete localization of the events along a macro fracture plane. In this case, sliding will occur (Jouniaux et al., 2001), leading to more strike-slip type of mechanisms.

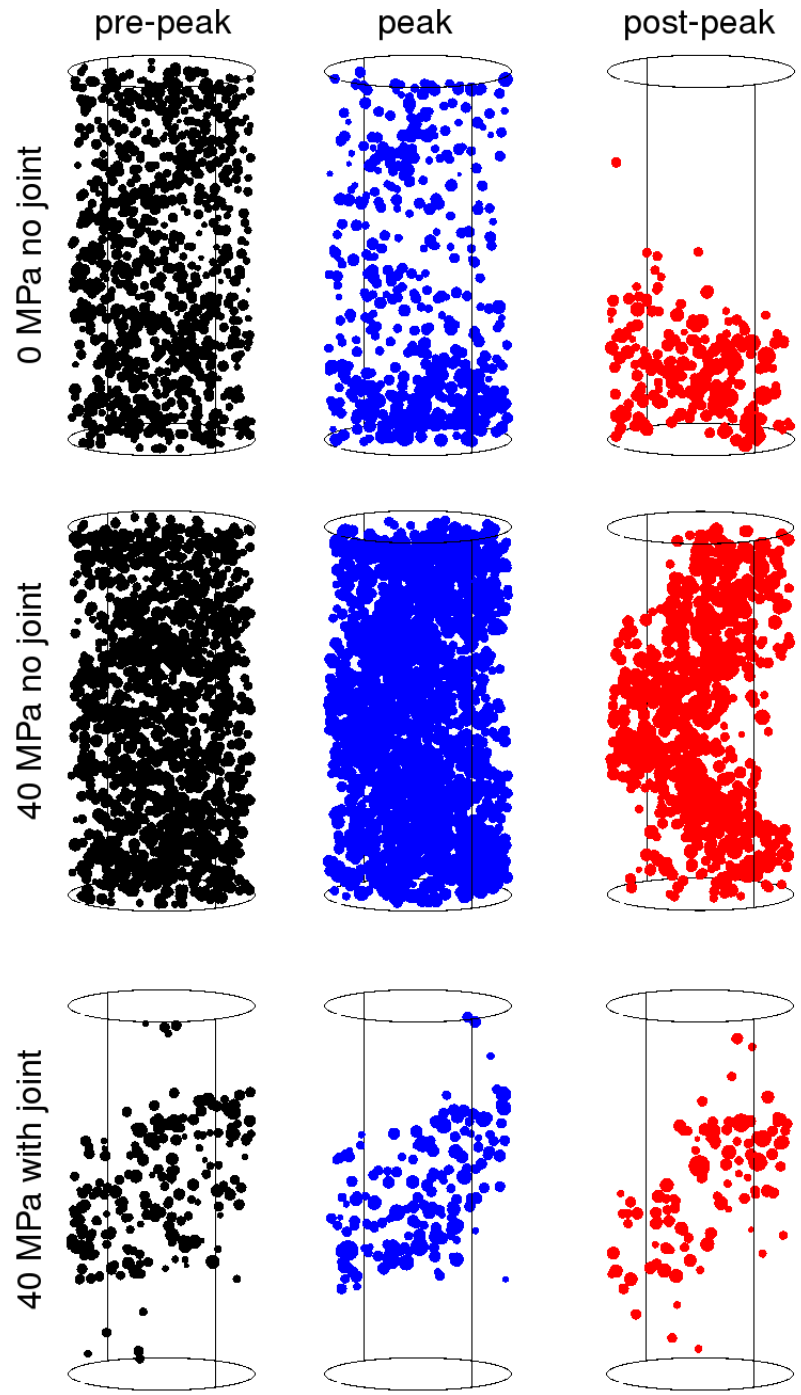


Figure 5.4: Images of the event locations at different stages for three different simulations.

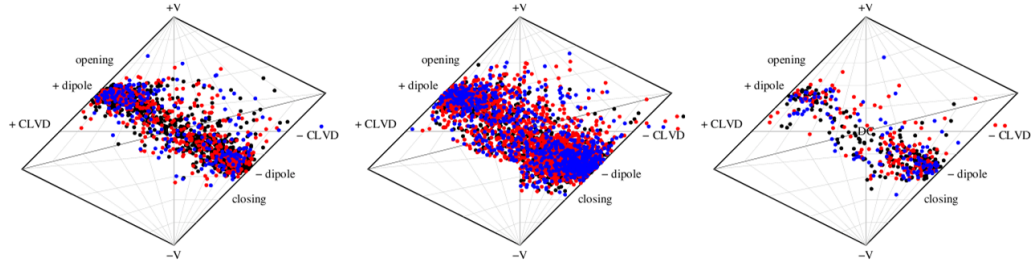


Figure 5.5: Source mechanisms of events for the simulations shown in Figure 5.4 represented on a Hudson plot. The colors define the different stages during the experiments according to Figure 5.4. 0 MPa no joint (left), 40 MPa no joint (middle) and 40 MPa with smooth joint (right).

5.1.6 Discussion

In this article we simulate acoustic emissions and geomechanical deformation in a simple triaxial compression test to demonstrate the capabilities of bonded-particle methods. Obviously the actual geomechanical behavior inside and surrounding a reservoir during hydraulic fracturing is significantly more complex; yet analysis of the energy balance already allows us to draw some conclusions on ratios between aseismic (ductile) versus seismic (brittle) deformations. Often substantial differences are estimated between the total input energy inferred from fluid injection rates and pressures, the fracture energy to pry apart the walls of a single very large fracture, and the radiated energy observed from recorded seismicity. The injected energy is $10^4 - 10^7$ times larger than the estimated radiated seismic energy, and the fracture energy is inferred to equal 15 – 40 % of the input energy (Maxwell et al., 2008; Boroumand and Eaton, 2012). These energy calculations incorporate several key factors and assumptions. The injected energy includes the work done to cause local rock failure and deformation but also fluid friction inside the well, rocks and any leak off. The fracture energy purely entails tensile opening of an existing crack but excludes the work required to create new fractures. Estimates of the amount of radiated seismic energy are based on empirical laws commonly used

in global seismology that assume double-couple source mechanisms and thus pure shear but no tensile deformation (failure). In geomechanical modeling the boundary work (input energy) equals the sum of exerted body forces (gravity), kinematic energy (bond breakages), frictional work, strain energy (ductile deformation) and internal damping. The kinematic energy includes thus both shear and tensile failure, and represents about 4 – 10 % of the total energy (Table 5.4). On the other hand, the estimates for the seismic radiated energy comprise only 0.08 – 0.10 % of the total energy (Table 5.5), and are thus 50 – 100 times smaller here than the actual amount of brittle failure (work). This implies that computations based on the amount of radiated energy inferred from seismic moment calculations may always significantly underestimate the percentage of incurred brittle failure, partially since the underlying empirical laws exclude tensile failure. Finally, when examining the radiated or kinetic energy from brittle failure, in either case, the energy is substantially lower than the input energy. It seems reasonable to conclude that ductile deformation must be a significant term in the energy budget for both the proceeding simulations and for hydraulic fracturing experiments in general.

5.1.7 Conclusion

An important question in the monitoring of a reservoir is what the exact link is between the recorded microseismicity and the actual geomechanics. Independent observations of event locations, source mechanisms and stresses are used to infer their relationship but often observations are not made at the same location (around wells for stresses, further away and deeper for microseismic events) or at the same scale. It is also possible aseismic deformation may take place, preventing the use of recorded microseismicity for deduction

of the geomechanical behavior in the reservoir. One possible way to define the interaction between rupture mechanisms and recorded events is by the use of modeling. In this article, we have used the bonded particle method to explore the rupture mechanisms of a sandstone model under differing confinement pressures both with and without a joint. We find the radiation energy to be about 50-100 times smaller than the kinetic energy from brittle failure. This suggests the possibility that radiated energy calculated by the Gutenberg-Richter relationship may underestimate the energy incurred from brittle failure. Whatever the case, energy from brittle failure is substantially lower than the input energy suggesting ductile deformation is a significant term in the energy budget. These preliminary experiments produce both interesting and quantifiable results suggesting the bonded particle method is a viable approach for modeling more complicated scenarios. Ultimately, it is both a real desire, and perhaps a possibility, to include the complexity of fluid injection in the hopes of better modeling hydraulic fracturing experiments.

5.2 Energy Budget Discrepancy between Rock Fracturing and Associated Microseismicity

Abstract

Many studies of hydraulic fracturing of oil and gas reservoirs have raised the issue of energy balance between the injected fluid volume and the recorded microseismicity. Indeed the injected energy is 10^4 - 10^7 times larger than the estimated radiated seismic energy. The computation of the different energy components are based on several assumptions, including the well-known em-

pirical energy-magnitude relation inferred for large magnitude earthquakes. To address this problem, we use a bonded-particle geomechanical modeling approach which allows us to compute each energy component independently. To test our model, we simulate triaxial compression on sandstone samples. Based on our independent computation of the radiated energy, we propose an updated empirical energy-magnitude relation. This relation should be more suitable for microseismic events with various rupture mechanisms including volumetric changes. However we still find a discrepancy between the radiated energy and the strain energy: the radiated energy only represents 2.5% of the input strain energy. Aseismic deformation processes are the best candidate to explain the difference.

5.2.1 Introduction

Earthquakes are the mechanism through which the potential (or strain) energy stored in a fault plane is released in the form of seismic waves, radiated energy, but is also lost through friction and surface energy as new fractures are created in the subsurface (Kanamori, 2001; Scholz, 2002). The seismic efficiency η is a measure of the partitioning of energy during an earthquake and is equal to the ratio of radiated energy over the change of strain energy due to the slip on the fault. For most earthquakes, this seismic efficiency is found to be less than 0.06 (McGarr, 1999) implying that most of the released strain energy cannot be recorded at the surface.. In general, η is strictly an estimate as it requires knowledge of the total stress changes at the fault but only the radiated energy can be determined from seismological observations directly (Kanamori and Rivera, 2006; Kanamori, 2001; Scholz, 2002).

Many studies of microseismicity in the context of hydraulic fracturing of oil

and gas reservoirs have attempted to assess the energy balance after injection (Boroumand and Eaton, 2012; Maxwell et al., 2008). These studies also show a discrepancy between the injected fluid volume (input energy) and the recorded microseismicity (radiated energy). Indeed the injected energy is around 105 times larger than the estimated radiated seismic energy, and the fracture energy is about 15-40% of the input energy (Boroumand and Eaton, 2012). The computation of the different energy components are based on several assumptions, including the well-known empirical radiated energy-magnitude relation (Kanamori, 1977) inferred for large magnitude events with a double-couple failure mechanism. Part of the underestimation of fracture energy is due to the smallest magnitude events not being recorded, but even after correction for missing events using the Gutenberg-Richter magnitude distribution, the discrepancy remains (Boroumand and Eaton, 2012).

Without direct access to the subsurface rock it is difficult to infer what geomechanical processes are responsible for the observed microseismicity and how the energy is actually dissipated. Geomechanical modeling is one technique that can provide some insight into the dissipation of energy in the reservoir. Bonded particle modeling provides a means to simulate both the geomechanical rock deformation and the related microseismicity (Hazzard et al., 2000; Potyondy and Cundall, 2004). It allows for the spontaneous development of cracks under applied stress. The source mechanisms of the cracks can then be investigated and linked to the overall deformation of the medium (Hazzard and Young, 2000).

In this article, to address the problem of energy balance, we use a bonded-particle geomechanical modeling approach, which allows us to compute each energy component independently (Chorney et al., 2012). To test our model,

we simulate triaxial compression conducted on a calibrated sandstone model. This choice of simulation is motivated by the fact that sandstone is a common porous rock (where hydrocarbons are found), and triaxial laboratory experiments are well-documented providing a means of comparison of our results. The outline of the remainder of this article is as follows. The second section of this paper is devoted to the description of the model and the explanation of the relevant simulation parameters. Section three presents the simulation results and associated microseismicity calculations. In section four we discuss our results and make a comparison of our modeling with larger scale examples.

5.2.2 Modeling

Bonded Particle Model

The discrete element method (DEM) is a class of finite element methods whereby a material system is represented by independent discrete elements, typically of micrometer to millimeter size (Cundall 1971). It has become a powerful tool for simulating the mechanics of rock materials. The essential idea of the method is that each element interacts with adjacent elements by specifying contact interactions. Rotational degrees of freedom are also allowed so that interacting elements can impart not only normal and shear forces, but also moments. By creating an assembly of many such interacting, and in general non-identical elements, it is possible to simulate rock mechanics for a wide range of heterogeneous materials. However, the fact that each particle does not necessarily represent an actual particle (or grain) in the system means that the use of DEM should be accompanied by a model calibration process whereby the micro-parameters specified for the model are chosen such that

they lead to desired macro-parameters (eg. Young's modulus and unconfined compressive strength) for the material.

A bonded particle model (BPM; Potyondy and Cundall, 2004) is a specific implementation of DEM that simulates rock deformation using an assembly of rigid, round particles that are bonded together using the parallel bond logic. (The canonical BPM implementation uses disks (in two-dimensions) or spheres (in three-dimensions) as the basic element referred to as “balls” or “particles”.) This assembly of particles can deform freely and bonds can be broken to represent local failure. Such a discrete approach is more appropriate to model rock deformation through failure since it eliminates the need for complex constitutive relations required for continuum approaches (Hazzard et al., 2000). In addition, microseismic events can be inferred by integrating local bond failure in both space and time (Hazzard and Young, 2004).

BPMs are therefore a highly flexible implementation of DEM that can be used - in principle- to model a wide range of geomechanical structures and processes, including for example: compression and fracture tests (rock modeling), bulk flow, mixing, rock cutting, excavation and hydraulic fracturing. To investigate the utility of BPM methods, in this article, we report on simulations of fracture formation and propagation during triaxial compression tests on sandstone. We have employed the Particle Flow Code 3D (PFC3D) software package (Itasca Consulting Group, 1999), which implements the BPM. We describe the formulation of the model below, including the crucial step of model calibration, required for comparison to experiments with real rock samples.

Material Genesis

A BPM is formulated by generating a set of particles inside a finite domain and specifying the contact properties for inter-particle bonds. Typically, the particle and contact properties are sampled from a multivariate distribution so that a heterogeneous (irregular) assembly may be simulated. In three-dimensional models the finite domain is formed by the union of two-dimensional surfaces (i.e. walls) that form a closed region in space. Moreover, these surfaces can be either fixed (for static situations) or moving (under dynamic loading). The choice of boundary conditions is naturally problem-dependent, but with some combination of the above mechanisms it is usually possible to model many geomechanical problems of interest.

The BPM consists of specifying a set of intrinsic ball properties, which includes density ρ , average radius R and friction μ . Given these parameters, it is possible to determine the porosity of the sample as $n = 1 - V_p/V$ where V is the volume of the sample and V_p is the total volume of the particles (indexed by i) given simply by $V = \sum_i \frac{4}{3}\pi R_i^3$ for the case of spherical particles.

To construct the BPM, one must additionally specify the bond properties. Bonds represent the addition of a cementitious material between two adjacent particles. This “cement” allows both forces and moments to be transmitted over a finite area, and therefore allow a realistic model of many rigid materials. The bond can be envisioned as elastic springs (transmitting Hooke’s law type forces) spread uniformly across a circular area centered at the contact point perpendicular to the contact plane. Parallel bonds are specified by the normal and shear stiffness (k_{pbn} and k_{pbs} respectively), the normal (tensile) and shear strength (ω_c and τ_c respectively) and an additional parameter, the bond radius R_{pb} . Because the parallel bond acts over a finite area (determined by the

bond radius), the parameters ω_c and τ_c are expressed as the maximum normal or shear stress before the parallel bond breaks. In short, the parallel bond implement forces and moments that act as resistance for the two particles to both translate and rotate away from each other in both the normal and shear directions on the contact plane.

After specifying the particle and bond properties, as well as any external loading (as in the case of compression tests), the dynamical evolution of the sample is calculated using the simultaneous application of a Force-displacement relation and Newton's second law (Potyondy and Cundall, 2004). For rock mechanics tests, the usual procedure for material genesis is given by the following steps:

1. Compact Initial Assembly. Create assembly within cylindrical walled domain with desired porosity.
2. Install specified isotropic stress
3. Reduce number of 'floating' particles. This removes particles that have less than three bonds, thus ensuring a denser bond network.
4. Install parallel bonds

Compression Tests

Following the materials genesis procedure triaxial compression tests are implemented as follows. The top and bottom platens (walls) are accelerated to a final velocity, representing the axial compression while a specified stress field is maintained on the lateral walls. During the simulation the (engineering)

axial stress and strain are monitored. From these variables the Young's modulus (slope of stress-strain curve) and rock strength (deviation from elastic behavior) of the sample may be inferred.

At sufficient compressive load, fracturing may occur due to the propagation of micro-cracks (ie. broken bonds) in the system. If the tensile or shear stress exceeds the maximum tensile or shear strength of the parallel bond, a breakage will occur. The fracture angle is related to the rock strength and stress tensor.

Moment Tensor Algorithm

The bond breakages leave unbalanced forces on all particles neighboring the source breakage. By monitoring changes in forces, it is possible to model source mechanisms for the failure. Hazzard and Young (2004) created an algorithm that extracts the moment tensors for such failure.

When a bond breakage occurs in the BPM, the broken parallel bond is considered a single crack occurring between two particles. The moment tensor for a single breakage is calculated by measuring the changes in contact forces at all contacts surrounding the two particles for the duration of the event. The duration of the event is half the speed of the shear wave velocity over a distance of the average diameter of the particles in the sample. At each time step the change in forces at the contacts are measured against the initial contacts just before the bond breakage. Then for single bond breakages the moment tensor is calculated by summing up all moments to the surrounding contacts (Hazzard and Young, 2004).

For a single crack, the source location is at the center between the two particles involved in the breakage. A bond breakage that occurs between any

two random particles is about the same magnitude as the average size of the particles is about the same throughout the sample (The net forces following the breakages are similar as the masses are similar). In order to model a broad range of magnitudes of events, a rupture must be defined. A rupture is defined as a larger event that includes multiple cracks. The rupture occurs when there are multiple cracks that occur within close proximity of the initial crack. Specifically, a new crack must share one of its particles with a crack already within the rupture and must have occurred within the duration of the event. Thus a rupture is a coalescence of many bond breakages. The larger magnitude event is complete when no new crack occurs within proximity of the existing cracks. The moment tensor is again calculated by summing over all contacts surrounding all particles involved in all of the bond breakage pairs within the rupture. The event location is now the geometric centroid of the cracks.

Damping

As a bonded particle model essentially behave as a large system of springs, a damping parameter is needed to reduce unrealistic kinetic energy in the system. In order to dissipate the kinetic energy a damping parameter is introduced. The damping creates a fictitious force that opposes the net unbalanced forces, on the particles in the model. The magnitude of this force is given by,

$$F_D = -\alpha|F_{net}|sign(V) \quad (5.2)$$

where α is the user-defined damping parameter, F_{net} is the net force on the particle, and V is the velocity. Assuming a single mass spring system subject to only F_D , a quality factor Q is derived where,

$$Q = \frac{\pi}{2\alpha} \quad (5.3)$$

(Itasca Consulting Group, 1999). This equation provides an estimate for the damping parameter needed to match the wave attenuation parameter Q of a rock. However, the estimate does not include energy lost to friction. When monitoring and analyzing changes in kinetic energy within the system, the damping does indeed have a significant effect on the measured energy release from bond breakages throughout the system. Such a Q factor is not realistic at low damping where the force of friction greatly outweighs the damping force. Throughout the paper the user-defined damping parameter α will be used.

Parameter Calibrations

In order to align the simulated synthetic rock mass with the behavior of a real material (and therefore to have some confidence in the interpretation of the simulations) one must undertake a model calibration process. Here the micro-parameters of the DEM simulation (ie. particle and bond properties) are “tuned” until the desired behavior of the assembly is attained, as determined through the calculation of macro-parameters and their comparison with known properties of materials found in laboratory tests. For example, if simulating a compression test, one can calculate the stress-strain curve for the material and hence derive the Young’s modulus and rock strength, which can be compared to known values for an equivalent compression test in the laboratory.

It is worth adding a note of caution in the application of BPMs to model heterogeneous materials. One must perform convergence tests with respect to particle number and size. Even so, the BPM behavior may differ from a real rock sample for a number of reasons. For example, the use of spherical

particles can lead to spurious dynamics that may be avoided by utilizing a more complex elementary particle shape.

5.2.3 Simulations

Samples

For the following simulations a triaxial sleeve is created of height 2cm and radius 0.5cm. Initially, the samples are calibrated to match that of a sandstone from the Piceance basin with unconfined compressive strength (UCS) 175.6MPa, $E=39.6$ GPa, and $\nu=0.26$ (Senseny 1983). Five random packings of the spheres are created with identical microparameters on which unconfined compression tests are conducted. The seeds for the random number generator for the packing of the spheres are the only attributes varied for the five samples. These samples, S7, S8, S9, S11 and S12 are created using seed's 7, 8, 9, 11 and 12, respectively, for the random number generator. For the initial calibration, the damping parameter, α , is left at the default value of 0.7. The values for the average UCS, E , and ν are, 178 ± 4 MPa, 38.8 ± 0.4 GPa, 0.26 ± 0.01 , respectively. For individual values see Table 5.6. In order to model the dynamic behavior of the samples and to appropriately analyze changes in kinetic energies of the system, the damping parameter must be appropriately set. For the following simulations, the damping parameters are updated from a value of $\alpha=0.7$ to $\alpha=0.05236$. This lower damping parameter is selected to encourage more dynamics in the system. The low damping will produce larger magnitude events and less attenuation of seismicity promoting a more realistic distribution of microseismic events (Hazzard et al., 2000).

With a higher quality factor of the rock, uniaxial testing produces updated

Table 5.6: Mechanical properties of the simulated samples. E is the Young’s modulus; ν is the Poisson’s ratio; and UCS is the unconfined compressive strength

Sample	E (GPa)	ν	UCS (MPa)
S7	39.0	0.27	180.0
S8	38.6	0.26	178.7
S9	39.0	0.26	172.0
S11	38.3	0.25	183.8
S12	39.2	0.25	176.1

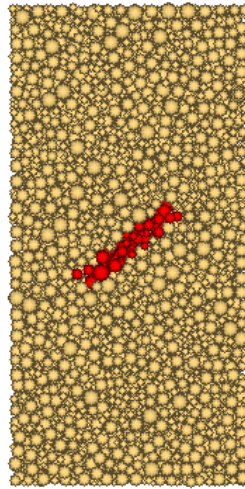


Figure 5.6: Example of a sample with plane weakness colored in red.

values of the UCS, E , and ν which are 162 ± 6 MPa, 39.1 ± 0.3 GPa, and 0.26 ± 0.01 , respectively. The average value of the Young’s modulus and Poisson’s ratio remain about the same, but the compressive strength of the samples drop by about 9 %. It is important to note that the lower damping parameter results in greater kinetic energy within the system. This in turn disrupts bonds closer to failure. A low Q factor (high damping) implies numerous single-bond breakages, in general about 75% of the total number of events, whereas low damping simulations allow for larger building events with approximately 65% of single-bond events.

Simulations

Triaxial tests with a confining pressure of 20 MPa are applied to the calibrated samples S7 to S12. The triaxial tests are run until the axial strain is larger than 1%, in which case full nucleation of the shear fractures develop as the sample fails in a brittle fashion. In addition, tests are performed on samples with a region of unbonded particles enclosed inside. In Figure 5.6 the particles highlighted in red are unbonded. Such a region should be imagined as an imperfection in the rock that could act to further localize the fracturing of the sample. These five samples are S7w, S8w, S9w, S11w, and S12w which are weakened samples created using seeds 7, 8, 9, 11 and 12. For the duration of the simulation, bond breakages are monitored, moment tensors are calculated, and the kinetic energy following the bond breakages is extracted.

The stress strain curves for the simulation conducted on the homogenous samples are shown in Figure 5.7. Very clearly the elastic regime can be observed. Eventually, as individual bonds start to break, permanent damage of the microstructure of the sample is occurring as the deformation becomes more ductile. The load reaches the peak stress of the sample and brittle failure occurs (cf Table 5.7).

The stress strain curves for the simulations conducted on the weakened samples are shown in Figure 5.7. The curves look very similar with the peak compressive strength of the samples about 8% lower, although the weakness of the sample causes a more distinct localization of the bond breakages along a shear fracture plane (see Figure 5.9b). Finally, two additional tests are conducted on samples where the damping of the system is very low and very high. The low damping, $\alpha=0.00785$, and high damping, 0.7854, are conducted on a sample with the default seed to the random number generator of 10,000, which

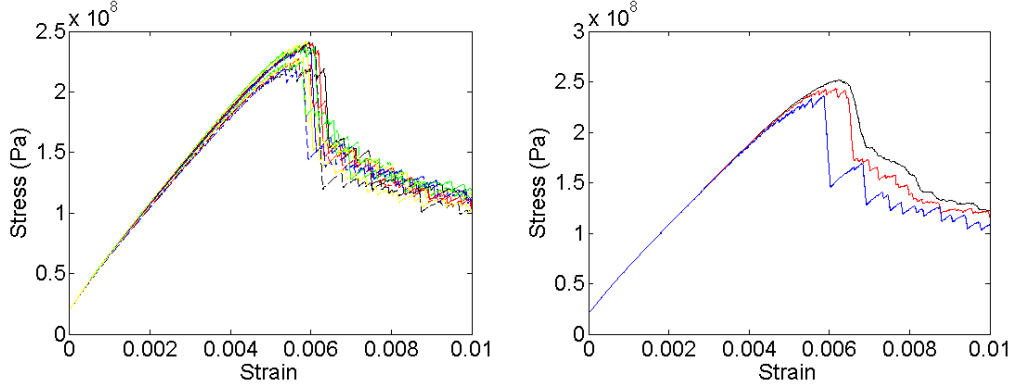


Figure 5.7: (Left) Stress-strain curves for 10 simulations, 5 with intact samples (solid lines) and 5 with a weakness (dashed lines). Colors are referring to the seed number used for the simulations: seed 7 in black, seed 8 in red, seed 9 in blue, seed 11 in green and seed 12 in yellow. (Right) Stress-strain curves for 3 simulations with different damping factors: $Q=2$ in black, $Q=10$ in red and $Q=200$ in blue.

are samples Q200 and Q2, respectively. The confinement of the simulations is again maintained at 20 MPa. The two samples are tested to investigate the range of emitted kinetic energy. Their stress strain curves are in Figure 5.7.

Energy Calculations

In earthquake seismology the radiated energy is defined as the change in kinetic energy from the beginning to the end of the rupture of the earthquake along a fault,

$$E_R = \Delta E_K = -\Delta E_P - \Delta E_F - \Delta E_S, \quad (5.4)$$

where ΔE_P is the strain energy, ΔE_F is the frictional work, and ΔE_S is the surface energy (Scholz, 2002). A microseismic event within the BPM is complicated in that it may be a coalescence of many bond breakages. There certainly is some ambiguity as to the specific termination of the rupture. It is reasonable to assume the rupture ends when the maximum kinetic energy is

Table 5.7: Energy results and peak stress values for all simulations. E_K is the radiated energy computed from the change in kinetic energy during an event. E_R is the radiated energy computed from the event magnitudes using Kanamori’s formula (1977).

Sample	Peak Stress (MPa)	Boundary Work (J)	Frictional Work (J)	Total Kinetic Energy (J)	E_K (J)	E_R (J)
S7	241.5	2.2591	0.7119	0.14479	0.059663	0.0043516
S8	240.3	2.2263	0.70285	0.194055	0.056422	0.0041678
S9	236.4	2.2070	0.70291	0.16934	0.058532	0.0041024
S11	238.1	2.2574	0.66644	0.1347	0.058392	0.004108
S12	241.7	2.2339	0.67015	0.13863	0.056755	0.0041806
S7w	222.8	2.0852	0.6379	0.14476	0.050771	0.0035786
S8w	227.2	2.1539	0.66352	0.11528	0.053014	0.004007
S9w	219.5	2.1170	0.6412	0.12254	0.047668	0.0037341
S11w	225.4	2.2041	0.6535	0.11035	0.055054	0.0040287
S12w	228.4	2.0952	0.63296	0.118338	0.052338	0.0036845

reached following a microseismic event.

In order to obtain an energy budget for the simulations, the radiated energy release from the microseismicity is estimated by directly monitoring kinetic energy following bond breakages. The total kinetic energy in the system at any given time is calculated from the translational motion and angular velocity of all particles in the sample. Two algorithms run simultaneously. The first algorithm monitors the total change in kinetic energy of the entire sample following individual bond breakages. The energy released by the failure of bonds in the samples is estimated by subtracting the maximum of the instantaneous kinetic energy post bond breakage from the instantaneous kinetic energy in the system prior to the breakage (Chorney et al., 2012). This kinetic energy is summed over all bond breakages to provide an estimate of the total radiated energy.

The second routine only monitors the kinetic energy of particles within measurement spheres surrounding the bond breakage events. The radius of the

measurement sphere is the P-wave velocity multiplied by the time it takes for a single bond breakage event to complete. The measurement sphere will capture most of the kinetic energy for single bond breakage events and for large ruptures the measurement sphere increases linearly as a function of the total number of cracks in the acoustic emission. As the measurement spheres grows events that are close together in space and time may constitute separate events so that two separate measurement spheres overlap and double count the kinetic energy. A limit to the size of the measurement spheres is in place so as not to get too large in order to avoid double counting. The measurement sphere is placed at the geometrical centroid of the event. As more and more bond breakages occur, the event centroid migrates with the center of the growing rupture. It is possible that as the measurement sphere moves, kinetic energy is missed. Following large magnitude events the kinetic energy in the measurement spheres drops dramatically as energy is lost to damping and friction. If a small event occurs in space and time with such a measurement sphere (but is not a member of the large rupture) it is possible that the change in kinetic energy before and during the small event is negative. These events are small and the kinetic energy is set to zero by default. About 7% of the events are these zero type of events, but 65% of these events are single bond breakages. The magnitude of these events are negligible in the overall energy budget. These algorithms continuously monitoring the kinetic energy of the system provide a direct estimate of the radiated energy without estimating the values on the right side of equation (5.4). Whereas in the context of earthquake seismology, the radiated energy is calculated by estimating the terms on the right of equation (5.4). The power of the bonded particle model is in its ability to allow direct computation of the kinetic energies of the system.

For the simulations the radiated energy is also calculated from the estimated

moment tensors using the formula from Kanamori (1977),

$$E_R = 10^{11.8+1.5 \times M_w}. \quad (5.5)$$

Finally, boundary conditions (forces) applied to particles within the BPM provides a net input of energy into the system. The boundary work is calculated by first summing up all contact forces between each wall and the particles in contact with it. The work conducted by a single wall is then just this resultant force multiplied by the displacement of the wall over one time-step. The work is then summed up over all walls in the system, and then summed over all time-steps. The frictional work can also be tracked and is obtained by multiplying the force of friction, F_n , with the slip distances at all contacts in the system then summed over all time-steps. Unfortunately, energy lost to the damping of the system is not monitored. For the simulations the input energy or boundary work into the system is monitored along with the total amount of energy lost to frictional work.

Statistics of Events

Gutenberg and Richter (1944) defined the power law distribution of earthquake magnitudes as $\log N(m > M) = a - bM$ where N is the number of events with a magnitude m superior to a certain magnitude M . The value b is the coefficient of the power law and represents the slope of the curve in a semilog plot of N versus M . The parameter a defines the background seismicity. The b -value can simply be computed by fitting the graphical curve $\log N$ versus M in a least-square sense. A high b -value means numerous low magnitude events are happening whereas a low b -value is found when large magnitude events are

occurring. Changes in the b -value can be used as a proxy for stress changes in the medium (Grob and van der Baan, 2011; Schorlemmer et al., 2005).

5.2.4 Results

Radiated Energy

For the samples S7-S12 and S7w-S12w the total radiated energy from the moment tensors and the total radiated energies from the measurement spheres are in Table 5.7. These two values differ by an order of magnitude. The radiated energy E_R computed from Kanamori's relation accounts for about 0.2% of the total input energy. The radiated energy E_K inferred from change in kinetic energy however reaches 2.5% of the total input energy. E_K is a direct measurement of the energy linked to seismic wave propagation so the difference in the ratios suggest that Kanamori's relation is underestimating the actual radiated energy. The frictional energy of both the weakened and homogeneous samples are recorded in Table 5.7. The percentage of energy lost to friction over the simulations is the same for all samples at about 30%. The ratio of the kinetic energy release over the boundary work for triaxial simulations on samples Q200 and Q2.2 is 0.7% and 7.3%, respectively.

Microseismic efficiency is the fraction of total input energy which is radiated as seismic waves and is often assessed during monitoring of hydraulic fracturing (Boroumand and Eaton, 2012). This ratio is usually much less than 1% (most of the time around 0.1%). The main explanation for such a low percentage is that low magnitude events may not be recorded and that the attenuation factor of the rock could be grossly underestimated. Even after correction by extending the Gutenberg-Richter law to the smallest magnitudes, the micro-

seismic efficiency remains around 0.1% (Boroumand and Eaton, 2012). For our simulations, as the particles are monitored directly, all events are recorded without exception, and still the ratio between the input energy (boundary work) and the radiated energy only reaches 0.2% when the radiated energy is computed with Kanamori's (1977) relation between magnitude and radiated energy (Chorney et al., 2012). The radiated energy computed by directly monitoring kinetic energy of the particles increases the microseismic efficiency to around 2.5% (see Table 5.7). There is about a factor 10 between the two methods of radiation energy calculation.

Microseismicity

The number of events grows exponentially throughout the simulations (Figure 5.8), as is observed in real triaxial laboratory experiments (e.g. Lockner et al., 1991; Jouniaux et al., 2001; Lei et al., 2004), even for the weakened samples. The crack activity accelerates at the end of the linear elastic phase at roughly 0.0035 s and the number of events increases drastically from this point forward. This behavior is consistent in all our simulations and is similar to real laboratory experiments (Jouniaux et al., 2001; Lei et al., 2004). The dynamic damping factor α influences the total number of events but not the onset of crack activity increase (cf Figure 5.8). Figure 5.9 shows the locations of events at different time intervals (chosen to contain the same number of events) during one simulation. During the first steps events are spread all over the sample. At around six seconds they cluster along a single curved plane. This behavior is strongly similar to the results shown by Lockner et al. (1992, figures 10 and 11) for laboratory triaxial experiments on Berea sandstone. The clustering of events happens at the peak stress (cf Figure 5.8) and remains until the end

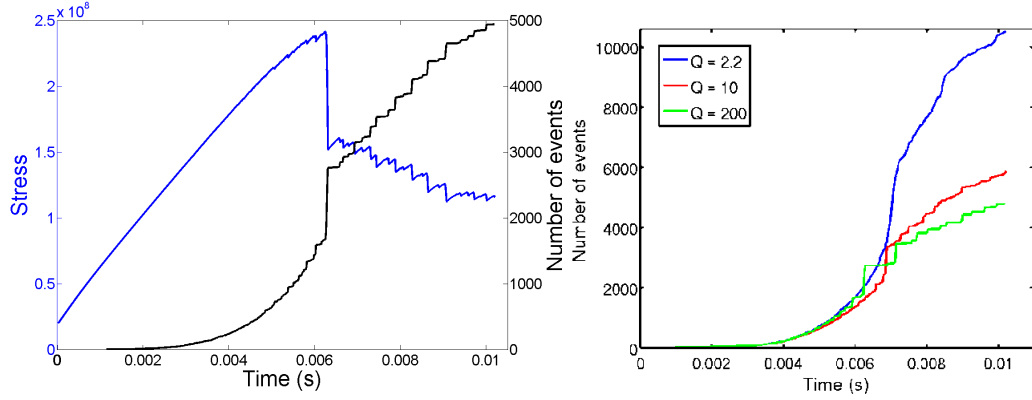


Figure 5.8: (Left) Stress (blue) and cumulative number of events (black) versus time for one simulation. (Right) Number of events versus time for three simulations with varying Q factor: 2.2 in blue, 10 in red and 200 in green.

of the experiment, which is the expected behavior for triaxial experiments on sandstone (Lockner et al., 1992). This evolution is consistent throughout our simulations. When the weaknesses are included in the samples, events tend to cluster earlier and develop into a single macro rupture plane whose orientation follows the inserted joint. The weaknesses certainly encourage localization of the fractures.

The event magnitude distribution follows the Gutenberg-Richter power law (cf Figure 5.10; Gutenberg and Richter, 1944) and is consistent over all simulations. The distribution departs from linearity around -7.4 for small magnitudes and above -6.3 for large magnitudes for all simulations, except Q_2 . The lower limit of the power law is due to the numerous single-bond events which have an average magnitude of -7.7 (Chorney et al., 2012), the variations being due to the different force changes taken into account for each event. The departure from linearity for large magnitudes depends on the rarity of big events in our finite size samples used for the simulations. All b -values are therefore computed in the range of magnitudes between -7.4 and -6.3 . Simulation Q_2 contains 75% of single-bond events, which could explain the dissimilar magni-

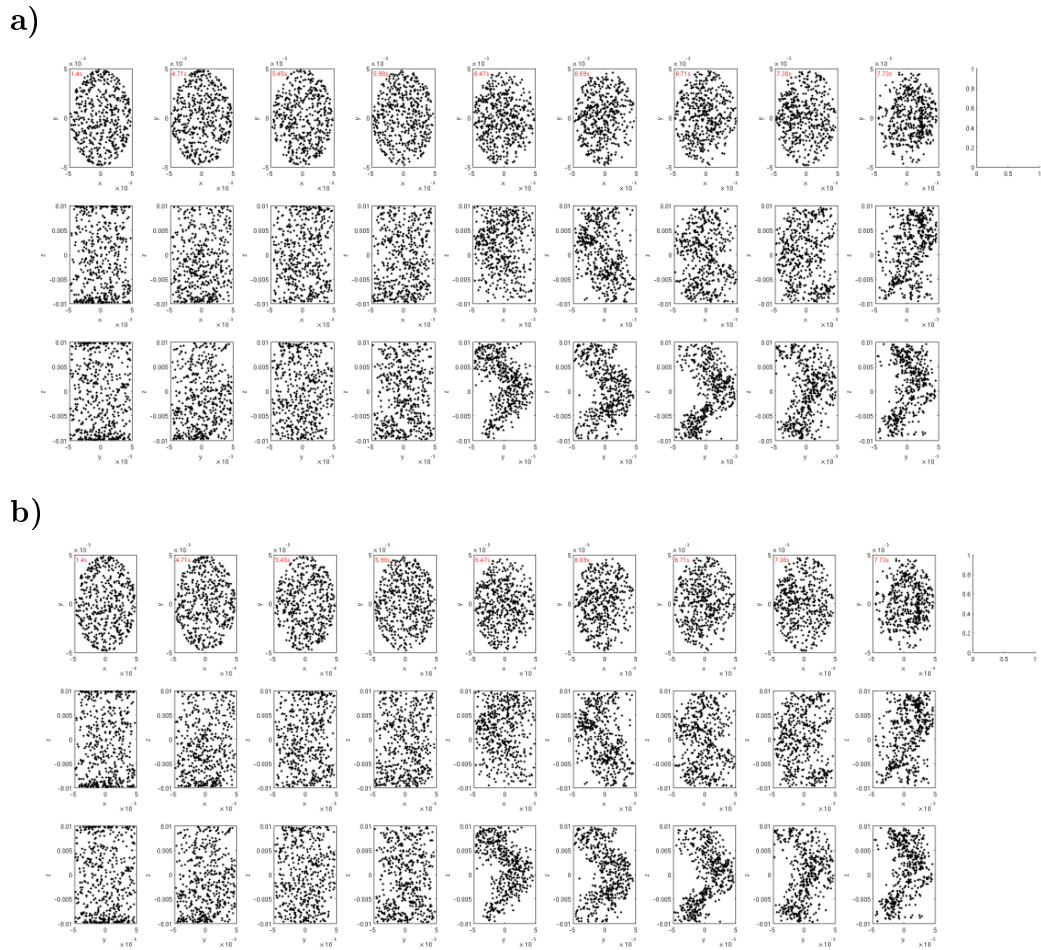


Figure 5.9: Event locations for two simulations at different time steps: a) S7 and b) S7w. For each subfigure top is map view, middle is one side view and bottom is side view rotated 90 degrees from the previous one. The time at which the snapshot was taken is written in the top frames in red.

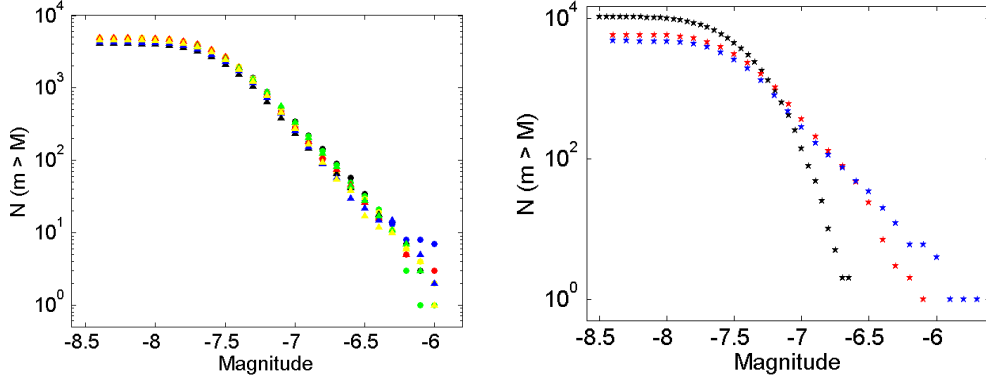


Figure 5.10: (Left) Frequency-magnitude distribution for 10 simulations, 5 with intact samples (filled circles) and 5 with a weakness (filled triangles). Colors are referring to the seed number used for the simulations: see 7 in black, seed 8 in red, seed 9 in blue, seed 11 in green and seed 12 in yellow. (Right) Frequency-magnitude distribution for 3 simulations with different damping factors: $Q=2$ in black, $Q=10$ in red and $Q=200$ in blue.

tude distribution and the anomalous b -value found (cf Table 5.8 for b -values computed for each simulation considered in this analysis). The average b -value for the simulations with intact samples is 2.03 whereas it reaches 2.10 for the simulations with weakened samples. This difference is mainly due to the large b -values found for simulations S9w and S12w. The uncertainty on b for both these cases is also much larger than for the other simulations because big events were actually sparser thus creating outlying values in the distribution and increasing the uncertainty on the slope.

Analysing the temporal variation of the b -value for the 10 simulations (Figure 5.11) shows a decrease before 6 ms, which corresponds to the increase in the applied stress. The lowest b -value is found at peak stress. The relaxation phase is depicted by a plateau in the stress curve and a slightly increasing b -value as it is characterized by numerous small magnitude events. The same behavior is depicted by several authors (Lei, 2003; Lei et al., 2004).

Table 5.8: Values of b computed for 10 repeating simulations considered in this analysis. In the simulation names the letter S stands for ‘seed’ and w for ‘with weakness’.

Simulation	S7	S8	S9	S11	S12
b	1.98 ± 0.03	2.07 ± 0.04	2.01 ± 0.06	2.04 ± 0.04	2.07 ± 0.05

Simulation	S7w	S8w	S9w	S11w	S12w
b	1.96 ± 0.06	2.09 ± 0.03	2.19 ± 0.08	2.09 ± 0.05	2.18 ± 0.1

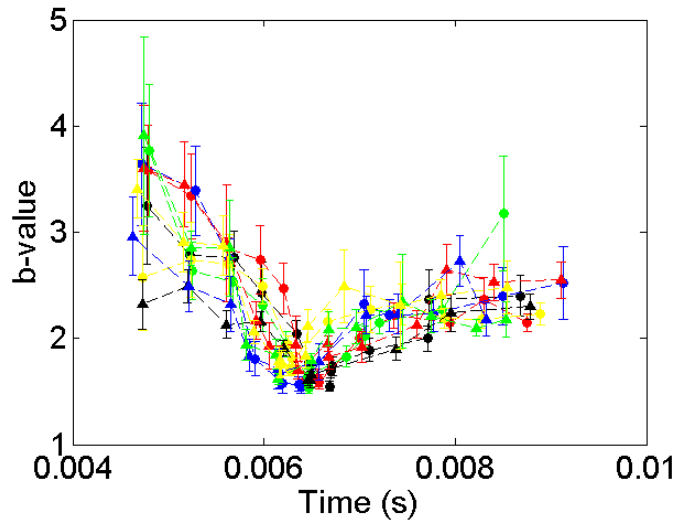


Figure 5.11: Temporal variations of the b -value for 10 simulations, 5 with intact samples (filled circles) and 5 with a weakness (filled triangles). Colors are referring to the seed number used for the simulations: seed 7 in black, seed 8 in red, seed 9 in blue, seed 11 in green and seed 12 in yellow.

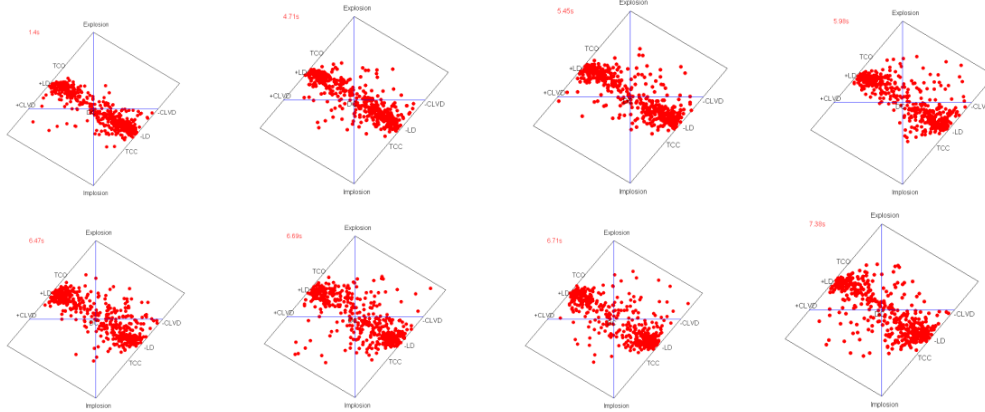


Figure 5.12: Moment tensors represented on Hudson plots for simulations S7 at different times. The time at which the snapshot was taken is written at the top in red.

The BPM allows for a direct estimate of the source mechanism of events by computing their actual moment tensors. Figure 5.12 displays snapshots of these moment tensors represented on a Hudson plot (Hudson et al., 1989) at different times during the simulation S7. The same behavior is found for all simulations including the weakened samples. The general trend in the moment tensors evolve from opening to closing with some double-couple behavior. A minor difference seems to appear after 6.5 s when there is fewer pure double-couple events and the events are now characterized by more closing than opening type mechanisms. Schorlemmer et al. (2005) shows that changes in b -values for earthquakes are related to changes in tectonic stress regimes as shown by earthquake double-couple moment tensors. In our simulations, although the b -value is anti-correlated with the applied stress, the link with the source mechanisms is not that obvious. The volumetric change implied by the isotropic component of the moment tensor seems to be the parameter to affect this correlation.

We also study the relationship between moment magnitude and kinetic energy. In Figure 5.13 we plot the changes in kinetic energy due to an event versus

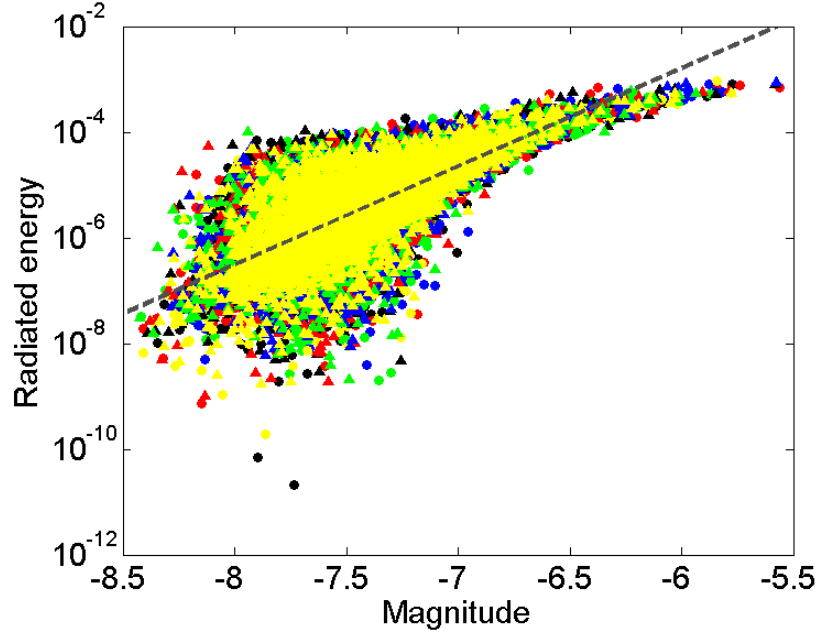


Figure 5.13: Radiated energy versus magnitude plot for 10 simulations, 5 with intact samples (filled circles) and 5 with a weakness (filled triangles). Colors are referring to the seed number used for the simulations: seed 7 in black, seed 8 in red, seed 9 in blue, seed 11 in green and seed 12 in yellow. The dashed gray line represents the best least-square fit for all the data.

its moment magnitude. We suggest an updated empirical energy-magnitude relation following Kanamori (1977):

$$\log_{10} E_K = 1.86 M_W + 8.36, \quad (5.6)$$

where E_K is the energy radiated by seismic waves after failure and M_W is the moment magnitude. This relation should be more suitable for micro-events with various rupture mechanisms including volumetric changes as the previous formula was inferred for large magnitude, strike-slip event. Computing the total kinetic energy for each experiment using this new formula leads to a higher value than with Kanamori's formula but still only accounts for 2.5% of the input energy (cf Table 5.7).

5.2.5 Discussion

Both the damping and friction within the BPM are responsible for losses in the released strain energy as radiated energy (assuming negligible surface energy). In the context of earthquake seismology there is only the non-conservative force of friction acting in resistance to the movement of the upper and lower regions along the fault. It should be noted that for the models here an additional term on the right of equation (5.4) must be added to account for energy lost to damping. This term will affect the magnitude of the radiated energy. It is clear from the simulations on samples Q2 and Q200 there is a discrepancy between the released radiated energies, in particular the energy percentages differ by one order of magnitude. In extreme cases, the damping of the system influences the emitted kinetic energy by at most one order of magnitude.

An updated opposing force, F_F , could be defined as

$$F_F = \mu F_N + F_D, \quad (5.7)$$

where μ is the coefficient of friction along the fault, F_N is the normal force and F_D is the damping force. The damping is simply an additional non conservative force responsible for attenuation in the models. A theoretical quality factor Q for the models would be a symptom of the total force F_F .

This opposing force acts on the particles in the models throughout the simulations so that the net forces are updated accordingly. The moments calculated within the moment tensor algorithm (Hazzard and Young, 2004) are found using the net forces on the particles so that this damping force is intrinsic in the calculation of the moment tensors. The damping has a direct effect on the ratio of the radiated energy over the input energy but is not responsible

for the difference in magnitude between the two separate calculations of the radiated energies further promoting our updated relationship.

The bonded particle models allow direct computation of the input energy, an estimate for radiated energy, and total energy losses to friction. Unfortunately, the energy lost to damping is not monitored. Averaging the input, frictional, and radiated energies for samples S7-12 it is possible to take a closer look at the energy budget. For these bonded particle models the energy budget can be dissected directly (which of course may be overly simplified with respect to the avenues for the energy during earthquakes and hydraulic fracturing). In the bonded particle model there is potential energy of the bonds and contacts, kinetic energy of the particles, energy loss to friction and damping, a very small amount of energy loss due the numerical integration of the discrete system (Itasca Consulting Group, 1999), and boundary work applied by the moving walls. The input energy can transform between only these energy states. With 30% energy lost to friction (which includes both the losses during the rupture process and the attenuation of the seismicity) there is still about 70% of the energy that remains unaccounted for. Certainly a large percentage of this energy is lost to damping. The remainder of the energy must then be stored as strain energy plus the instantaneous kinetic energy still bouncing around in the system. The percentages of kinetic energy at the end of the simulations are negligible. Therefore, in these models, the majority of the input energy is stored as potential energy of the bonds and contacts (where of course this transformation of boundary work energy to strain energy is completely aseismic).

The radiated energy is about 2.5% of the boundary work. The kinetic energy in the models is monitored following bond breakages only so that any of the

kinetic energy associated with the movement of particles not tied to a specific microseismic event is not recorded by the measurement spheres. This sort of aseismic deformation is missing in the total estimate for the radiated energy release. Additionally, it could be possible that there exists noisy events (which do in fact cause seismic waves) associated with an abrupt slip between particles within the sample which is not marked by a bond breakage. Without a particular bond breakage the measurement sphere is not triggered. This sort of event, analogous to slip along a pre-existing fault, could release a significant amount of radiated energy not recorded by the measurement spheres. The total kinetic energy release, including both aseismic and seismic deformation, is likely higher than the values extracted from the models.

Finally, in regards to estimating kinetic energy release in the simulations, the complexity of the ruptures in the bonded particle model is more complicated than a slip along a fault. The rupture is a coalescence of many bond breakages that may not be uniformly distributed in time. Therefore there is not necessarily just one large spike in kinetic energy following an event. There may be peaks and troughs in the kinetic energy curves as a function of time, so that simply computing the maximum change in kinetic energy over the duration of the event may grossly simplify the estimate of the radiated energy.

In a real rock with failure localizing along a plane of weakness or existing joint, some energy would be expected to be lost to frictional work. In the simulations S7w-S12w significant sliding should be observed in the energy budget. For the homogeneous and weakened samples the energy budget is close to identical. The problem with the unbonded region of particles is that they are able to roll. As friction does not work on rolling spheres, there is no additional energy loss due to friction. In order to model a more realistic joint there needs to be

actual physical sliding between the particles. It is possible to try and create a single plane but the rugosity of a surface of spheres creates a very high friction coefficient, and in that case sliding does not generally occur. A smooth joint logic has been created that tries to overcome this (Mas Ivars et al., 2011), but is more applicable to smaller scale sliding only. For these simulations the joint should be imagined strictly as a region that promotes localization of the failure plane and not as a region where energy is lost to friction.

5.2.6 Conclusion

Geomechanical modeling is one technique to provide some insight as to what may be happening in the reservoir. The bonded particle model described in this paper provides a means of modeling both the geomechanical rock deformation and the source mechanisms of microseismicity events along with their respective locations. By directly measuring kinetic energy within the models we suggest here that the actual radiated energy incurred from brittle failure is underestimated by the Gutenberg-Richter relationship to at least an order of magnitude. We suggest a new relation more suitable for small magnitude, non-double-couple type of events. Regardless of this correction, the radiated energy accounts for only 2.5% in the energy budget. Aseismic deformation processes such as frictional sliding (between individual grains and possibly sliding along fractures), damping, and the potential energy stored in the strain of the rock is the culprit for accounting for the majority of the input energy.

Our simulations produce macroscopic behavior indicative of rock fracturing and deformation in the laboratory possibly providing some intuition into the recorded microseismicity observed during hydraulic fracture treatments in the field. Although the experiments are overly simplified and fluid processes are

not introduced within our models, these preliminary results suggest that BPM can be used for modeling more complicated scenarios.

5.3 Discussion and Conclusions

The previous two articles discussed some recent numerical simulations conducted on three dimensional bonded particle models investigating the geomechanics of brittle deformation and its associated microseismicity. The models were shown to replicate actual behavior observed during triaxial tests on rocks in the laboratory (Lockner et al., 1991; Jouniaux et al., 1991). With confidence in the models some conclusions were drawn. The moment tensors computed from the particle motions following bond breakages suggest that the source mechanisms for failure are not entirely pure shear. The Hudson plots indicate both opening and closing type events (see Figure 5.12) indicating an isotropic component to the moment tensors. These sort of Hudson plots have been observed during hydraulic fracture treatments (Baig and Urbancic, 2010) but in general it is assumed that for confined triaxial tests the failure is a Coulomb pure shear where events nucleate along shear bands (Jaeger et al., 2007); the moment tensors are explicitly deviatoric. It may seem surprising that the moment tensors from the numerical simulations have an isotropic component but laboratory experiments conducted on granite do indicate this sort of behavior.

Graham et al. (2009) conducts triaxial tests on Aue granite cylindrical samples at 20 MPa confinement. The samples fail in a brittle fashion with a resulting fault at an angle of thirty degrees from the axis of the cylinder. During the test, acoustic emissions are monitored and events are located using the P-picks from a minimum of eight sensors. Additionally, a moment tensor inversion is

run on the seismic data to obtain the moment tensors for the failure mechanisms of each acoustic emission. Throughout the experiment the moment tensors indicate tensile type failure within the failure zone including the final stages of the experiment (even after the fault has formed). It seems reasonable to conclude that on the micromechanical level, the failure of rock during a confined triaxial test is much more complicated than the commonly assumed pure shear Coulomb type failure. These laboratory tests provide further confidence in the brittle deformation of the bonded particle models previously discussed.

The b-values discussed in the previous two articles are higher than what is expected from laboratory experiments. Lei et al. (2003) found average values around 1 for experiments conducted on granitic porphyry. The averages of the b-values for the numerical simulations here are around 2. Clump based simulations calibrated to that of a granite using a 2-D bonded particle model while running the two dimensional moment tensor algorithm created by Hazzard and Young (2004) also shows reasonably high b-values. Their simulations have an average b-value of 2.6 (Yoon et al., 2012). The higher b-values indicate the brittle failure of the sample is marked by larger amounts of small magnitude events and fewer high magnitude events. The high b-values for both the bonded particle models and the clumped based models are likely a symptom of pure slip events not being recorded. A pure slip event that is not directly tied to a bond breakage will not be recorded using the Hazzard and Young (2004) moment tensor algorithm. The algorithm measures only the force couples strictly following bond breakages. Any sort of slip type deformation with no bond breakage will not be recorded as an acoustic emission. A moment tensor algorithm should be implemented that monitors force changes following pure slip events.

A few final remarks regarding bonded particle geomechanical modeling in the specific context of hydraulic fracturing is mentioned here. The ultimate goal of these bonded particle models is to provide insight into both the geomechanics and microseismicity occurring during hydraulic fracturing of reservoirs. Although the previous simulations were overly simplified in that fluid processes were not employed in the models, they do provide insight into possible micromechanical behavior that may be occurring during brittle deformation of rocks. That being said, hydromechanical models coupling both bonded particle models with fluid flow algorithms do exist. Zhao and Young (2011) create a network of interlocking 'microreservoirs' within the confines of two dimensional bonded particle models. The microreservoirs are connected by conduits (or pipes) running along the contacts between particles in the model. The fluid flow in the pipes are a laminar type flow controlled by Darcy's Law. The fluid pressure in the microreservoirs acts on neighboring particles as equivalent body forces which are summed into the net forces on the particles. The models are able to replicate fluid stimulation of a natural fracture running through a reservoir. Similarly, Yoon et al. (2013) model fracture initiation by fluid injection with 2 dimensional bonded particle models. Coupling fluid flow into 3-dimensional bonded particle models is an active area for further research.

Chapter 6

Aseismic Stress Release and Stable Sliding

In the previous chapter the energy budget during the fracturing of rock undergoing triaxial experiments was investigated using the bonded particle model. As mentioned in the introduction, it is possible that slow earthquakes, on the global scale, may be the result of a stable slide of the overriding and under-riding slabs along the fault (Schwartz et al., 2007). It is possible that on a much smaller scale these sort of stable slides may be a possible explanation for aseismic processes that are speculated to occur during hydraulic fracture treatments.

DEM type models have been used in the past to explore the mechanics behind slippage along faults (Ferdowsi et al, 2013; Mas Ivars et al., 2008). In this next chapter the goal is to investigate the energy budget further with the hopes of tracking down energy losses from stable frictional sliding. Specifically, here it is of general interest to study the energy budget in the context of aseismic stress release. Perhaps aseismic stress release and the small percentage of emitted

seismic energy is a symptom of energy losses due to the force friction along large preexisting faults or joints during stable slides. The main objective of this chapter is to analyze the effect of a joint on the energy budget during triaxial experiments. A jointed sample is created and results are analyzed and compared with a control. Before examining these simulations initial calibration of the joints is conducted.

6.1 Joint Calibration

A rock is very seldom homogeneous in nature. It generally has many fractures or joints which complicate the overall behavior of the specimen. Cracks, fractures and joints will alter the macroscopic elasticity of the rock. Such an intrusion could also alter the local stress field of the rock deviating local principal stresses from their global principal directions. It is of general interest to understand how joints alter the behavior of a rock sample, although the primary objective here is to investigate how a joint accommodates deformation and reduces emitted seismic energy. Before investigating joints within the confines of a large sample (with applied boundary conditions) the nature of slip along a simple joint must be explored.

An environment is created to apply direct shear tests between an upper and lower slab to estimate both the coefficient of friction and the mechanical nature of slide. See Figure 6.1 for an image of the direct shear test environment. The bottom platform of the sample is held in place by surrounding walls, whereas the top part of the sample is pushed by an upper panel on the right. The upper and lower walls apply a constant normal stress on the plane of the joint. The applied shear stress of the upper panel is monitored. In this manner, the

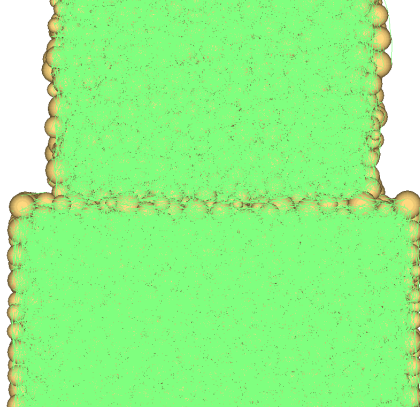


Figure 6.1: Shear test environment. Parallel bonds are removed that intersect an imaginary plane between the upper and lower slabs.

coefficient of friction and cohesion of the surface of the joints can be calculated.

When a sample is created using the BPM, the particles are tightly packed, overlapping and bonded. To create a fracture or joint within the sample, the bonds between desired particles must be removed or altered. The first attempt at creating a joint in the sample is to remove all the bonds crossing the plane marking the intersection of the top piece and the lower piece.; see Figure 6.1. A routine removes all the bonds crossing this plane and the direct shear test is applied. The results from the tests are seen in Figure 6.3a-f. The images show the applied shear stress vs. wall strain. The wall strain in the experiment is a measure of the distance traveled by the upper panel over the width of the base of the specimen. It should be noted that increasing wall strain does not necessarily indicate slippage of the sample. As mentioned in Chapter 3, the wall is allowed to overlap with particles; the force on the individual particles is proportional to this overlap. Additionally the strain may be a result of elastic deformation of the medium.

In general the expected behavior of these direct shear tests will be a rise in shear stress (where elastic deformation of the rock occurs as the upper and lower slabs are locked due to friction) until the failure shear stress is reached.

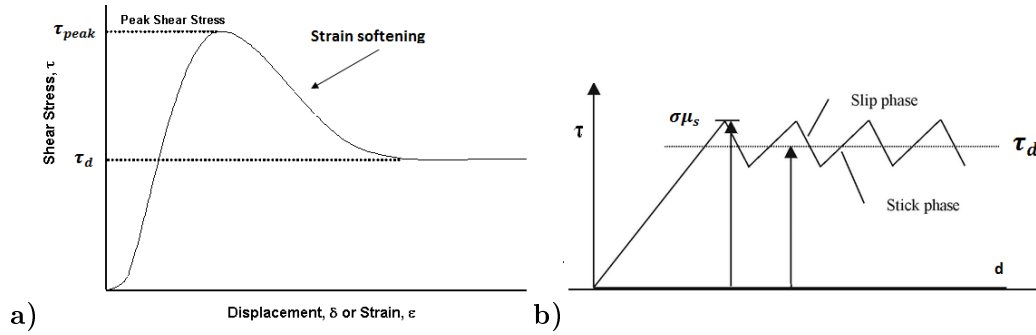


Figure 6.2: Idealized behavior for slipping along a joint. a) Curve indicating the peak shear stress due to the coefficient of static friction and the dynamic shear stress due to the coefficient of kinetic friction. b) Stick slip type behavior. The peak shear stress due to the coefficient of static friction is labeled. The dynamic shear stress is the average of the stick and slip phases. Images taken from the web.

There than is an an abrupt drop or gradual strain softening as the shear levels drop off onto the the dynamic value. The peak stress is due to the coefficient of static friction where as the dynamic shear stress is a result of the coefficient of kinetic friction. See Figure 6.2a for this idealized behavior. In the case of stick-slip sliding there is an oscillatory back and forth between stick and slip resulting in an incessant rise and fall of the shear stress. The average value for the rise and falls for the shear stress is the dynamic shear stress for the stick slip oscillation. See Figure 6.2b for this idealized behavior. The direct shear tests are now applied to the bonded particle models.

The maximum shear stress in the simulations are fairly high and in all cases are quite close to the confinement pressure suggesting a high coefficient of friction. The rise in shear stress due to the elastic deformation is clearly observed. In Figure's 6.3b-f with non zero confining stress the post peak shear stress dramatically drops leveling off on the constant dynamic shear stress indicative of the coefficient of kinetic friction. In the images, the distinct effect of the static and kinetic friction coefficients (as defined in Chapter 2.3) on the shear stress are readily observed. As the peak shear stress drops off to

the constant value $\sigma\mu_d$ a number of time steps is needed to reach this value. In fact there looks to be evidence of strain softening (which is very pronounced for the test at 5 MPa confinement). The shear stress gradually decreases and is not an abrupt process for the simulations at lower confinement pressure. In the context of the structural geology of faults, a mechanism called granular flow is the result of both frictional sliding and rolling of the grains along the fault. It generally occurs when the boundaries between the grains are much weaker than the individual particles. This sort of behavior will occur at low effective confining pressures (shallow depths or high pore pressure). The behavior is often observed as unconsolidated sediments slump due to very little cohesive strength between the grains (Davis, 1942). The direct shear tests show this sort of behavior as increasing confinement pressure leads to more abrupt drops in the shear stress. The strain softening is likely a result of granular flow comprised of both frictional sliding and the rolling of the spheres in the models.

From the peak failure shear stress, $|\tau_f|$, along with the normal confinement pressure, σ , the static coefficient of friction and joint cohesion can be estimated by linearizing the data using equation (2.25). The linearized data will then provide an estimate for the coefficient of static friction, μ_d , and the surface cohesion, S_0 . See Figure 6.6a for the resulting Coulomb friction curve. The data shows a clear linear trend with $\mu_s = 0.69$ and $S_0 = 3.570$ MPa. This is within reason for actual laboratory friction tests conducted on dry sandstones by Rae (1963). The coefficient of the static friction for these first simulations look to agree with shear tests conducted on dry sandstones.

The ultimate goal is to try to model stable sliding with low coefficients of friction. Stable sliding is one possible mechanism that may be responsible for

slow slip events observed at subduction interfaces around the world (Schwartz et al., 2007). Although in nature it is expected that complicated fluid processes play an important role in the mechanism for stable sliding (Sleep et al., 1992) an attempt must be made to lower the coefficient of friction on the joint without the introduction of complex fluid mechanics into the models. For a good stable slide the desired results of the shear test curves should be similar to the idealized behavior shown in Figure 2.2c where there is a horizontal plateau indicative of stable frictional sliding (or plastic deformation).

In order to simulate a slow slip event the coefficient of friction for the joint must be substantially lower than 0.50 and the mechanism of slide should be stable (no stick slip oscillation and/or abrupt slips). To reduce the coefficient of friction of the joint a region of thickness 0.0009m is unbonded (whereas in the previous simulations the bonds were only removed that crossed the intersecting plane). In short this new joint logic removes many more bonds between the particles; this region is marked in Figure 6.4a by the particles in red. Figure 6.4b shows the region is clearly unbonded with no parallel bonds holding the upper and lower regions together (the parallel bonds are indicated in green). Direct shear tests are applied using this new configuration and Figure 6.5a-h shows the results for the direct shear tests vs. wall strain.

The results of the tests show stable slides followed by gradual decay (see Figure's 6.5a-h). Again this strain softening is likely a result of the spherical nature of the particles. The spheres act as a means for the upper slab to roll along the bottom slab. So the deformation is marked by a granular type flow where there is both rolling and sliding of the particles. In general, the curves are fairly horizontal and similar to the idealized behavior in Figure 2.2c. At confinement pressures as high as 40 MPa there is little stick slip behavior (a few

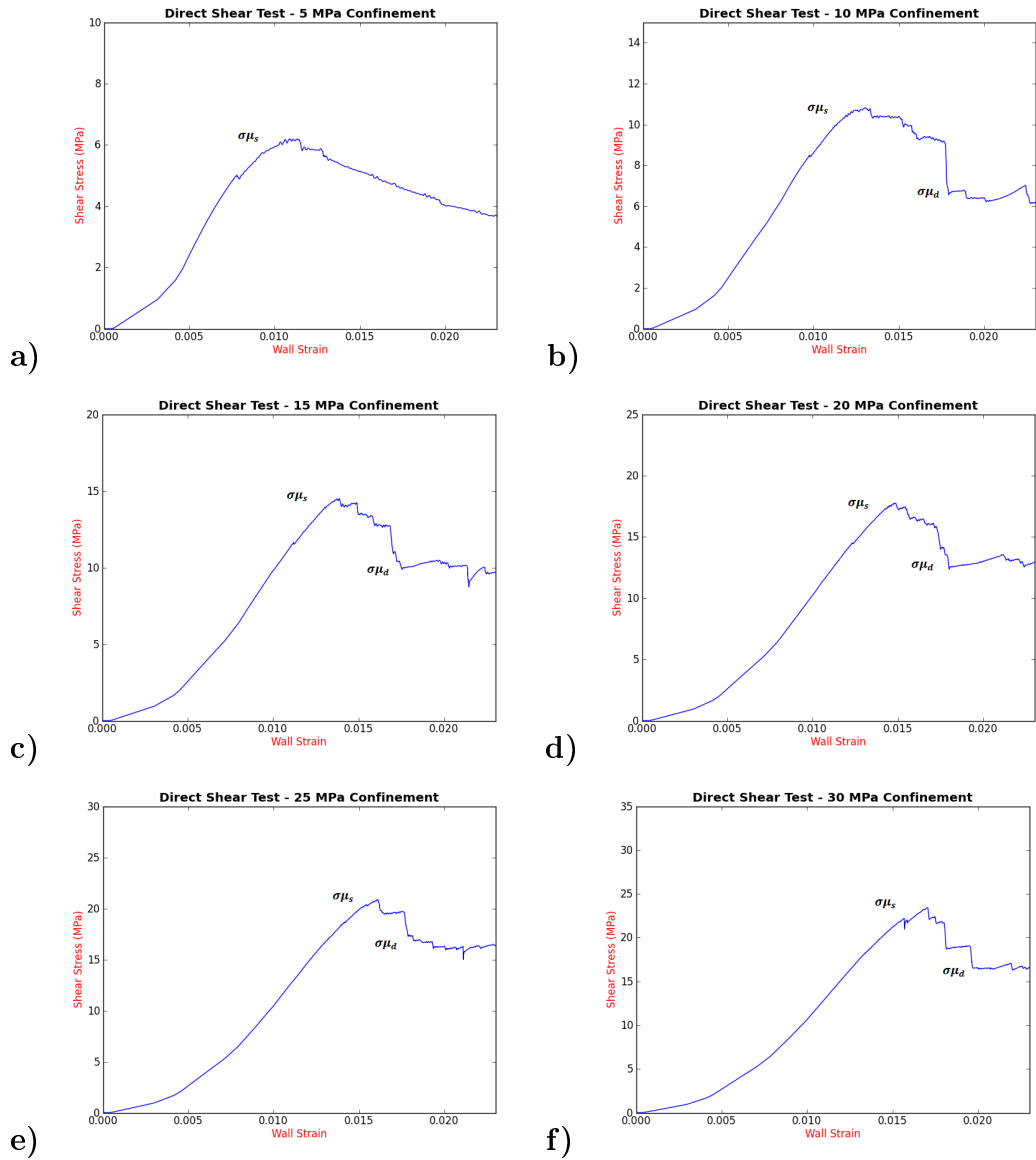


Figure 6.3: Results for shear test on a high friction joint. a) 5 MPa confinement. b) 10 MPa confinement. c) 15 MPa confinement. d) 20 MPa confinement. e) 25 MPa confinement. f) 30 MPa confinement.

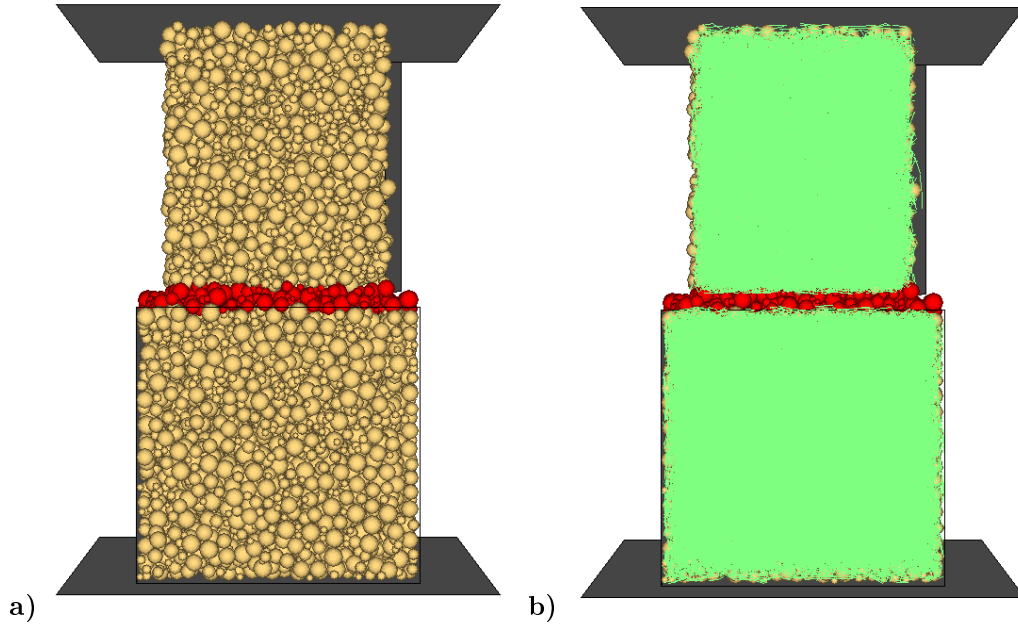


Figure 6.4: Updated shear test environments. a) Particles in red are unbonded. b) Regions in green show the parallel bonds.

minor slips are observed). The sliding causes minimal failure of the medium as very few bond breakages are observed; with only 84 cracks. Consequently, the new region of unbonded particles provides the condition for the system to slide in a stable fashion. A plot of the shear stress failure vs. normal stress is in Figure 6.6b. The plot shows linear Coulomb type friction with $\mu_s = 0.27$ and $S_0 = 0.90$ MPa. The friction and surface cohesion on the joint is quite low and are exactly the behavior desired for modeling a stable slide that may be the mechanism responsible for aseismic slow slip.

These first simulations highlight that the BPM is capable of modeling a broad range of deformation including elastic, brittle (discussed in detail in Chapter 5), stick slip sliding, stable frictional sliding, granular flow and even approaching plastic behavior. A number of conclusions can be drawn; the coefficient of static friction along the joints is inversely proportional to the thickness of the shear zone. Larger fault zones have much lower friction coefficients as the models allow a granular type flow where the particles roll. The granular

type flow is more pronounced at lower confinement stress (see Figure's 6.3a-f) which agrees with the structural geology for faults at shallow depths or high pore pressure. These joints are now in a position to explore some more complicated scenarios.

6.2 Internal Shearing on a Fracture

With a calibrated joint behaving in a fairly stable fashion uniaxial tests are conducted on the calibrated models from chapter 4 with the addition of joints in the center of the samples. See Figure 6.7b for a cross section showing the joint marked in red (the particles in red are unbonded as discussed in the joint calibration previously). It is of interest to see how these jointed numerical models compare with the theoretical micromechanical model discussed in Chapter 2. A number of uniaxial tests are conducted on the cylindrical sample with joints inserted while varying the angle β from the axis of the cylinder to the unit normal of the joint plane. These uniaxial tests are conducted on cylindrical sleeves whereas the theoretical micromechanical model, from (2.27), is for thin rectangular plates of dimensions L and b with thin finite thickness, t . In both cases, $\sigma_2 = \sigma_3 = 0$, and so that using equation (2.5), the magnitude of the shear stress's are the same. The results should follow the same general trend.

The results of the uniaxial tests are compared with the theoretical micromechanical model from equation (2.27). The theoretical micomechanical model curve showing the relationship between the effective Young's modulus and angle β is shown in blue in Figure 6.7a. For this curve the parameters are, $\mu = 0.27$, $L = 0.02m$, $b = 0.01m$, $c = 0.0025m$, and $E_m = 39.0GPa$. The

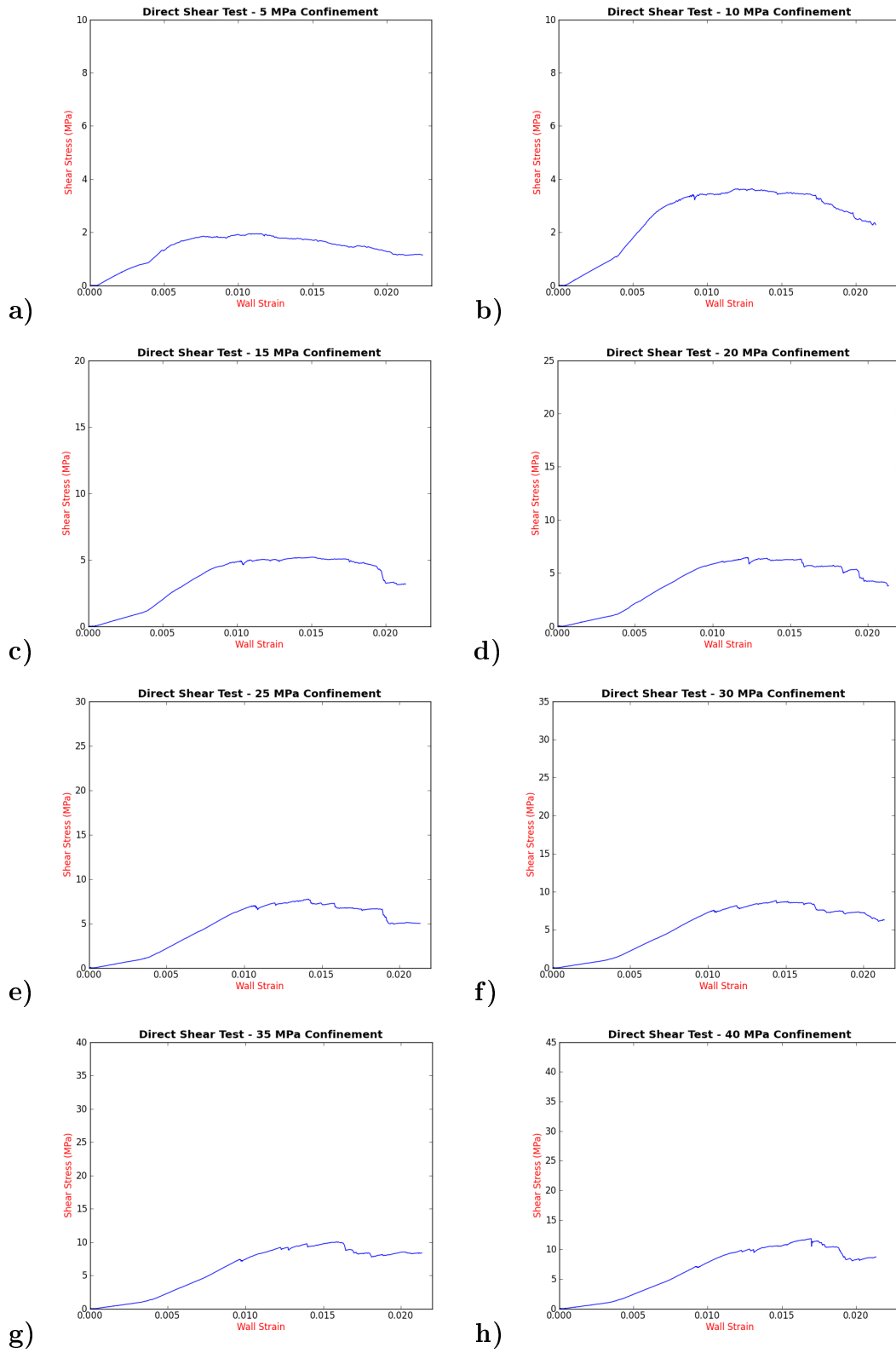


Figure 6.5: Shear stress vs. strain for low friction joint at various confinements of: a) 5 MPa. b) 10 MPa. c) 15 MPa. d) 20 MPa. e) 25 MPa. f) 30 MPa. g) 35 MPa. h) 40 MPa.

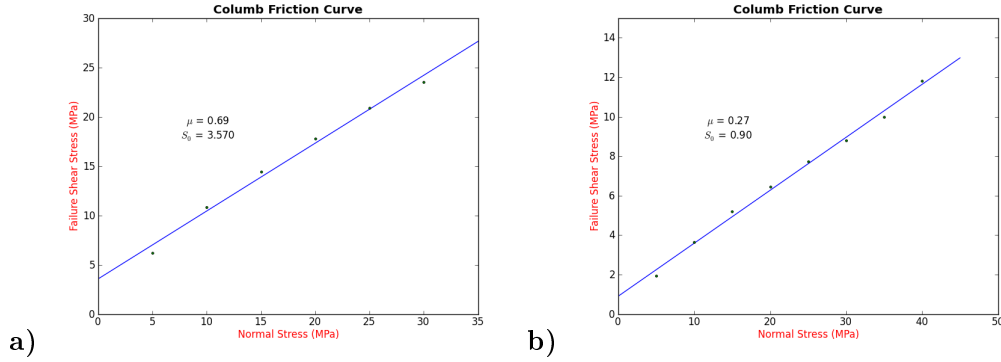


Figure 6.6: Failure shear stress (peak) as a function of the confinement pressure. a) Results for the thin region of unbonded particles b) Results for the thick region of unbonded particles.

measured Young's modulus and UCS for the BPM's at various angles are in Table 6.1 and are also plotted in Figure 6.7a in green. Figure 6.7a clearly shows that the magnitude of the measured Young's moduli from the BPMs are about 5% lower than what is expected from the theoretical micromechanical model. There also looks to be a small shift in the data; further analysis should be conducted to provide an explanation for this behavior but is not explored here.

The joint from the bonded particle models has a measurable thickness whereas the micromechanical model assumes an infinitely thin, closed crack. The thick joint within the bonded particle model creates a soft region which reduces the overall stiffness of the sample. When $\beta = 0$, the joint is perpendicular to the compression axis and the majority of force chains now run through this soft asperity reducing the overall Young's modulus of the sample. The Young's modulus is higher when $\beta = 90^\circ$ than at $\beta = 0$ as the compression axis is now parallel to the joint so that the force chains avoid the weakness and channels around the inclusion through the surrounding stronger medium.

Although the joint has a measurable thickness and is not infinitely thin, the behavior of the measured data does follow the general trend of the theoretical

Table 6.1: Young’s modulus and UCS for the jointed sample at various angles for the measured values from the BPM.

	0°	15°	30°	45°	60°	75°	90°
E	37.86 GPa	37.63 GPa	37.52 GPa	37.41 GPa	37.67 GPa	37.97 GPa	38.08 GPa
C_0	169 MPa	168 MPa	168 MPa	158 MPa	163 MPa	169 MPa	170 MPa

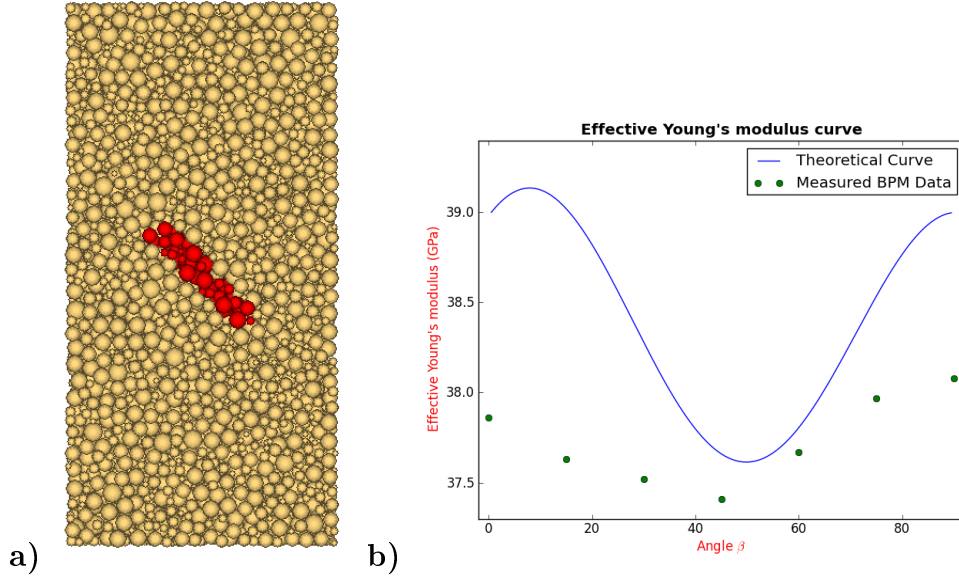


Figure 6.7: a) A cross section of the BPM showing the joint (in red) within the sample. b) In blue is the theoretical curve for the micromechanical model using equation (2.27) where the parameters are $\mu = 0.27$, $L = 0.02m$, $b = 0.01m$, $c = 0.0025m$, and $E_m = 39.0GPa$. The points in green are the results from the BPMs.

effective Young’s modulus curve. A thinner sliding plane would provide a more accurate representation for the theoretical micromechanical model; nonetheless the current bonded particle model does reproduce expected macroscopic behavior and provides additional confidence in the models.

6.3 Energy Budget for Stable Sliding on a Joint

With a few simulations on these joints accomplished it is time to explore their overall effects on the energy budget. The objective here is to explore the relationship between stable sliding on a joint to some sort of aseismic stress

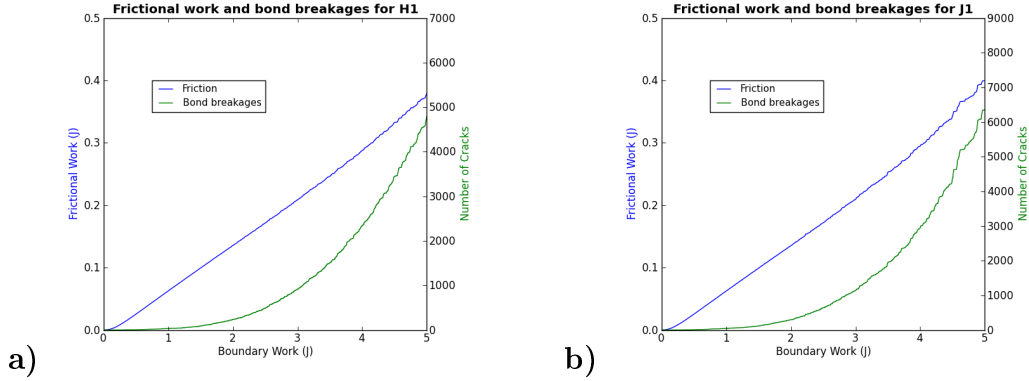


Figure 6.8: Frictional work and bond breakages as a function of increasing boundary work. Frictional work on the left side in blue and number of cracks in green on the right side. a) Sample H1. b) Sample J1. Note the vertical scale for number of cracks is different.

release. Two large samples are created with the hopes of providing increased resolution of the models. A cylindrical sleeve of around 73,000 particles is created. The micro-parameters of the samples are identical to those discussed in Chapter 4 (see Table 4.3). The Young’s modulus and Poisson’s ratio are similarly 39.0 GPa and 0.26, respectively. As discussed in the second article from Chapter 5, the damping of the system needs to be considered as high damping leads to less kinetic energy emitted throughout the models. Again the damping parameter, α , is set at 0.05236 to provide a Q factor of about 30.

Two models are created; a control, H1, and a model with a joint added, J1. The radius of the circular joint is 0.0025m and the angle is 45 degrees from the axial direction. The coefficient of friction on the joint is 0.27 and the surface cohesion is 0.90 MPa as discussed in section 6.1. In this triaxial experiment the bottom platen is fixed while the top platen closes on the sample and the simulations are run until failure. Throughout the simulations the boundary work, frictional work, and bond breakages are monitored. The total frictional work monitored within the models includes all energy losses to friction which includes both the micromechanical losses (such as grain to grain contacts as

the particles move around) and macroscopic losses (such as large scale sliding along a joint). Therefore spikes in frictional work may not necessarily be from large scale sliding; it may be the result of micromechanical losses of kinetic energy following microseismic events.

The total energy lost to friction as a function of boundary work is plotted for both samples for an input energy of 5J; see Figure 6.8. The frictional work from sample J1 is larger at 5J of boundary work than sample H1 at, respectively, 0.41J and 0.37J. At first glance it seems reasonable to suggest this may be a result of energy losses due to frictional sliding along the joint.

The sample J1 is weakened by the joint and fails at substantially less input energy than sample H1; from Figure 6.8b, at 5J of boundary work, there is about a thousand more bond breakages for sample J1 than H1. See Figure 6.9a for the stress strain curves. Examining the bond breakages as a function of boundary work in Figure 6.8 shows a direct correlation between friction and the bond breakages. Large jumps in frictional work follow large bond failure events. When the bonds break, released kinetic energy causes rapid motion of particles within the sample. The force of friction acts in opposition to the accelerating particles. The friction between the spheres causes large amounts of frictional work post bond breakages. A more careful examination needs to be conducted to determine the overall effect of the joint on the frictional work of the triaxial simulations. To separate the effects of micromechanical friction losses from any potential macroscopic friction losses the energy budget needs to be examined at a point in the simulation where the slip is in process but there are no bond breakages that act to skew the frictional energy losses.

As the axial stress is applied to the sample J1 eventually the shear stress on the joint becomes large enough so that there is slip. The radial stress during

the simulation is constant and maintained at 20 MPa so that when the axial load reaches around 37.26 MPa, from formulas (2.6) and (2.7), the normal and shear stress at the surface of the joint is calculated to be 28.63 MPa and 8.63 MPa, respectively. Plugging in $\mu_s = 0.27$ and $S_0 = 0.90MPa$, from formula (2.25), the shear test criterion for failure is then 8.63 MPa. So at an axial load of 37.26MPa, given the calibrated coefficient of friction, sliding should occur. The frictional sliding along the joint should be expected to cause boundary work energy losses to frictional work.

To ensure the theoretical axial load of 37.26 MPa for slippage matches observations in the models the stress strain curves are examined. In Figure 6.9b the two curves are the same and then diverge at about 17 MPa differential axial stress (or 37 MPa axial load); this region is highlighted by the red box. For sample J1 the joint is initially locked than at an axial load of 37 MPa slip occurs which causes softening of the sample as the J1 stress strain curve diverges from the H1 stress strain curve. During this initial elastic regime of the models, there is minimal failure so that any increases in frictional work is a result of macroscopic sliding and not the attenuation of kinetic energy following bond breakages. At the time of initial sliding the boundary work on both samples H1 and J1 is 0.0788 J. At an arbitrary input energy of 2 J (chosen further along in the simulation where there is still minimal failure of the samples) the energy loss to frictional work for H1 and J1 is 0.1355 J and 0.1353 J, respectively. At this point along the stress path of the simulation the criterion for sliding has long been met and there is negligible differences in frictional work between the two samples. The sliding along the joint occurs but with minimal effect on the frictional work for the energy budget of the simulation. It turns out that a stable slide marked by frictional sliding and rolling spheres causes a negligible amount of input energy losses. In short,

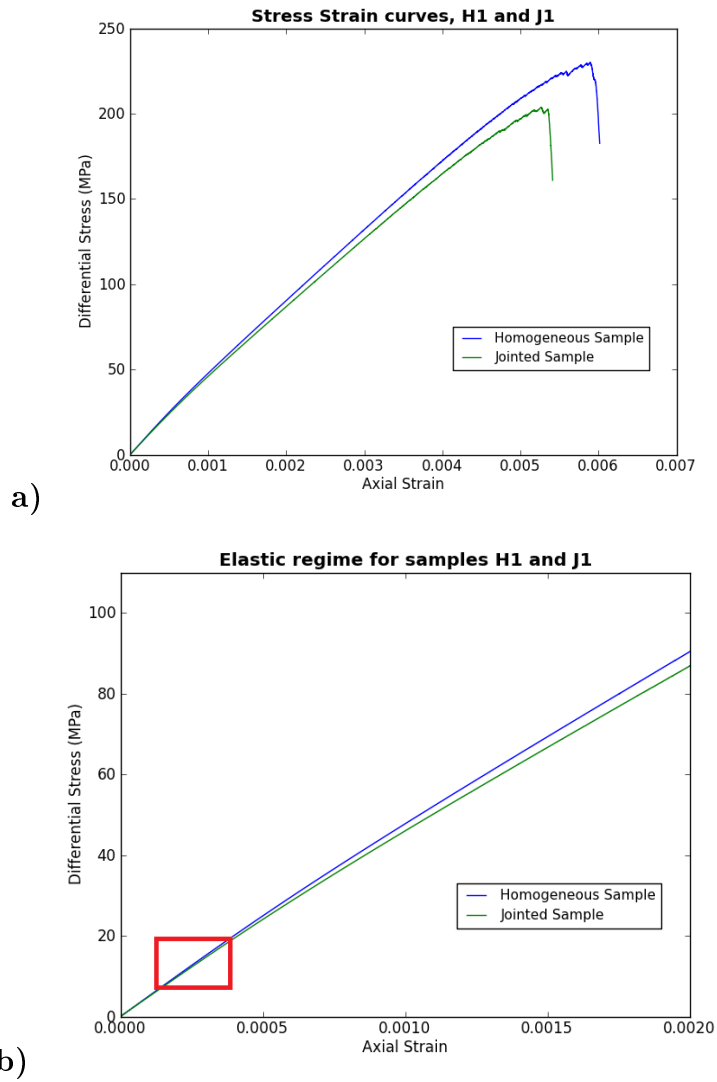


Figure 6.9: Stress strain curves for homogeneous samples H1 and jointed sample J1. a) Curves showing the elastic and brittle regimes. b) The elastic regime of the curves. The region highlighted by the red box indicates when the sample J1 undergoes softening due to slippage.

this sort of aseismic deformation of the samples looks to account for minimal energy loss.

6.4 Discussion and Conclusions

The objective of this chapter was to investigate stable sliding as a means of aseismic deformation that is speculated to be an integral mechanism for slow slip events. In particular, this was conducted by exploring the behavior of frictional sliding and its implications on the energy budget.

The simulations from section 6.1 show that the BPM is able to model complicated forms of deformation including stable friction sliding, granular type flows, and more abrupt slips characteristic of stick slip sliding. As confinement pressures increases the granular type flow evolved to the more traditional idealized friction where there is a coefficient of static friction and the coefficient of kinetic friction. At high pore pressures and shallow depths (low confinement pressure) granular type flows are a viable mode of deformation that could potentially occur at both subduction interfaces and possibly during hydraulic fracture treatments. There is an inverse relationship between the size of the shear zone and the coefficient of friction of the joint/fault. The larger shear zone created behavior more indicative of stable sliding (but did still exhibit some granular type flow behavior).

From Section 6.3 there is minimal energy loss due to sliding along the joint. As the confinement on the samples is maintained at a constant 20 MPa, it is likely the magnitude of the slip is quite small (additionally the curves for H1 and J1 are quite similar). It is possible a large slip along a large fault (such as the case in plate tectonics) would in fact show more pronounced energy losses due

to the slide. That being said, the stress strain curves do indicate slippage and negligible frictional work. The problem with the unbonded region of particles is that they are able to roll. As friction does no work on rolling spheres, there looks to be minimal energy loss to friction.

Sliding behavior marked by rolling particles is observed in nature and is called granular flow. Granular flow is comprised of frictional sliding and rolling particles and is a known geologic effect (Davis, 1942). Such a flow can happen during fault slippage causing flows that are responsible for strain softening as they essentially provide a lubrication for the fault surface.

From the following simulations it seems reasonable to conclude that relatively small amounts energy is lost to friction when there are rolling particle grains along preexisting joints. If the mechanism behind an aseismic slide at a subduction interface or a joint within the neighborhood of a hydraulic fracture treatment is rolling grains than minimal input energy is lost to friction. In the case of a granular flow the input energy will be stored predominantly as strain energy or perhaps the acceleration of the upper and lower regions with respect to one another.

These bonded particle models suggest that if any aseismic deformation along a joint involves granular flow type processes there is negligible energy losses due to friction along the joint. In general, it may be reasonable to conclude that minimal energy is released during aseismic stable sliding at convergent fault margins and during hydraulic fracture treatments. With about 2.5% of the input energy released as kinetic energy following failure (see Chapter 5), the majority of the input energy is stored as potential energy of the contacts and the parallel bonds. The strain energy of the rock makes up the largest portion of the energy budget.

Chapter 7

Seismicity and Radiation Patterns

So far rock fracturing, energy budgets, and moment tensors have been investigated. The objective of this final chapter is to briefly explore wave propagation and to discuss some areas of further interest for future research.

7.1 Wave Propagation

From a seismological standpoint, wave propagation is generally modeled by solving the full 3-D wave equation (most commonly using finite difference methods). With moment tensors for failure estimated in the bonded particle models the next question to ask is, do the particle motions from failure lead to wave propagation? With a Hooke's law type formulation acting between the contacts of the discrete spheres, discussed in Chapter 3, it seems plausible. Toomey and Bean (2000) show that wave propagation can be modeled using a DEM approach for 2D models. In particular, the particles in their models are disks and are packed hexagonal so that a central disk is surrounded and is in contact with six other disks. They manipulate source particles, monitor

receiver particles and compare the resulting wave velocities with finite difference models. They find the results to be within very close agreement. In the following section wave propagation will be independently investigated for the 3D bonded particle models that have been discussed throughout this thesis.

The Triaxial Experiments and Microseismicity

When boundary conditions are applied to the bonded particle models, such as the triaxial tests discussed throughout Chapter 5, bond breakages and microseismic events occur. In particular, the source mechanisms for these events were investigated using the moment tensor algorithm created by Hazzard and Young (2004). The first step here is to examine the instantaneous motion of a particle during a triaxial simulation.

Figure 7.1 shows the instantaneous velocity vs. time step for a receiver particle during a triaxial simulation from Chapter 5. A receiver particle in the model is simply a particle that is monitored throughout the simulation. The figure shows the velocity of the receiver particle in the x , y , and z directions. This receiver particle is analogous to a three component geophone.

Are these spikes in velocity tied to bond breakages of the sample? Figure shows the evolution of the bond breakages laid overtop of a seismogram. It is observed that as the bond breakages start to increase there is a greater occurrence of spikes on the seismogram. Figures 7.3a and 7.3b show a zoom in view of the red rectangle in Figure 7.2. Figure 7.3a shows a large coalescence of around 3000 cracks. Examining Figure 7.3b, a short number of time-steps following the jump, there is a large spike in particle velocity. It looks as though the large spike in particle velocity is directly correlated to failure within the

sample. When a bond breaks, kinetic energy is released and seismic waves are emitted. Are these P and S waves traveling through the sample following the microseismic events? It is now time to take a closer look at the elastodynamics of the bonded particle model in a more controlled fashion.

P and S Waves

By monitoring receiver particles in the sample throughout a triaxial simulation synthetic seismograms are readily observed. The next step is to track down seismic velocities in a more controlled setting and then compare these velocities with the theoretical velocities derived from the elasticity constants E and ν using equations (2.33) and (2.34).

A new, high resolution (smaller particles), cylindrical sample is created, *HRS1*, with the micro-parameters from Table 4.3 (including $\alpha = 0.05236$), except there are now close to 80,000 particles. The porosity of sample is 0.3505 and the density of individual balls are $3400\text{kg}/\text{m}^3$. The sample density, Young's modulus and Poisson's ratio is $2208\text{kg}/\text{m}^3$, 40.0 GPa and 0.253, respectively, which are found by conducting uniaxial compression tests (exactly as in Chapter 4 Section 4.3). The large sample is created to allow for natural propagation of the waves. For these discrete models, dispersion and scattering of the waves must be considered as small wavelengths will have an effect on the phase velocities (certainly a wavelength the size of a single particle will scatter). Toomey and Bean (2000) investigated the effects of the wavelength on the dispersion and scattering of their lattice models and found that if the wavelength is larger than ten particles it was below a detectable level. Here the minimum wavelength is set to ten times the average size of the particles in the sample; which is 0.00247 m.

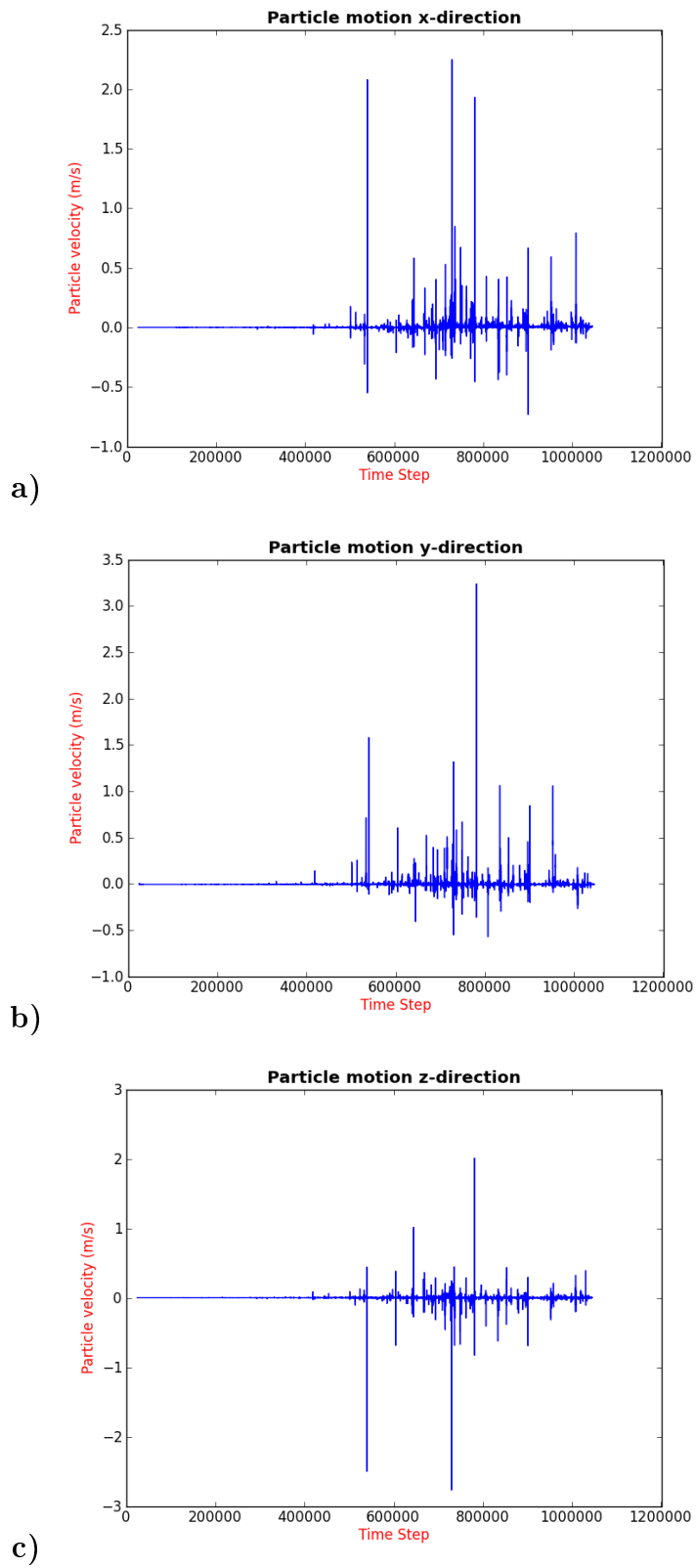


Figure 7.1: Particle motion in the x , y , and z direction for a particle in the sample throughout triaxial test conducted in Chapter 5.

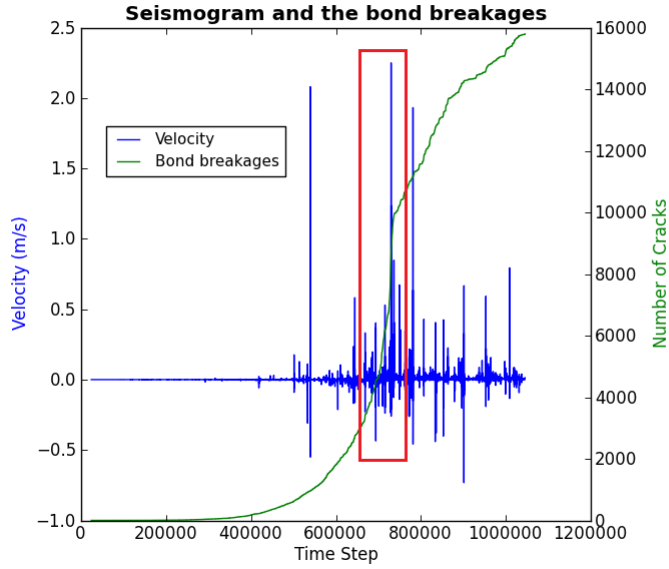


Figure 7.2: Seismogram and bond breakages superimposed. Red box indicates a large spike in particle velocity and a dramatic increase in bond breakages.

For the propagation of seismic waves there is both a near field term and far field term (see (2.35) from Chapter 2). If the wavelength is much less than the distance from the source to the receiver it can be assumed that the near field term is negligible and only the far field terms need to be considered. The distance here is set to be at least 5 times the wavelength to prevent near-field contributions. Within the calibrated sample a source particle is chosen along with six receiver points. The source point and receiver points vary along the axis of the cylinder where the minimum distance from the source to the receiver is .014m (see Figure 7.4). The number of wavelengths from the source to the closest receiver is about five and a half.

From the elasticity constants, using equations (2.33) and (2.34) the P and S wave velocities are $4676m/s$ and $2689m/s$, respectively. Assuming the minimum wavelength of 0.00247 m the maximum frequency for the P waves is close to 1.8 MHz and for the S waves is about 1.1 MHz. The source particle velocity here is manipulated to emit a single period of a sinusoidal wave at a

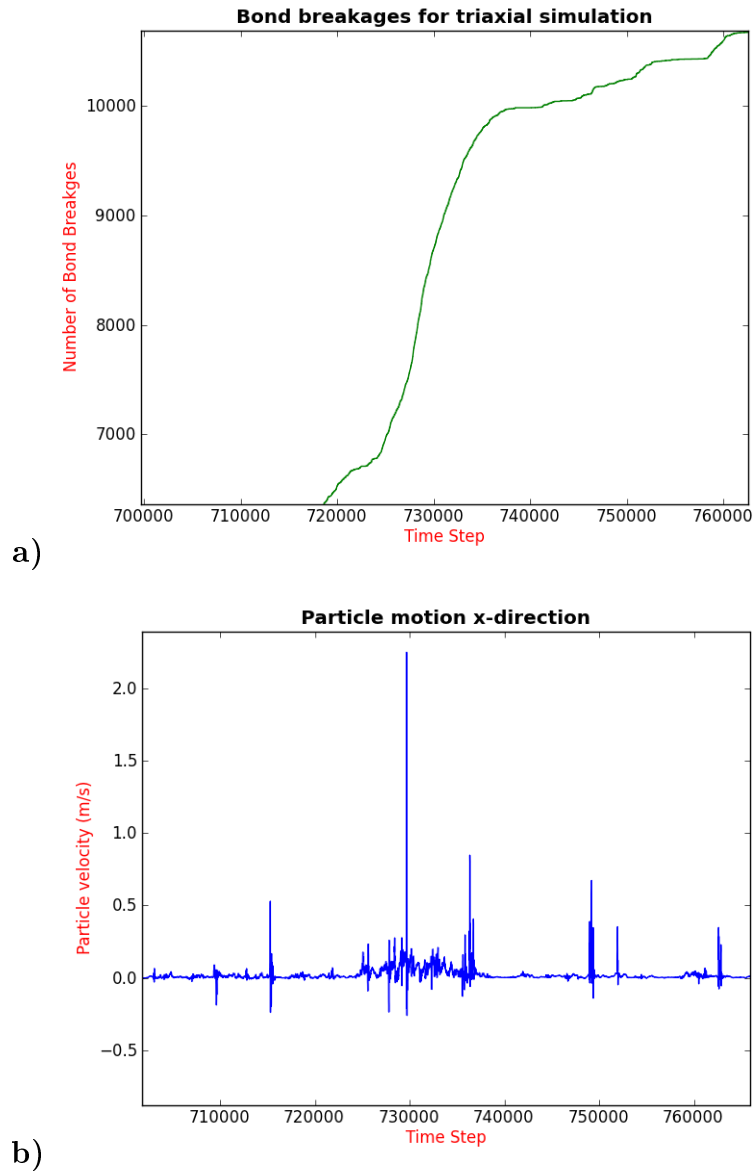


Figure 7.3: a) Zoom in of bond breakages for triaxial simulation; a jump in around 3000 bond breakages. b) Seismogram magnified showing particle velocity shortly after the large jump in bond breakages.

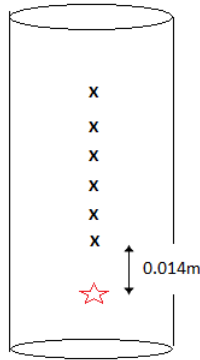
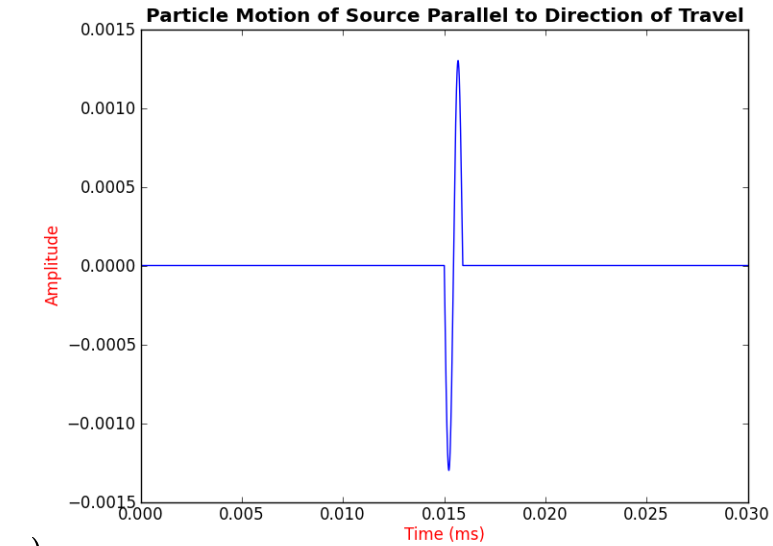


Figure 7.4: Sketch of the array running up the axis of the cylindrical sample. The closest distance from the source to a receiver point is 0.014m.

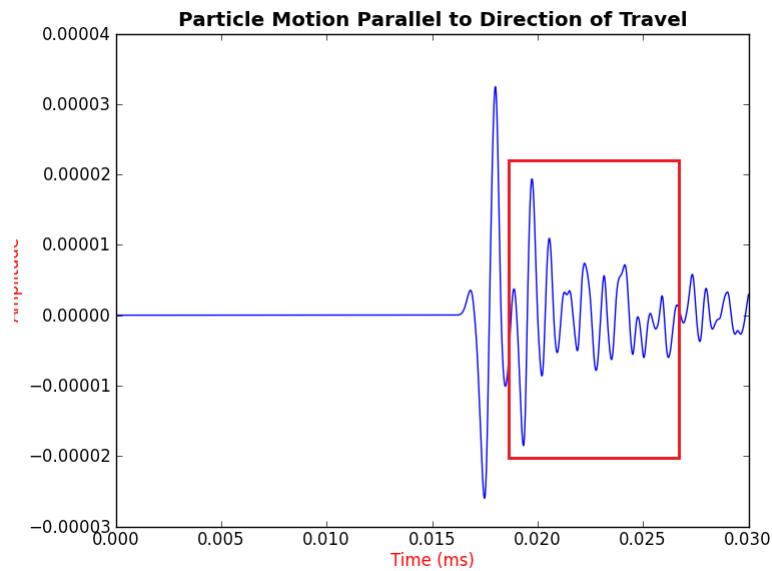
frequency of 1.8 MHz for the P waves and 1.1 MHz for the S waves. The 1.8 MHz source signal is shown in Figure 7.5a.

For the P waves, the source particle is manipulated in the axial direction and the particle velocity of the receiver is monitored in the axial direction (the particle motion is parallel to the direction of travel). Six receiver points are set (see Figure 7.4 for a sketch of the array.) See Figure 7.5b for an example of the signal observed at the first receiver point. With the source receiver distances known, the velocities are estimated by measuring the time between the peak of the wave at the source to the time of first peak of the wave at the receiver. The peaks of the waves are used (as opposed to the first arrivals) as farther from the source the data is noisy due to effects from scattering and the reflections. Averaging the velocities for six receiver points gives a value of $4747m/s \pm 73m/s$. The dynamic wave velocity of the sample is about 1.5% faster.

Similarly, for S-waves generated with polarizations perpendicular to the source-receiver axis the average velocity of the sample is $2969 \pm 88m/s$. The measured velocity is about 10% faster than the velocity calculated from the elasticity



a)



b)

Figure 7.5: a) Shows the source wave, frequency of 1.8 Hz. t_0 was set at 0.015 ms to ensure any existing kinetic energies in the models are completely dissipated. b) The receiver signal at 0.014 m, showing the first arrival along with later arrivals due to reflections and scattering marked in the red box.

constants.

The main source of error is strong scattering due to the PFC particles (you can see this from the coda arriving after the first arrival). Strong scattering implies strong dispersion and hence generally an advance in the travel times (van der Baan, 2001). The region marked by the box in red are reflected waves bouncing off of the boundary walls of the sample and internal scattering from the PFC particles. Unfortunately, the size of the sample is relatively small (to ease computational expense) so that reflections interfere with the receiver points even at distances in close proximity to the source point. This makes accurate picking more complicated. In the laboratory it is also a well known fact that the dynamic P and S wave velocities do not generally agree with the velocities derived from the static elasticity constants (Jaeger et al., 2007). In a relatively well cemented Berea sandstone, the dynamic velocities may be up to 20-30% faster. In the laboratory, the differences between these two velocities are thought to be a symptom of the micro-structural heterogeneity of rock (as for a homogenous steel the two velocities are in agreement). In these bonded particle models the micro-structure is characterized by particle contacts creating abundant local heterogeneities.

Nevertheless, certainly both the P and S waves are quantifiable in the models and it is now of interest to take a brief look at radiation patterns. Ideally, the radiation patterns from the synthetic seismograms agree with theoretical seismograms created using the moment tensor, and conversely a moment tensor inversion on the synthetic seismograms from the models should produce moment tensors in agreement with the source mechanisms estimated by the algorithm implemented by Hazzard and Young (2004). As a first step in this direction, the radiation pattern for a single particle dislocation is qualitatively

investigated. For a single particle dislocation the theoretical radiation pattern for the far-field P waves is in Figure 7.6a (Aki and Richards, 2002). The maximum amplitude is parallel to the direction of motion and perpendicular to the direction of particle motion the amplitude is null. A simulation is created where eight receiver particles are distributed counter clockwise around the axis of the cylindrical sample, *HRS1*. A source particle is chosen in the center and is manipulated towards the top of the page as in Figure 7.6a. The source particle motion is again sinusoidal. The positions of the receiver particles, looking down the axis of the cylinder, are illustrated in Figure 7.6b.

The simulation is cycled forward 30,000 time steps and the x , and y components of the geophones are projected onto the radial direction (the positive direction is outwards radially from the center). The seismograms are then plotted as a function of azimuth within the radial plane for recs 1-8 in Figure 7.6b; see Figure 7.7. The amplitude and polarity of the first arrivals (P-waves) are in direct agreement with the expected theoretical behavior with maximum amplitudes of opposite polarities along the single force excitation, receivers 1 and 5, and very low amplitude at receivers 3 and 7. The larger signal at 3 compared to 7 is a result of the discrete nature of the models. The receiver point 3 is not exactly at the nine o'clock position whereas receiver particle 7 is very close to the 3 o'clock position as depicted in Figure 7.6b. Notice again reflections and other coda waves immediately following the arrival of the P-waves. This qualitative simulation provides further evidence for the feasibility of studying wave propagation phenomena using these bonded particle models.

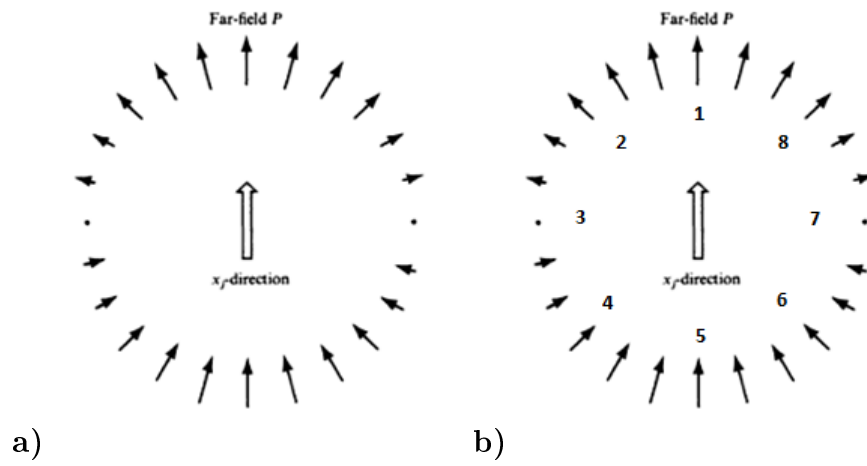


Figure 7.6: a) Theoretical radiation pattern of the P-waves for a single particle dislocation. b) Receiver positions for the simulations superimposed onto the theoretical radiation pattern.

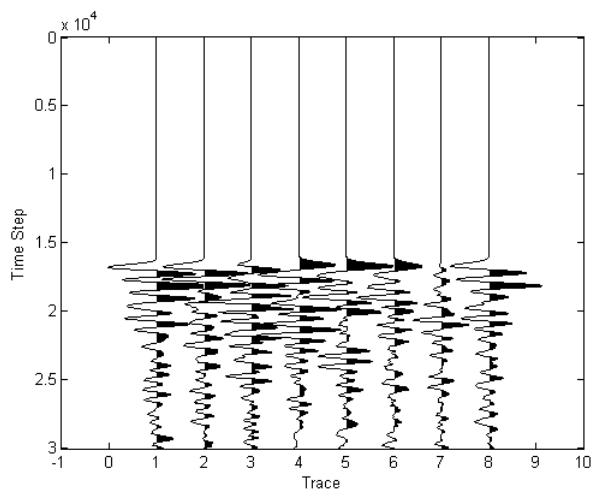


Figure 7.7: Seismograms of the receivers (radial component only) described by the points shown in Figure 7.6b.

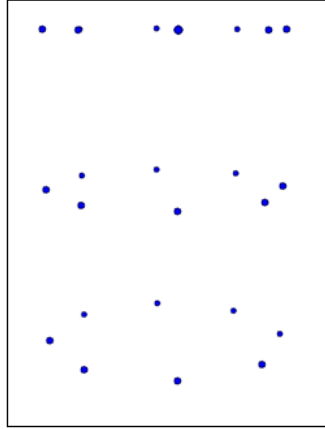


Figure 7.8: A three dimensional array of receiver particles placed within the samples H1 and H2 from Chapter 6.

7.2 Seismograms of a Large Triaxial Simulaion

With a good level of confidence in the wave propagation in the bonded particle models a final simulation was run on the samples H1 and J1 from Chapter 6 where an array of monitoring particles was inserted within the sample; the array is shown in Figure 7.8. The object of this final simulation was to investigate the moment tensors and their radiation patterns while also taking a look at the frequency spectrum of the simulations. The data was quite noisy; any large magnitude events ideal for analysis of the radiation patterns on the receivers occurred during regimes of abrupt failure. With so many events it was hard to isolate seismic signal with its corresponding microseismic event. A simulation needs to be run that decelerates the compression of the platens when there is abrupt failure of the sample so as to allow for relative silence following microseismic events. This would significantly aid with interpretation and analysis of the seismograms. Unfortunately, a spectral analysis was not conducted on the time series for the receiver particles as a Fourier transform needs to be implemented that is able to handle non-stationary time-steps.

7.3 Future Work

From the proceeding discussion, it seems very reasonable to suggest that seismic waves are accurately transmitted through the BPMs allowing for the examination of wave phenomena related to more complex scenarios. The paramount objective of studying geomechanical models in this thesis is to provide insight into the mechanics of a reservoir during hydraulic fracturing; in particular to provide a link between microseismicity observed at the geophones to the actual geomechanical processes occurring in the subsurface.

Future work for the BPMs includes applying moment tensor inversions on the synthetic seismograms to ensure that the results are in agreement with the moment tensors predicted by Hazzard and Young (2004). This may give more confidence in linking geomechanical behavior to the observed microseismicity and vice versa since it may provide indications on how to infer better geomechanical behavior from seismically measured particle motions.

For instance, microseismic monitoring during hydraulic fracturing treatments reveals mysterious resonance frequencies (Tary and van der Baan, 2012). Their cause is thought to be related to the dynamics of resonating hydraulic fractures or non-laminar fluid flow within the medium. Both phenomena have been studied in the context of volcano seismology (Ferrazzini and Aki, 1987; Benson et al., 2008). Although the bonded particle models are quite primitive in that they do not incorporate fluid processes, the fact that the models are able to reproduce rock mechanical behavior, failure, and synthetic seismograms suggests that more research should be geared towards introducing fluid processes into the models. Perhaps, low frequency phenomena may be observed in the synthetic seismograms which could than be directly linked to the particle motions and the geomechanics.

In the context of plate tectonics and global seismology the bonded particles models may potentially provide insight into the geomechanics occurring during slow earthquakes. Seismic tremor or low frequency signal often occurs simultaneous with slow slip events, for example in Cascadia (Rogers and Dragert, 2003). The resonance phenomena may be a result of the slippage along a fault. Again the underlying processes are assumed to be related to fluids. One proposed explanation is that subducting slab release aqueous fluids by dehydration; the fluid then migrates to the slab surface. At high temperatures and pressure the fluid mixes with silicates and exists as supercritical fluid. This supercritical fluid reduces friction causing slow slip events and forms new cracks by the process of hydraulic fracturing. It is the superposition of these microseismic hydraulic fracturing events that are responsible for the tremor (Obara, 2002). Although the low frequency signal is likely a result of fluid processes (perhaps analogous to the low frequency signal observed during hydraulic fracture treatments) the geomechanical models may provide some insight on the link between the microseismicity and deformation that occurs during slippage along a fault.

Ferdowsi et al. (2013) uses discrete element models to investigate microslips as precursor to large slip events along faults. In Chapter 6 a cataclastic type flow was modeled where spherical particles both roll and slide providing a suitable medium for stable sliding along a fault. Bonded-particle methods provide the opportunity to simulate this effect and examine its seismic signature on geophones. Although it is unlikely that any resonance phenomena will be observed, the simulations could be useful for further reinforcing the argument that low frequency signal is tied to specific deformation processes either through direct examination of any transient microseismic events, in their location patterns and moment tensors, associated with stick-slip on asperities

and brittle failure in general, or via examination of any low-frequency signals associated with frictional sliding, and other aseismic phenomena.

Chapter 8

Conclusions and Future Work

Hydraulic fracturing is a modern approach to accessing unconventional hydrocarbon reservoirs. Microseismicity is now an essential tool for monitoring the growth of fracture networks and with today's growing need for energy there is now a real push to obtain a deeper understanding of the reservoir geomechanics and its associated microseismicity. There are a number of key questions that were discussed throughout this thesis.

It has been observed that the energy input of hydraulic fracturing is millions of times larger than the observed energy output from the microseismicity (Maxwell et al., 2008). The deformation is much more complicated than simply brittle failure as certainly ductile type processes are occurring within the subsurface during hydraulic fracture treatments. In Chapter 5, triaxial tests were conducted on cylindrical sleeves that were the aggregation of thousands of bonded spherical particles that reproduced the macroscopic behavior of sandstones. Throughout the simulations, the energy budget was monitored, specifically monitoring the radiated energy of the system following bond breakages (by tracking kinetic energy). Failure mechanisms for the microseismic

events were estimated using a moment tensor algorithm created by Hazzard and Young (2004). The moment tensors were used to calculate the radiated energy for the failure using the formula from Kanamori (1977). The percentage of the radiated energy to the input energy from the moment tensors was in agreement with estimates by Boroumand and Eaton (2012). The percentage of the radiated energy to the input energy by tracking kinetic energies was about 2.5%, which was higher by a factor of about 10 than estimates of the radiated energy from the moment tensors. It was then suggested that energy releases incurred from brittle failure are larger than previously suspected. In fact, an updated formula for the relationship between radiated energy and the magnitude of the event was proposed: $\log_{10}E_K = 1.86Mw_W + 8.36$. Statistical analysis of the microseismicity of the simulations was explored which exhibited behavior observed in laboratory experiments. The b -values were similar to that of several authors (Lei, 2003; Lei et al., 2004). With the radiated energy being only about 2.5% of the boundary work ductile and aseismic deformation must make up a large portion of the energy budget. In fact, with around 30% of the boundary work lost to friction the primary energy sink must be the potential energy of the contacts and parallel bonds.

There are a number of topics from Chapter 5 that could use further study. The main area for further research is to more closely analyze the energy budget. Within the BPM there is boundary work, potential energy of the contacts and bonds, kinetic energy, energy losses to friction, energy lost to damping, and finally energy losses due to the numerical approximations within the models (which can be assumed to be small Itasca Consulting Group (1999)). Simulations need to be run where all avenues of the energy are monitored. The power of these models is that at any moment the total mechanical energy of the system can be dissected. Although it was concluded that the primary

energy sink is the energy of the contacts and parallel bonds, this should be confirmed by running additional simulations. The conservation of mechanical energy should be confirmed throughout the simulations to ensure that there is no (or minimal) energy lost (or gained) due to numerical integration.

With only 2.5% of the input energy released as seismic waves in the models it was of interest to investigate aseismic deformation within the samples. Energy losses due to sliding along a joint was examined in Chapter 6. In the context of plate tectonics and global seismology, large scale slippage along faults is observed, called slow slip events, where no seismic waves are detected (although a mysterious low frequency phenomenon often accompanies them) (Schwartz et al., 2007). It has been proposed that such aseismic processes may be a possible candidate for the discrepancy of the energy budget observed during hydraulic fracture treatments. Perhaps stable sliding along preexisting fractures and joints absorb a portion of the input energy. Joints were created and calibrated by applying direct shear tests on the bonded particle models. The deformation along the joints exhibited granular flow type processes, stable frictional sliding, and abrupt slips. Highly confined samples showed more abrupt slips, where simulations run at low confinements were characterized by more granular type flow. These models support the fact that a granular flow should occur at low confinement pressures (shallow depths or high pore pressure). There is an inverse relationship between the size of the shear zone of a fault and its coefficient of static friction. The energy budget of a triaxial simulation with a joint contained within the sample was explored. It was found that deformation along the joint accounted for negligible energy losses due to stable frictional sliding. This is likely the fact that rolling spheres lose no energy to frictional work. If any aseismic deformation or slow slip events at subduction zones and during hydraulic fracture treatments is marked by rolling spheres and granular

type flows it is unlikely that any significant portion of the input energy is lost to friction. The primary energy sink must be the strain energy of the rock.

Certainly more research should be conducted with respect to joints within the confines of these samples. A number of studies have been conducted already, for example Mas Ivars et al. (2011), where they introduce a smoothjoint logic which eliminates the inherent rugosity of the BPM samples. The smooth joint logic tries to overcome the limitations of these rough surfaces (Ivars et al, 2008), but unfortunately, they currently seem to be more applicable to smaller scale sliding only. They also investigate unbonded regions of various grain sizes. Simulations should be set up to monitor the energy budget for these other surface interfaces as perhaps the results may differ from what was discovered here.

In Chapter 7 the elastodynamics of the models was investigated. Toomey and Bean (2000) showed that it was possible to accurately model wave propagation in a two dimensional DEM model. In this thesis, wave propagation was investigated for the three dimensional bonded particle models. When individual particle velocities were monitored within the models, during the brittle regime of the triaxial simulations, the particle velocities closely resembled seismograms. The failure of the samples and bond breakages were a precursor to the motion observed on the seismograms. P and S wave velocities were measured in a controlled environment and they were in close agreement with the theoretical values derived from the elasticity constants. In the simple case of a single particle dislocation the radiation patterns were in agreement with theory. A triaxial test was conducted on a high resolution sample with a receiver array contained within. The seismograms were marked by many microseismic events as the failure of the sample accelerated during the brittle regime of the

triaxial simulation. It was difficult to isolate microseismic events and their corresponding seismic signatures on the array. A simulation needs to be run where the axial load decelerates during abrupt failure so as not to contaminate the array with too many events.

With the BPM able to model synthetic seismograms there is a myriad of research that should be done. As already mentioned in Chapter 7, the estimated moment tensors using the algorithm by Hazzard and Young (2004), needs to be confirmed with the particle motions in the models. Forward modeling could be done to verify radiation patterns and relative amplitudes but, ideally, a moment tensor inversion should be run on the synthetic seismograms to establish confidence in both the elastodynamics of the models and the estimated moment tensors. With confidence in the elastodynamics, the frequency spectrum during simulations should be examined to perhaps provide some insight into the low frequency resonance phenomena observed during both slow slip events and hydraulic fracture treatments. A number of other tests should be run in order to further provide confidence in the wave propagation (for example reflection coefficients between layers of separate acoustic impedance, etc).

Regarding the simulations conducted throughout the thesis, the tests should be run with the flat joint contact logic introduced since the tensile strength of the bonded particle models are larger than those of real rocks found in laboratory experiments. The flat joint logic removes the unrealistically high tensile strengths (Potyondy, 2011). It is extremely likely that the high tensile strength of the models will have an effect on the failure of the samples. Hudson plots in Chapter 5 indicated tensile failure (opening and closing type events) and so the failure should be re-examined with the more realistic geomechanical model.

Finally, the bonded particle model was able to produce both interesting and quantifiable results. The models were able to reproduce all sorts of deformation including elastic, ductile, and brittle deformation. Additionally the models were able to investigate sliding and granular type flows along with wave propagation. As the BPM is able to reproduce stress/strain, failure and elastodynamics of samples, the bonded particle model should be considered a powerful geomechanical model and that it is a viable approach for modeling more complicated scenarios. With initial confidence in these models established, attempts should be made to couple the three dimensional bonded particle models with fluid processes in hope of directly modeling hydraulic fracture treatments.

References

Aki, K. and P. G. Richards, 2002, Quantitative seismology: University Science Books, 2nd edition

Amitrano, D., 2003, Brittle-ductile transition and associated seismicity: Experimental and numerical studies and relationship with the b-value: Journal of Geophysical Research, 108, 2044

Bahrani, N. and B. Valley, 2011, Evaluation of PFC2D Grain-Based Model for Simulation of Confinement-Dependent Rock Strength Degradation and Failure Processes: ARMA 11-156

Baig, A. M. and T.I. Urbancic, 2010, Microseismic moment tensors: A path to understanding frac growth: The Leading Edge, 29, 320-324.

- Benson, P. M., S. Vinciguerra, P. G. Meredith, and R. P. Young, 2008, Laboratory Simulation of Volcano Seismicity: *Science*, Vol. 322, no. 5899 pp. 249-252
- Beroza, G. C. and S. Ide, 2011, Slow Earthquakes and Nonvolcanic Tremor: *Ann. Rev. Earth and Planet. Sci.* Vol. 39 271-296
- Boroumand, N., and D. W. Eaton, 2012, Comparing Energy Calculations - Hydraulic Fracturing and Microseismic Monitoring: 74th Mtg., EAGE, Copenhagen, C042.
- Chorney, D., Jain, P., Grob, M., van der Baan, M., 2012. Geomechanical modeling of rock fracturing and associated microseismicity. *Lead. Edge* 31, 1348–1354.
- Cundall, P. A., 1971, A computer model for simulating progressive large scale movements in blocky rock systems, *ISRM Symp.*, Nancy, France, Proc. 2, pp. 129-136
- Danian, Y. and Z. Jinmin, 1991, Haphazard Packing of Unequal Spheres: *Chinese Journal of Geochemistry*, Vol. 10 No. 2
- Davis, G. H., S. J. Reynolds, and C. Kluth, 1942, *Structural geology of rocks and regions*: 3rd ed.
- Denton, W.H., 1957, The packing and flow of spheres: *AERE Report E/R* 1095
- Dieterich, J. H., 1978, Time-Dependent Friction and the Mechanics of Stick-Slip: *Pure Appl. Geophys.*, 116, 790-806.
- Dieterich, J. H., 1979, Modeling of Rock Friction 1. Experimental Results and Constitutive Equations: *Journal of Geophysical Research*. Vol 84.

Dragert, H., K. Wang, and T. S. James, 2001, A silent slip event on the deeper Cascadia subduction interface: *Science*, 292, 1525 - 1528.

Ferdowsi, B., M. Griffin, R. A. Guyer, P. A. Johnson, C. Marone, and J. Carmeliet, 2013, Microslips as precursors of large slip events in the stick-slip dynamics of sheared granular layers: A discrete element model analysis: *Geophysical research letters*, VOL. 40, 4194 - 4198

Ferrazzini, V. and K. Aki, 2012, Slow waves trapped in a fluid-filled infinite crack: Implication for volcanic tremor: *JGR Solid Earth*, Vol 91, pp 9215-9223

Fjaer, E., R. M. Holt, A. M. Raaen, R. Risnes, and P. Horsrud, 2008, *Petroleum Related Rock Mechanics*: Elsevier, Amsterdam

Graham, C.C, S. Stanchits, I. G. Main, and G. Dresen, 2009, Comparison of polarity and moment tensor inversion methods for source analysis of acoustic emission data: *Int. J. Rock Mech. Min. Sci.* 47 161-169

Grassberger, P., and I. Procaccia, 1984, Dimensions and entropies of strange attractors from a fluctuating dynamics approach: *Physica D: Nonlinear Phenomena*, 13, 34 – 54.

Grob M. and M. Van der Baan, 2011, Inferring in situ stress changes by statistical analysis of microseismic event characteristics. *The Leading Edge*, 30 (11), 1296-1301

Gutenberg, B., and C. F. Richter, 1944, Frequency of earthquakes in california: *Bulletin of the Seismological Society of America*, 34, 185–188

Hazzard, J.F., and R. Young, 2004, Numerical investigation of induced cracking and seismic velocity changes in brittle rock: *Geophysical Research Letters*, 31, no. L01604

Hazzard, J. F., R.P. Young, and S.C. Maxwell, 2000, Micromechanical modeling of cracking and failure in brittle rocks: *Journal of Geophysical Research*, 105, no. B7, 16683-16697

Hirose, H., K. Hirahara, F. Kimata, N. Fujii, and S. Miyazaki, 1999, A slow thrust slip event following the two 1996 Hyuganada earthquakes beneath the Bungo Channel, southwest Japan: *Geophysical research letters*, Vol. 26, No 21, pages 3237-3240.

Hudson, J.A., R.G. Pearce and R.M. Rogers, 1989, Source type plot for inversion of the moment tensor: *Journal of Geophysical Research*, 94, no. B1, 765-774

Itasca Consulting Group Inc. PFC2D/3D (Particle Flow Code in 2/3 Dimensions), Version 2.0. Minneapolis, MN: ICG; 1999.

Jaeger, J.C., N.G.W. Cook, and R.W. Zimmerman, 2007, *Fundamentals of Rock Mechanics*: Fourth edition, blackwell.

Jouniaux, L., K. Masuda, X. Lei, O. Nishizawa, K. Kusunose, L. Liu and W. Ma, 2001, Comparison of the microfracture localization in granite between fracturation and slip of a preexisting macroscopic healed joint by acoustic emissions measurements: *Journal of Geophysical Research*, 106, no. B5, 8687-8698

Kanamori, H., 1977, The energy release in great earthquakes: *Journal of Geophysical Research*, 82, no. 20, 2981-2987

Kanamori, H., 2001. Energy budget of earthquakes and seismic efficiency, in: Majewski, E., Teisseyre, R. (Eds.), *Earthquake Thermodynamics and Phase Transformations in the Earth's Interior*. Academic Press, San Diego, California, pp. 293-305.

Kanamori, H., Rivera, L., 2006. Energy partitioning during an earthquake, in: Abercrombie, R. (Ed.), *Earthquakes: Radiated Energy and the Physics of Faulting*. AGU, Washington, DC, pp. 3–13.

Lei, X., 2003. How do asperities fracture? An experimental study of unbroken asperities. *Earth Planet. Sci. Lett.* 213, 347–359.

Lei, X., Masuda, K., Nishizawa, O., Jouniaux, L., Liu, L., Ma, W., Satoh, T., Kusunose, K., 2004. Detailed analysis of acoustic emission activity during catastrophic fracture of faults in rock. *J. Struct. Geol.* 26, 247–258.

Ling, L., 2003, A review of techniques, advances, and outstanding issues in numerical modelling for rock mechanics and rock engineering: *Int. J. Rock Mech. Min. Sci.* 40, 283-353

Lockner, D., Byerlee, J., Kuksenko, V., Ponomarev, A., Sidorin, A., 1991. Quasi-static fault growth and shear fracture energy in granite. *Nature* 350, 39–42.

Lockner, D.A., Byerlee, J.D., Kuksenko, V., Ponomarev, A., Sidorin, A., 1992. Observations of Quasistatic Fault Growth from Acoustic Emissions, in: Evans, B., Wong, T. (Eds.), *Fault Mechanics and Transport Properties of Rocks*. ACADEMIC PRESS LIMITED, London, pp. 3–31.

Mas Ivars, D., M. Pierce, D. DeGagne, and C. Darcel, 2008, Anisotropy and scale dependency in jointed rock mass strength - A synthetic rock mass study: In R. Hart, C. Detournay and P. Cundall (eds), *Proceedings of the 1st International FLAC DEM Symposium on Numerical Modeling*, August 25-27, 2008, Minneapolis, MN USA. Minneapolis: Itasca (In press).

Mas Ivars, D., Pierce, M.E., Darcel, C., Reyes-Montes, J., Potyondy, D.O.,

Paul Young, R., Cundall, P. a., 2011. The synthetic rock mass approach for jointed rock mass modelling: *Int. J. Rock Mech. Min. Sci.* 48, 219–244.

Maxwell, S.C. and T. I. Urbancic, 2001, The role of passive microseismic monitoring in the instrumented oil field: *The Leading Edge*, June, pp. 636 - 639

Maxwell, S.C., J. Shemata, E. Campbell, and D. Quirk, 2008, Microseismic deformation rate monitoring. SPE 116596.

McGarr, A., 1999. On relating apparent stress to the stress causing earthquake fault slip. *J. Geophys. Res.* 104, 3003–3011.

Murphy, W.F., III, 1982, Effects of Microstructure and Pore Fluids on the Acoustic Properties of Granular Sedimentary Materials: Ph.D. dissertation, Stanford University

Obara, K., 2002, Nonvolcanic deep tremor associated with subduction in southwest japan: *Science*, Vol. 296, no. 5573, pp. 1679-1681

Potyondy, D.O., and P. A. Cundall, 2004, A bonded-particle model for rock: *International Journal of Rock Mechanics and Mining Sciences*, 41, no. 8, 1329-1364

Potyondy, D.O., 2006, Simulating stress corrosion with a bonded-particle model for rock: *Int. J. Rock Mech. Min. Sci.* 44 677-691

Potyondy, D.O., 2007, The Effects of Voids on the Mechanical Properties of Rock: *Proceedings of the Fourth International Conference on Discrete Element Methods*, Brisbane, Australia.

Potyondy, D.O., 2011, Parallel-bond refinements to match macroproperties of hard rock: *Cont. Dist. El. Mod. Geo.*, paper: 08-04

- Potyondy, D.O., 2012, A Flat-Jointed Bonded-Particle Material for Hard Rock: American Rock Mechanics Association, 12-501
- Rae, D., 1963, The measurement of the coefficient of friction of some rocks during continuous rubbing: *J. Sci. Instr.*, 40, 438-40
- Rogers, G., and H. Dragert, 2003, Episodic Tremor and Slip on the Cascadia Subduction Zone: The Chatter of Silent Slip: *Science*, Vol. 300, no. 5627, pp 1942-1943
- Scholz, C., 2002. *The Mechanics of Earthquakes and Faulting*, Second edi. ed. Cambridge University Press.
- Schorlemmer, D., Wiemer, S., Wyss, M., 2005. Variations in earthquake-size distribution across different stress regimes. *Nature* 437, 539–42.
- Schwartz, S. Y. and J. M. Rokosky, 2007, Slow slip events and seismic tremor at circum-Pacific subduction zones: *Rev. Geophys.* 45:RG3004.
- Senseny, P. E., 1983, Laboratory Measurements of Mechanical Properties of Sandstones and Shales: SPE/DOE 11762
- Silver, P. and T. Jordan, 1982, Optimal estimation of scalar moment: *Geophysical Journal of the Royal Astronomical Society* 70, 755 - 787.
- Sleep, N. H. and M. Blanpied, 1992, Creep, compaction and the weak rheology of major faults: *Nature* 359, pp. 687-692
- Spherical Packing, Wikipedia: The Free Encyclopedia. Wikimedia Foundation, Inc., 2013. <http://en.wikipedia.org/wiki/Sphere_packing>
- Stein and Wysession, 2003, *An Introduction to Seismology, Earthquakes, and Earth Structure*: Blackwell Publishing

Stesky, R.M., W.F. Brace, D. K. Riley, and P.F. Robin, 1974, Friction in faulted rock at high temperature and pressure: *Tectonophysics*, 23.

Tary, J. B. and M. van der Baan, 2012, Potential use of resonance frequencies in microseismic interpretation: *The Leading Edge*, 31(11), 1338-1346

Thompson, B.D., 2005. Observations of premonitory acoustic emission and slip nucleation during a stick slip experiment in smooth faulted Westerly granite. *Geophys. Res. Lett.* 32, L10304.

Toomey, A. and C. J. Bean, 2000, Numerical simulation of seismic waves using a discrete particle scheme: *Geophys. J. Int.* 141, 595-604

van der Baan, M., 2001, Acoustic wave propagation in one dimensional random media: the wave localization approach: *Geophys. J. Int.* 145, 631-646

Warpinski, N., S. Wolhart, and C. Wright, 2001, Analysis and Prediction of Microseismicity Induced by Hydraulic Fractures: paper SPE 71649.

Weaire, D., 1999, A Short History of Packing Problems: *Review Forma*, 14, 279-285

Yoon, J., A. Zang, and O. Stephansson, 2012, Simulating fracture and friction of Aue granite under confined asymmetric compressive test using clumped particle model: *Int. J. Rock Mech. Min. Sci.*, 49, 68-83

Yoon, J., A. Zang, and O. Stephansson, 2013, Hydro-mechanical coupled discrete element modeling of geothermal reservoir stimulation and induced seismicity: *Clean Energy Systems in the Subsurface*, SSGG, pp. 221-231.

Zhao, X., and R. P. Young, 2011, Numerical modeling of seismicity induced by fluid injection in naturally fractured reservoirs: *Geophysics*, Vol. 76, No. 6, pp 167-180

Zoback, M. D., A. Kogi, I. Das, and M. McClure, 2012, The importance of slow slip on faults during hydraulic fracturing stimulation of shale gas reservoirs: SPE 155476

Yoshioka, S., T. Mikumo, V. Kostoglodov, K Larson, A. Lowry, and S. Singh, 2004, Interplate coupling and a recent aseismic slow slip event in the Guerrero seismic gap of the Mexican subduction zone, as deduced from GPS data inversion using a Bayesian information criterion